Lab on a Chip

Devices and applications at the micro- and nanoscale

Accepted Manuscript

Volume 17
Number 1
7 January 2017
Pages 1-200

Lab on a Chip

Devices and applications at the micro- and nanoscale

rsc.li/loc

ISSN 1473-0197

PAPER
Chengzhi Hu, Bradley J. Nelson et al.
Characterization of size-dependent mechanical properties of top-growing cells using a lab-on-a-chip device

ROYAL SOCIETY OF CHEMISTRY

rsc.li/loc

Interfacial electro-hydrodynamics inspired micro/nano-fluidic energy conversion: from mechanism to applications

Lingxuan Hao[1†], Mohammed Imran Khan[1†], Yilin Lei[1†], Shuneng Zhou[1], Bei Fan[1*]

[1]Mechanical Engineering Department, Michigan State University,
48823-East Lansing, Michigan, USA
†These authors contribute equally to the paper
*Corresponding author: fanbei1@msu.edu

Abstract

Water, with its natural abundance and various forms, has been a promising sustainable energy source. To harness water energy more efficiently, interfacial electro-hydrodynamics (EHD) micro/nano-fluidic energy conversion and harvesting technologies have rapidly advanced over the past few decades. Compared to conventional water energy harvesting methods like hydroelectric dams and tidal power plants, EHD-based approaches exhibit unique advantages in capturing random, low-frequency, and intermittent fluid motions, enabling the effective harvesting of untapped energy sources such as raindrops, tides, and even ambient humidity. This review systematically summarizes the major interfacial EHD inspired micro/nano-fluidic energy harvesting and conversion strategies, providing an in-depth analysis of their working principles, design principles for enhancing electric output, and their potential applications that mainly include power sources and self-powered devices. Furthermore, we highlight the key challenges facing this field and discuss future research directions and breakthroughs required to facilitate the feasibility and scalability of EHD-based energy harvesting and conversion systems. With continued advancements, these technologies offer significant promise for transitioning from laboratory research to practical applications, providing sustainable and distributed energy solutions.

1. Introduction

As global energy demands continue to rise, the reliance on fossil fuel-based electricity generation poses significant environmental and sustainability challenges. Fossil fuel combustion not only depletes finite resources but also emits greenhouse gases, which contribute to global warming, climate change, and ecological degradation.[1–3] In response, there has been an urgent shift toward renewable energy

solutions to reduce carbon footprints and ensure a sustainable energy future. Among various energy harvesting methods, liquid-based energy harvesting, particularly from water, stands out due to the abundance and renewability of water, as well as the diverse ways energy can be extracted from it.[4] However, despite covering over 70% of the Earth's surface,[5] water remains an underutilized energy source, as vast amounts of energy stored in various forms in global water cycle have yet to be effectively harvested.[1]

Water has long been a source of both mechanical and electrical energy. Traditional hydropower technologies, such as hydroelectric dams and tidal power plants, have demonstrated the feasibility of large-scale water energy harvesting by converting the kinetic energy of flowing water into electricity. While effective, these systems often require extensive infrastructure, are costly, and are limited to specific geographical locations.[6] More importantly, a large amount of water energy remains untapped in the forms of raindrops, tides, and even moisture.[2,6–9] These underutilized sources, found in widely distributed and dynamic environments, hold immense potential for energy harvesting. However, their low frequency, sparse distribution, and diverse forms make achieving efficient energy harvesting through conventional methods.[8,10–12]

In addition to large-scale renewable energy solutions, the increasing demand for portable and self-powered electronic devices has driven the development of miniaturized, efficient, and low-cost energy harvesting systems.[13–17] With the rapid proliferation of wearable sensors,[16,18] biomedical devices,[19,20] and Internet-of-Things (IOT) applications,[21–23] traditional power generation methods are no longer sufficient to meet energy needs. Liquid-based energy harvesting, with its adaptability and vast potential, presents an opportunity to create compact, noise-free, and environmentally friendly power solutions.[6]

To harness these untapped renewable liquid energy sources, the past few decades have witnessed the rapid emergence and advancement of interfacial electro-hydrodynamics (EHD) inspired micro/nano-fluidic energy harvesting and conversion technologies.[24,25] EHD, which studies the interactions between fluid motion and electric fields, presents a versatile and innovative approach to extracting energy from various liquid-based sources. Unlike conventional methods that primarily rely on large-scale hydropower infrastructure, EHD-based technologies leverage fluids as the medium for

energy transfer and conversion. This enables them to efficiently harvest energy from a wide range of liquid sources, including not only low-frequency, random, and intermittent mechanical motions but also other liquid-based energy forms. These include but are not limited to thermally induced flows, evaporation-driven motion, ionic gradients, and electrochemical potential differences—all of which contribute to the vast and largely untapped reservoir of liquid energy.

The most promising micro/nano-fluidic energy harvesting technologies based on interfacial EHD include reverse electrowetting-on-dielectric (REWOD) energy harvesters,[26,27] triboelectric nanogenerators (TENGs),[28,29] and electrokinetic energy conversion (EKEC) devices,[30,31] as illustrated in Figure 1. These technologies leverage interfacial charge interactions and fluid dynamics to enable efficient energy conversion, offering high adaptability and broad applicability for various liquid energy harvesting scenarios.
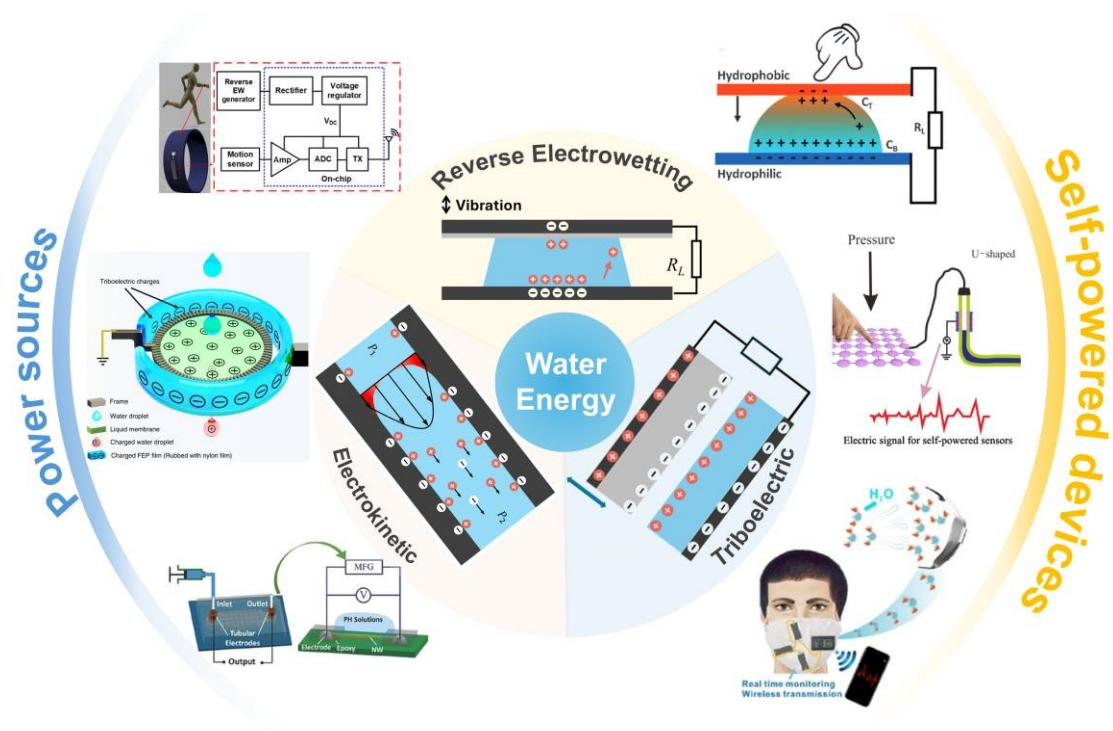
Figure 1. Summary of the working principles and applications of REWOD, TENG, and EKEC. Reproduced with permission.[26] Copyright 2020, IEEE. Reproduced with permission.[27] Copyright 2016, Wiley. Reproduced with permission.[28] Copyright 2017, Elsevier. Reproduced with permission.[29] Copyright 2019, Springer Nature. Reproduced with permission.[31] Copyright 2015, Wiley. Reproduced with permission.[30] Copyright 2023, Elsevier.

REWOD has emerged as a promising technique for fluidic energy harvesting. It leverages the fundamental principles of electrowetting on dielectric (EWOD)[32,33] but operates in reverse: the mechanical deformation of droplets redistributes electrical

charge, thereby generating electrical energy.[34] Recent research has focused on increasing the contact area, increasing the contact area difference (specifically for water-bridge REWOD), optimizing the dielectric film, and increasing droplet oscillation frequency to improve output performance.[34–36]

TENGs generate electricity by combining contact electrification and electrostatic induction, efficiently capturing mechanical energy from human motion, ocean waves, rolling droplets, liquid sloshing, and vibrations. When two materials with different electron affinities come into contact and then separate, electrons transfer between them, creating an electrostatic potential difference. Connecting an external circuit allows electron flow, generating electricity. Recent studies have focused on increasing surface charge, facilitating interface charge transfer, and enhancing liquid motion.[37–39]

EKEC represents a promising mechanism for harvesting energy from fluid motion. This technique takes advantage of the electrokinetic effect, which occurs when an electrolyte interacts with a charged surface to form an electric double layer (EDL) enriched with counterions near the interface. The movement of these counterions along with fluid motion creates an electrical current/potential that can be harnessed for energy. EKEC devices utilize the EDL at solid-liquid or liquid-liquid interfaces to separate charges and generate current under liquid flow. Operating at the nanoscale, EKEC systems can achieve highly efficient energy conversion even in confined spaces. Research in this field has focused on improving electrokinetic efficiency through surface engineering and exploring the interaction of ions at liquid interfaces.[40–43]

In addition, these fluidic energy harvesting technologies have promising applications across various fields. They can efficiently convert fluid motion or phase transitions into electrical energy, making them suitable for power sources, wearable electronics, and autonomous sensing systems. Beyond energy harvesting, they also function as self-powered sensors, enabling real-time detection of physical, chemical, and biological signals. Specifically, REWOD is particularly effective in harvesting low-frequency mechanical energy, especially from intermittent and aperiodic motion, making it highly suitable for energy harvesting from human motion. This capability allows it to power wearable[44–46] and implantable devices,[47,48] as well as mobile electronic systems[34,49] such as GPS devices, smartphones, and medical prosthetics. TENGs are effective in both localized droplet interactions and large-scale liquid flows,

capturing energy from raindrops,[50] ocean waves,[51,52] and pipeline flows,[53,54] making them useful in diverse energy harvesting scenarios. EKEC operates efficiently across various environments, from microfluidic systems[55–58] to large-scale natural water bodies such as oceans and rivers.[59] It can utilize droplets, moisture gradients, evaporation, and continuous flows to generate power, serving as a stable and continuous energy source.[60–62]

In recent years, significant research efforts have been dedicated to developing EHD-based micro/nano-fluidic energy harvesting technologies. As these technologies continue to evolve, it is essential to provide a comprehensive review of the literature, focusing on strategies to enhance electrical energy output, assess practical applications, and address key challenges and prospects. This review summarizes recent advancements in EHD-based micro/nano-fluidic energy harvesting. It begins by outlining the fundamental transduction mechanisms and then presents key developments in structural designs and material innovations that enhance fluid–device interactions, with the aim of improving overall energy conversion efficiency. These emerging technologies show great potential for powering microelectronic devices,[29,35,63] lab-on-a-chip systems,[64–66] next-generation self-powered sensors,[67,68] and smart wearable devices.[14,16,69] Finally, future research directions are discussed, highlighting potential breakthroughs that could enhance the feasibility, scalability, and real-world applicability of EHD-based micro/nano-fluidic energy harvesting systems.

2. Reverse electrowetting on dielectric (REWOD)

2.1. The electric double layer theory at electrolyte-solid interfaces

When an electrolyte solution comes into contact with surface with charges, electrical double layer (EDL) will form at electrolyte-surface interfaces. In 1879, Helmholtz[70] proposed the first EDL model, in which a monolayer of counterions forms a compact ion layer at the solid-liquid interface due to Coulomb forces, referred to as the Helmholtz plane. Gouy and Chapman[71,72] improved this model by considering thermal dynamic of ions, introducing a diffuse double layer where counterions extend outward from the solid surface following a Boltzmann distribution. In 1924, Stern[73] further refined the model by proposing that the electrified solid-liquid interface comprises a compact layer (Stern layer) and a diffuse layer beyond the Helmholtz plane. As illustrated in Figure 2, in the Stern layer, the counterions are strongly bound to the

charged surface. In the diffusion layer, the counterions are more loosely associated and distributed near the surface. In EDL, the electrical potential exponentially decreases as the distance from the surface increases.[74–78] The EDL behaves similarly to an electric capacitor in terms of its geometry and structure.[79–81] The characteristic thickness of the EDL, which significantly influences the potential distribution, is defined as the Debye length, as given by:[82]

$$\lambda_D = \sqrt{\frac{\varepsilon_0 \varepsilon_H k_B T}{2 n_0 z^2 e^2}} \qquad (1)$$

where λ_D is Debye length, n_0 is the concentration of species with charges z at temperature T, ε_0 is the vacuum permittivity, ε_H is the dielectric constant of liquid electrolyte, k_B is the Boltzmann constant, and e is the electronic charge. The development of EDL theories has significantly enhanced the understanding of interfacial charge interactions and transportation, providing a crucial foundation for advancements in REWOD, TENG and EKEC.
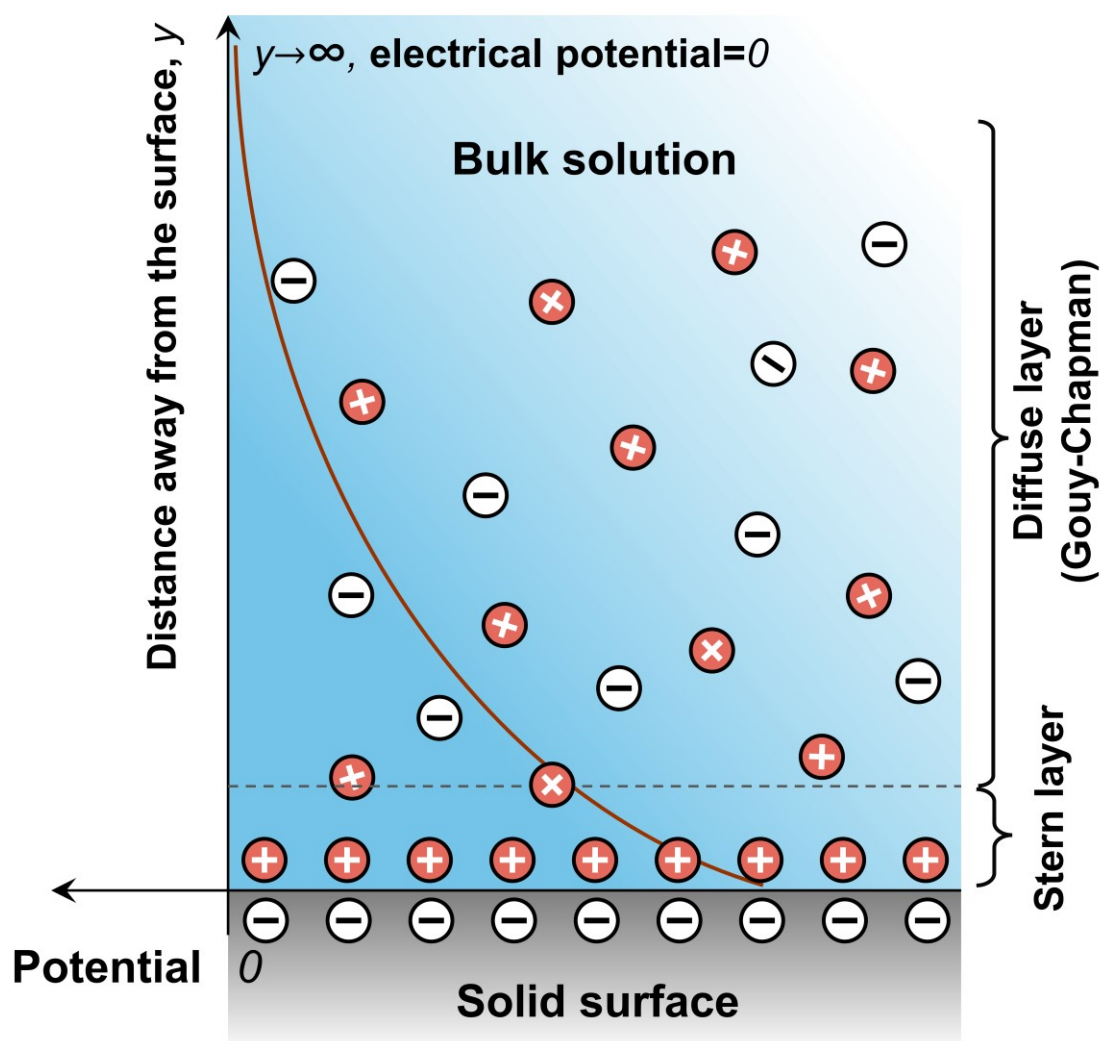
Figure 2. Schematic of EDL structure formed on a negatively charged solid surface. The red line represents the potential distribution along the distance from the surface. A monolayer of ions is adsorbed onto the electrified surface, forming the Stern layer, while the remaining ions are distributed in the diffuse layer.

2.2. Basic working principle

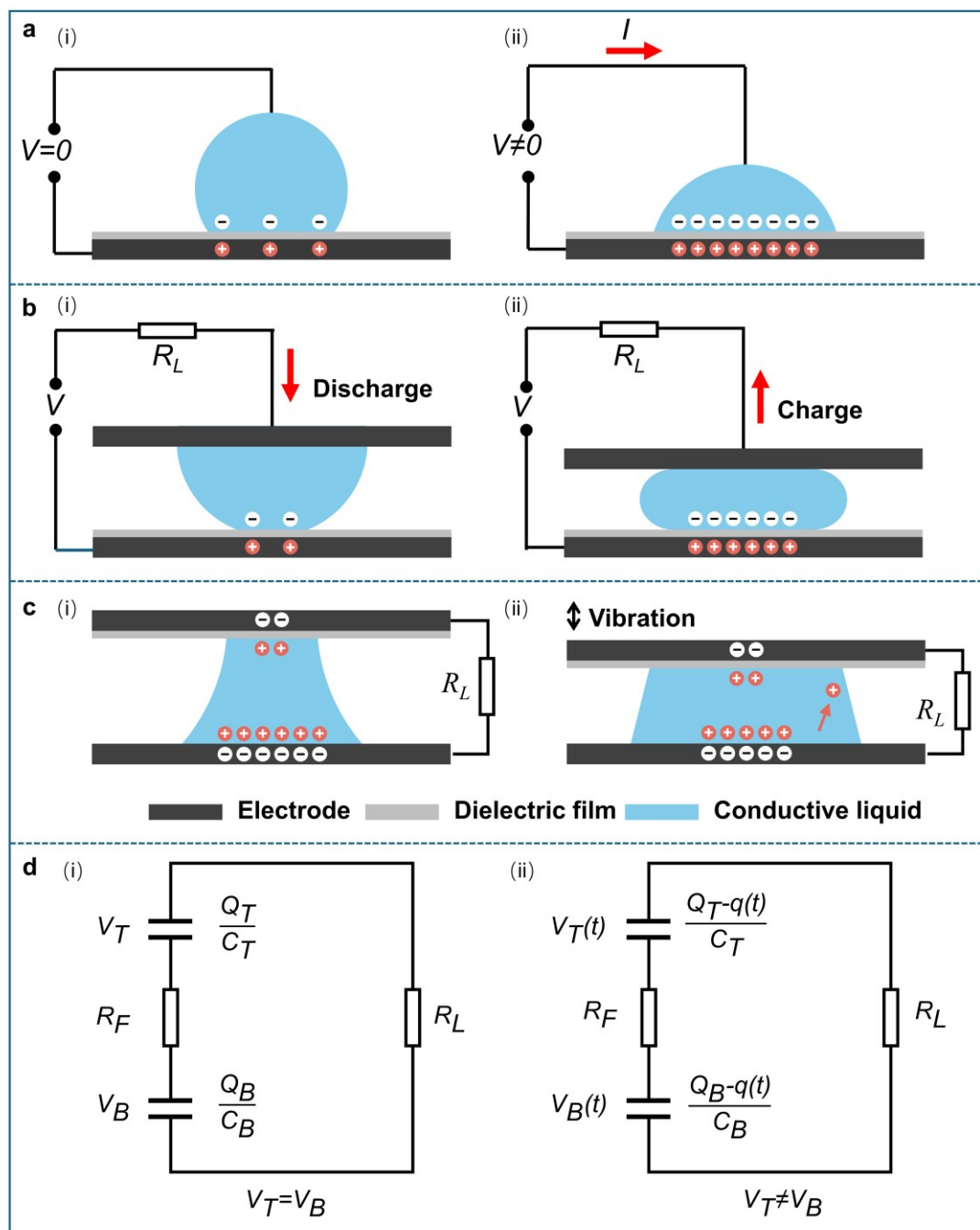Figure **3**. Basic working principles and equivalent circuit diagram. a) Working principle of the EWOD process. (i) no external voltage applied between the metal and the electrolyte solution, (ii) external voltage applied between the metal and the electrolyte solution. b) Working principle of the REWOD process. c) Working principle of the water bridge REWOD process. d) Equivalent circuit diagram of the water bridge REWOD process.

Electrowetting refers to the phenomenon where the surface tension of a liquid on a solid surface changes under an applied electric field. This effect dates back to the late 19th century, when Lippmann[83] first observed the electrocapillarity phenomenon. It was found that the capillary depression of a metal, particularly mercury, in contact with an electrolyte solution could be altered by applying a voltage between the metal and the electrolyte. (*The original work was published in French and later translated into English by Mugele et al., as shown in the appendix of Ref. the leterature.*[84]) The underlying mechanism of this effect involves the spontaneous formation of an EDL at the metal–electrolyte interface when a voltage is applied. Charges accumulate on the metal surface, while a cloud of oppositely charged counterions gathers on the liquid side, reducing interfacial tension. This relationship is quantitatively described by Eqs. 2 and 3, later known as the Lippmann equations.[85]

$$\sigma_e = -\frac{\partial \gamma_{SL}}{\partial V} \tag{2}$$

$$c_H = \frac{\partial \sigma_e}{\partial V} \tag{3}$$

where σ_e is the charge density on the solid-liquid interface, γ_{SL} is the interfacial tension at the solid-liquid interface, V is the applied voltage between the metal and the electrolyte solution, and c_H is the capacitance per unit area of the system. Here, c_H is defined as the capacitance per unit area of the EDL. The explicit dependence of interfacial tension on the applied voltage can be derived by assuming constant capacitance. In that case, the surface charge density becomes $\sigma_e = c_H V$. Substituting this into Eq. 2 and integrating with respect to voltage yields Eq. 4, where V' denotes the integration variable. This equation demonstrates that the interfacial tension decreases quadratically with the applied voltage. The reduction in interfacial energy caused by the electric field is stored as electrostatic energy in the system, forming the theoretical basis for electrowetting behavior.

$$\gamma_{SL}(V) = \gamma_{SL}(0) - \int_0^V \sigma_e(V')dV' = \gamma_{SL}(0) - \frac{1}{2}c_H V^2 \tag{4}$$

However, when the applied voltage exceeds a few hundred millivolts, it can lead to electrolyte decomposition.[84] To address this issue, Berge[86] introduced a thin insulating layer to prevent direct contact between the liquid and metallic electrode. With this approach, the applied voltage can be increased to several hundred volts, making this method more reliable. This technique is known as EWOD. As shown in Figure **3**a, the system can be modeled as two capacitors in series[87,88]: the EDL capacitor at the

insulator–droplet interface (c_H) and the electrical capacitor across the dielectric film (c_d). These capacitances per unit area are given by Eqs. 5 and 6, respectively.

$$c_H = \frac{\varepsilon_0 \varepsilon_H}{\lambda_D} \tag{5}$$

$$c_d = \frac{\varepsilon_0 \varepsilon_d}{d} \tag{6}$$

where ε_0 is the vacuum permittivity, ε_H is the dielectric constant of liquid electrolyte, ε_d is the dielectric constant of the dielectric film, d is the thickness of the dielectric film.

Since the thickness of the dielectric film d generally ranges from hundreds of nanometers to several microns,[48,89–91] the Debye length λ_D typically ranges from sub-nanometer to tens of nanometers, depending on the metal surface and the electrolyte concentration.[92,93] The dielectric constants of common coating layers typically range from a few to over one hundred.[36,48,94] The dielectric constant of liquid electrolytes is typically on the order of tens.[94] As a result, the d/ε_d is usually much larger than λ_D/ε_H. The total capacitance per unit area of the system, c, can be calculated as $c^{-1}=c_d^{-1}+c_H^{-1}$. As a result, c can be approximated as c_d. Consequently, Berge[32,86] derived the EWOD equation (Eq. 8) by combining the Lippmaan equations (Eqs. 2 and 3) with Young's equation (Eq. 7),[33] which later became known as the Young-Lippmann equation.[85,95] Mugele et al.[33] defined the last term of Eq. 8 as the dimensionless electrowetting number, which represents the ratio of the electrostatic energy stored in the electrical capacitor across the dielectric film to the liquid-vapor interfacial energy.[24] The electrostatic energy is given by Eq. 9. As shown in Eqs. 8 and 9, the contact angle of the liquid droplet on the solid surface decreases with increasing voltage V, indicating that the droplet tends to spread on the dielectric surface (Figure **3**a(ii)). This behavior demonstrates that an external electric field enhances the wettability of the dielectric surface by introducing extra electrostatic energy at the interface.

$$cos\theta = \frac{\gamma_{SG}-\gamma_{SL}}{\gamma_{LG}} \tag{7}$$

$$cos\theta(V) = cos\theta(V=0) + \frac{U}{A\gamma_{LG}} \tag{8}$$

$$U = \frac{cAV^2}{2} = \frac{\varepsilon_0 \varepsilon_d A V^2}{2d} \tag{9}$$

where θ is the contact angle of the liquid droplet on the solid surface, U is the electrostatic energy stored in the capacitor across the dielectric film, A is the solid-liquid contact area, and γ_{SG} and γ_{LG} are the interfacial tensions at the solid-gas and liquid-gas interfaces, respectively.

In 2013, Krupenkin and Taylor[34] first proposed that reversing the EWOD process could convert the mechanical energy of liquid motion into electrical energy, a phenomenon known as REWOD. The schematic of REWOD is shown in Figure **3**b.[24] Studies have shown that using ions as charge carriers is generally less efficient for energy generation, primarily due to strong charge trapping at the solid–liquid interface.[96] In contrast, the electrons are less susceptible to interfacial trapping, resulting in a higher density of available free carriers and significantly enhanced charge transport efficiency. As a result, liquid metals are considered ideal fluid in the REWOD systems. In addition, liquid metals exhibit high electrical conductivity, high surface tension, and low vapor pressure. High conductivity enables efficient electron transport and reduces resistive losses; high surface tension contributes to greater energy storage per unit interfacial area; and low vapor pressure enhances the stability of long-term operation. As a result, in this system, a liquid metal droplet is sandwiched between two conductive electrodes, one of which is coated with a dielectric film. Electrons, supplied by an external direct current (DC) bias voltage source, act as charge carriers. When an external force is periodically applied to the electrode, the droplet moves or deforms, causing a periodic change in the solid-liquid interfacial area. This variation alters the capacitance of the capacitor across the dielectric film,[49] thereby converting the periodic mechanical energy into electrical energy.[34] It is noted that the bias voltage itself does not contribute to net energy production during the energy generation process, a higher bias voltage can enhance output power by increasing the number of electrons. However, increasing the bias voltage also raises the risk of dielectric film breakdown. More importantly, this contradicts the fundamental goal of energy harvesting, as it requires additional external energy input.[35,48] In this review paper, such REWOD systems that require a bias voltage are referred to as the classical REWOD method.

To address these drawbacks, Moon et al.[35] proposed a new method for alternating current (AC) electrical power generation using plain water, without the need for an external bias voltage source. Figure **3**c and Figure **3**d illustrate the working principle and the corresponding equivalent electrical circuits, respectively. In this system, a plain water droplet is confined between two electrodes to form a water bridge. The top electrode is coated with a hydrophobic dielectric film (PTFE), while the bottom electrode is hydrophilic (see Section 2.3.2 for details). The contact area between the water and the bottom electrode remains nearly constant during each oscillation period

because of its small contact angle and pinning effects. In contrast, the contact area between the top electrode and water droplet varies significantly during each oscillation cycle. Accordingly, the capacitances at the top and bottom interfaces are described by Eqs. 10 and 11, respectively.

The ions in the plain water act as charge carriers, and the system can be modeled as two capacitors and two resistors connected in series, as shown in Figure **3**d. In Figure **3**d(i), this corresponds to a steady-state condition in which the water bridge is fully formed and the distance between the plates remains constant over time. Here, no current flows and the voltage-capacitance relationships are given by: $V_T=Q_T/C_T$ and $V_B=Q_B/C_B$. However, as the two plates move toward each other, the solid-fluid contact area at the top plate increases, whereas that at the bottom plate remains nearly unchanged. As a result, C_T increases while C_B remains constant. In this non-equilibrium state (as shown in Figure **3**d(ii)), electrical charging occurs at the top plate, while discharging occurs at the bottom plate. Therefore, the voltage expressions are updated as: $V_B(t)=(Q_B-q(t))/C_B$, $V_T(t)=(Q_T+q(t))/C_T(t)$. If the distance between the two electrodes oscillates at frequency f, the two electrodes continuously charge and discharge in different phases, generating an AC equal as $dq(t)/dt$. In this case, the voltage drop ΔV between the two capacitors is given by Eq. 12.

$$C_T(t) \cong \varepsilon_0 A_T(t) \left(\frac{d}{\varepsilon_d} + \frac{\lambda_D}{\varepsilon_H} \right)^{-1} \cong \frac{\varepsilon_0 \varepsilon_H}{d} A_T(t) \tag{10}$$

$$C_B(t) \cong \frac{\varepsilon_0 \varepsilon_H}{\lambda_D} A_B \cong constant \tag{11}$$

$$\Delta V = (R_F + R_L)\frac{dq(t)}{dt} = V_B(t) - V_T(t) = \frac{Q_B-q(t)}{C_B} - \frac{Q_T+q(t)}{C_T(t)}, \ q(t=0) = 0 \tag{12}$$

where C_T is the capacitance at top plate, C_B is the capacitance at the bottom plate, R_F is the electrical resistance across the water bridge, R_L is the load resistance, $q(t)$ is the increment (or decrement) of charges in the top (bottom) EDL at time t, V is the potential on the EDL, Q is the charges stored on the top and bottom electrodes, subscript T and B represent the top and bottom, respectively.

Based on Eq. 12, achieving a higher ΔV requires a greater difference between C_T and C_B. To accomplish this, a dielectric film is attached to the top electrode to increase C_T (as analyzed above). To further increase the difference between C_T and C_B, the disparity between A_T and A_B should also be maximized (to be discussed in Section 2.3.2).[97] This method (hereafter referred to as water-bridge REWOD) eliminates the need for a bias voltage while ensuring that the output power is not too low.

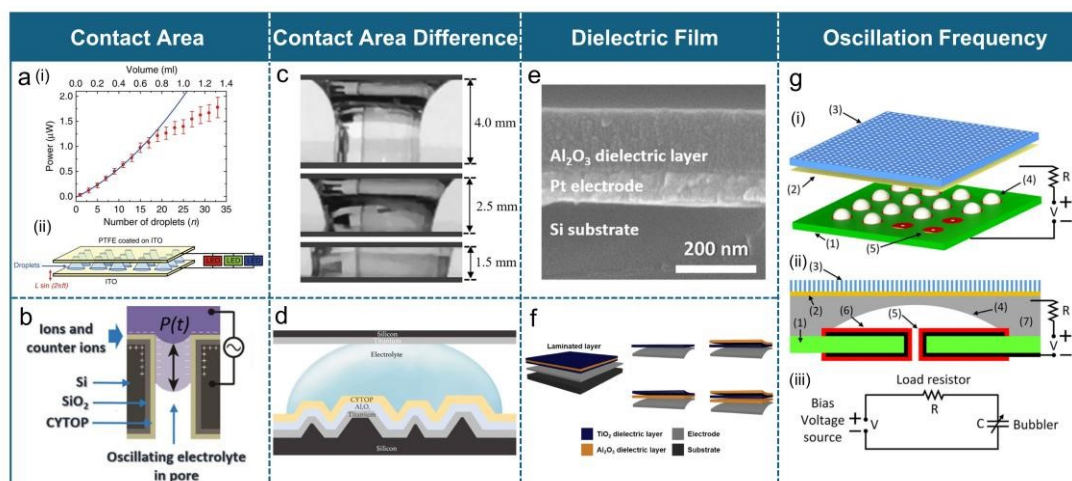## 2.3. Strategies to improve the electric output

Figure 4. Strategies for improving electric output power. a) (i) Power versus the number of water bridges; the solid curve represents a parabolic fit, and data are presented as mean ± standard deviation. (ii) Experimental setup for REWOD with a droplet array. Reproduced with permission.[35] Copyright 2013, Springer Nature. b) Working mechanism of high surface area REWOD energy harvesting under pulsating pressure, leading to AC voltage generation. Reproduced with permission.[98] Copyright 2022, Elsevier. c) Video freeze shots showing three stages of the electrolyte between electrodes during modulation, with electrode distance of 4 mm, 2.5 mm, and 1.5 mm. Reproduced with permission.[99] Copyright 2021, Springer Nature. d) Representative cross-sectional view of a rough electrode model. Reproduced with permission.[48] Copyright 2022, Wiley. e) Field emission scanning electron microscope image of a fabricated atomic layer deposition film sample. Reproduced with permission.[100] Copyright 2017, Elsevier. f) Schematic diagram of laminated structures. Reproduced with permission.[36] Copyright 2021, Springer. g) (i) Conceptual design of the bubbler: (1) REWOD chip, (2) membrane, (3) top plate, (4) an array of bubbles, (5) an array of electrodes; (ii) Schematics of a simplified single-electrode device used in the experiment: (1) REWOD chip, (2) membrane, (3) top plate, (4) bubble, (5) metal electrode, (6) dielectric coating, and (7) conductive liquid; (iii) Equivalent electrical circuit of the single-electrode device. Reproduced with permission.[101] Copyright 2015, Springer Nature.

Maximum achievable power density is one of the most important and desirable characteristics of an energy conversion method, as it allows for the fabrication of smaller and lighter devices that can be coupled to a wide range of energy sources. Krupenkin and Taylor[34] reported that a single conductive droplet, with a solid-liquid contact area of about 1 mm^2, can generate an instantaneous power density of about 10^2 W/m^2.

According to Eq. 9, the output power of REWOD during a single oscillation is directly proportional to the capacitance per unit area, the solid-liquid contact area, and the square of the bias voltage. The capacitance per unit area can be increased by enhancing the dielectric constant of the dielectric film and reducing its thickness.

Specifically, in the water-bridge REWOD system, the output power also increases with the difference between the top and bottom contact areas. Moreover, the total output energy is also strongly influenced by the oscillation frequency of the droplet.

It is important to note that, as previously discussed, although increasing the bias voltage can enhance the output power and the bias voltage itself does not contribute to the net output power, this approach contradicts the fundamental goal of energy harvesting. Moreover, a higher voltage between the electrodes increases the risk of dielectric film breakdown. Therefore, relying on a higher applied voltage is not a practical strategy for improving output power. On the contrary, achieving a lower bias voltage or even a bias-free operation has become a growing trend for enhancing the practical applicability of REWOD systems.

Based on the above, the energy generated by the entire REWOD system can be increased through four main methods: (i) increasing the contact area, (ii) increasing the contact area difference (iii) optimizing the dielectric film, and (iv) increasing the droplet oscillation frequency.

2.3.1. Increasing the contact area

For the classical REWOD method (as shown in Figure **3**b), an effective way to achieve higher output power is to increase the solid-liquid contact area. This can be achieved through the following main approaches: increasing the volume of the liquid droplet, using droplet arrays, and modifying the surface properties of the electrodes, including enhancing surface roughness, using low-hysteresis materials.

2.3.1.1. Increasing the liquid volume

For water-bridge REWOD, Moon et al.[49] demonstrated that increasing the droplet volume can enlarge the contact area and thereby enhance the output power. However, the droplet volume is constrained by the capillary length of water. The capillary length is a characteristic scale that reflects the balance between surface tension and gravitational forces, and is defined as: $l_c = \sqrt{\frac{\gamma}{\rho g}}$, where γ is the liquid-air surface tension, ρ is the liquid density, and g is the gravitational acceleration. At room temperature, the water-air surface tension is 0.072 N/m. The capillary length l_c is therefore approximately 2.7 mm. In the classical approximation, a stable droplet can be modeled as a hemispherical cap with a radius of l_c, whose volume is given by $\frac{2\pi l_c^3}{3}$. *As a result, the corresponding droplet volume can be estimated to be approximately 40 µL.*

13

When the size of the water bridge exceeds this threshold, surface tension can no longer sustain a spherical cap shape, and gravity dominates the droplet morphology, causing it to spread into a pancake-like configuration.[97] In addition, we note that although the capillary length primarily limits the maximum stable droplet volume, the contact angle also contributes as a secondary role in confined geometries. When the top surface is hydrophilic while the bottom surface is hydrophobic, a larger maximum stable volume is potentially obtained. This is because the stronger adhesive force forms between the top surface and water molecules, which can partially counteract the gravitational force acting on the water bridge. The higher free energy barriers of hydrophobic surfaces can prevent the system from transitioning to a lower energy state, thereby allowing droplets to remain in a metastable configuration.[102] This implies that when a droplet is placed on hydrophobic surfaces, it can persist beyond the equilibrium stability limit, supporting a larger volume compared to hydrophilic surfaces. As a result, the combination of stronger adhesion and higher energy barriers could lead to a higher gravitational stability threshold. However, when the hydrophilic surface is located at the bottom and the hydrophobic surface at the top, the situation reverses: the water bridge is more likely to destabilize and flatten into a pancake-like shape. Additionally, water naturally evaporates when exposed to air, causing a gradual decline in output power over time in open systems. In contrast, when the system is properly sealed to be airtight, the output power remains stable over time.[35]

Although the maximum droplet volume is limited by the capillary length, which restricts the increase in output power, this limitation can be addressed by increasing the number of droplets operating in parallel (as shown in Figure 4a), which directly increases the total contact area. In water-bridge REWOD systems, as explained in Section 2.2, the top and bottom capacitors are continuously charged and discharged out of phase, generating an AC power. Therefore, when increasing the number of droplets, it is essential to maintain multiple uniformly sized water bridges in parallel. Experimental Data indicates that the output power increases quadratically with the number of droplets. However, this quadratic relationship begins to break down when the number exceeds 17, likely due to unsynchronized top contact areas of the water bridges caused by inevitable variations in droplet size and shape.[35] Approximately 1 mL of water—arranged as a droplet array (the exact number of droplets was not specified in the original paper)—can generate about 1.5 µW of power, with a maximum

power density of 0.3 μW/cm².[35] This method demonstrates great potential for achieving high output in REWOD systems and has been widely adopted in recent research.[35] As a result, the development of REWOD devices based on droplet arrays has become an important direction for further optimization.

2.3.1.2. Modifications in electrodes

In the EWOD process, contact angle hysteresis leads to contact line pinning, where the droplet's contact line remains stationary under external forces (in this case, the applied electric field). This phenomenon is primarily caused by surface heterogeneities, roughness, or chemical inhomogeneities, which introduce energy barriers that the contact line must overcome to advance or recede. As a result, the droplet does not respond smoothly to the applied voltage and is difficult to spread, thereby reducing the actuation efficiency of EWOD-based systems.[33] Similarly, in the REWOD process, contact line pinning impedes fluid spreading, thus suppressing changes in the contact area and ultimately limiting energy generation. Krupenkin and Taylor pointed out that the effects of contact angle hysteresis in REWOD can be significantly mitigated by selecting an appropriate polymeric coating in contact with the conductive liquid. For example, in this work, a thin film of fluoropolymer (Cytop) has been reported to provide low contact angle hysteresis less than 5°.[34] This configuration minimizes contact line pinning and enhances droplet mobility, enabling more stable and efficient oscillation of the droplet during REWOD operation. Although the study does not provide a direct power density comparison with devices lacking the CYTOP layer, it reports that power densities of their devices containing CYTOP layer can exceed 100 W/m²—and in some cases reaching 1000 W/m².

Previous research on REWOD solely relied on planar electrodes which have a fixed interfacial area, thereby limiting capacitance and consequently limiting power density output.[36,49,99,100] Adhikari et al.[98] perforated Silicon (Si) wafers with numerous micro-sized pores to increase the electrode surface area. Figure 4b shows that the porous electrode is coated with dielectric materials (SiO_2 and CYTOP). A conductive electrolyte is inserted and retracted through the pores under a time varying pulsating pressure, which periodically modulates the electrical capacitance, generating an AC voltage.[103] Without applying any external bias voltage, and for a 38 μm pore-size electrode at a 5 Hz modulation frequency, the maximum current and voltage densities

per unit planar area were 3.77 µA/cm^2 and 1.05 V/cm^2, respectively. Additionally, the root mean square power density was measured to be and 4.8 µW/cm^2.

2.3.2. Increase the contact area difference

For the water-bridge REWOD (as shown in Figure 3c), as described in Section 2.2, the output power is proportional to the difference between the top and bottom contact areas, A_T - A_B.

Moon et al.[35] deliberately modified the wetting properties of the electrodes: the top electrode was made hydrophobic by coating polytetrafluoroethylene (PTFE) onto indium-tin-oxide (ITO) surface, while the bottom electrode (ITO) remained hydrophilic. The reported contact angles for water droplets on these surfaces are 62.5° (top electrode) and 107° (bottom electrode), respectively. Due to the strong pinning effects on the hydrophilic surface, the contact area between the water and the bottom electrode remained nearly constant throughout the oscillation cycle.[97] In contrast, the contact area on the hydrophobic top electrode varied significantly during each oscillation cycle, effectively increasing the difference between the top and bottom contact areas.

Adhikari et al.[99] also used a similar method. In their design, the top electrode was coated with a metal layer that served as a current collector. The bottom electrode was also coated with a metal layer for conduction, followed by a dielectric layer (e.g., Al_2O_3 or SiO_2) and a fluoropolymer coating (e.g., Teflon or CYTOP) to enhance surface hydrophobicity. As a result, the bottom electrode forms a much larger contact angle with the liquid compared to the top hydrophilic surface. Figure 4c shows the video freeze shots of the water bridge at different electrode distances. At the maximum displacement (i.e., when the electrode–electrolyte interfacial area is minimized) of 4 mm, the interfacial area between the top electrode and the electrolyte is slightly larger than that of the bottom electrode. Without using any external bias voltage, AC current generation was demonstrated, achieving a power density of 53.3 nW/cm^2 at an external excitation frequency of 3 Hz with an optimal external load.

Adhikari et al.[48] also enhanced the contact area difference between top and bottom interfaces by increasing the roughness of the bottom electrode through reactive ion etching. As shown in Figure 4d, this modification enabled a maximum power density of 3.18 µW/cm^2 to be harvested from a 50 µL deionized water droplet oscillating

at a 5 Hz, without any applied bias voltage, which is 4 times higher than that achieved with planar electrodes.

2.3.3. Optimizing the dielectric film

An ideal REWOD unit requires a thinner dielectric film with a higher dielectric constant. Calculation results[34] indicate that achieving a capacitance of ~10^2 nF/cm^2 at <100 V requires dielectric films with thicknesses on the order of several hundred nanometers. With this capacitance, calculations show that the resulting power density can reach up to 1 W/cm^2 at a vibration frequency of 50 Hz, thus enabling the fabrication of practical vibration harvesters with power output of several watts. However, both reducing the film thickness and using materials with high dielectric constants lead to a decrease in breakdown voltage.[34] For such nanometer-scale dielectric films, the breakdown voltage exhibits a highly nonlinear dependence on material properties, applied voltage, and polarity.[94,104–106] Local electric fields as high as 10^6 V/cm can develop even at relatively low voltages, leading to charge injection and trapping.[104,105] This effect immobilizes a portion of the electrical charge within the dielectric, hindering charge collection during the dewetting process and thus reducing energy generation efficiency.[34] Consequently, to enhance the output energy, it is necessary to select a dielectric film with a relatively high dielectric constant and lower charge trapping tendency while maintaining a relatively thin thickness.

Krupenkin and Taylor[34] investigated the breakdown characteristics of various dielectric materials. Among the tested materials, oxide films performed poorly, while inorganic fluorides exhibited better performance. The best results were observed with fluoropolymers, such as Cytop[107] and Teflon-like films. However, despite its minimal charge trapping, Krupenkin and Taylor[34] observed in their experiments that Cytop exhibited unreliable breakdown resistance, leading to a higher risk of breakdown, making it less suitable for high-performance applications. In contrast, Ta_2O_5, with its relatively high dielectric constant of 25, demonstrated superior breakdown resistance. Ultimately, to optimize both charge stability and breakdown performance, nanometer-thick multilayer dielectric films were used, which consist of Cytop deposited on Ta_2O_5.[34]

Under the same thickness, dielectric films with higher density have higher breakdown strength and lower leakage current caused by charge trapping, thus enhancing the effective output energy. It is also challenging to use non-vacuum-based

film fabrication methods, such as spray deposition and dip-coating, to obtain dense films with thicknesses in the order of nanometers. Vacuum-based methods, particularly atomic layer deposition (ALD), are ideal due to their self-limiting growth process.[108] ALD thin films have higher dielectric constants, breakdown strengths, and lower leakage currents, making them suitable for REWOD energy harvesting. Yang et al.[100] developed a REWOD energy harvester with an Al_2O_3 ALD film (see in Figure 4e). A 45 nm-thick ALD film was demonstrated to achieve lower leakage current density ($< 10^{-8}$ A/cm^2), higher capacitance (245.19 nF/cm^2), and higher power density (5.59 mW/cm^2) at a bias voltage of 13.5 V.

In subsequent research, Yang et al.[36] developed a laminated structure (see in Figure 4f) that is able to further reduce the leakage current in high-dielectric constant materials. This laminated structure consists of two materials: TiO_2, a high-dielectric-constant material, and Al_2O_3, known for its high electrical resistance and band gap energy.[109] A REWOD energy harvester incorporating this lamination layer achieved a high power density of 15.36 mW/cm^2 at a bias voltage of 30 V, exhibiting lower leakage current and relatively higher capacitance compared to single layer of TiO_2 or Al_2O_3.

To systematically compare the performance differences among various dielectric films, Table 1 summarizes key parameters including material type, fabrication method, thickness, dielectric properties, breakdown voltage, leakage current, and corresponding power density. It is evident that both material selection and processing techniques significantly influence the performance of dielectric films. Future optimization efforts should continue to focus on the synergy between material innovation and structural design.

Table 1. Key performance parameters of various commonly used dielectric films.

Material	Fabrication method	Thickness (nm)	Capacitance (nF/cm²)	Dielectric constant	Breakdown voltage (V)	Leakage current test field strength (MV/cm)	Leakage current density (A/cm²)	Power density test bias voltage (V)	Power density (mW/cm²)	Reference
Ta_2O_5/Cytop	Sputtering + anodic oxidation	<100	16	2/23	~10	N/A	N/A	N/A	N/A	34
Ta_2O_5/Parylene C/Cytop	Chemical Vapor Deposition	200/200/70=470	Not measured	2/3/23	>50	N/A	N/A	N/A	N/A	107
Al_2O_3	Thermal oxidation	101	53	6	40 – 50	4.94	<10^{-7}	N/A	N/A	110
Al_2O_3	Sputter	85	89.27	8.57	18	0 – 1.0	<10^{-2}	12	1.5	100
Al_2O_3	ALD	140	69.61	11.01	>20	0 – 1.0 (Film: 100 nm)	<10^{-8}	13.5	3.38	100
Al_2O_3	ALD	45	245.19	12.46	13.5	0 – 1.0 (Film: 100 nm)	<10^{-8}	13.5	5.59	100
TiO_2/Al_2O_3	ALD	85/65=150	146	24.73	27	0 – 0.8	<10^{-8}	27	14.87	36
Al_2O_3/TiO_2/Al_2O_3	ALD	65/100/65=230	102	26.5	30	0 – 0.8	<10^{-7}	30	15.36	36

19

2.3.4. Increasing oscillation frequency

According to the principle of REWOD, an external force is periodically applied to the electrode, causing the droplet to move or deform, thereby converting mechanical energy into electrical energy. Consequently, increasing the oscillation frequency of droplets can boost harvested power by increasing the number of energy conversion events per unit time and enhancing energy output per oscillation through improving charge transfer dynamics.[34] Typically, achieving high droplet oscillation frequencies requires an external mechanical source operating at similarly high frequencies. However, many common energy sources—such as vibrations from vehicles and machinery, human motion, ocean waves, wind, and structural vibrations—operate at much lower frequencies, generally below several Hz. To circumvent this limitation, Hsu et al.[101] introduced the "bubbler" method, which integrates the REWOD process with the rapid self-oscillating behavior of bubble growth and collapse. The bubbler system (as shown in Figure 4g) comprises three key components: (i) a REWOD chip featuring an array of dielectric-coated circular electrodes, each with a central hole, (ii) a thin membrane separated from the REWOD chip by a small gap, and (iii) a top plate that supports the membrane and facilitates the escape of dielectric fluid. The gap between the chip and the membrane is filled with a conductive liquid that does not wet the membrane. When pressurized dielectric fluid (e.g., air, inert gas, or a dielectric liquid) is supplied through the chip holes, dielectric bubbles form on each electrode. As these bubbles grow, they displace the conductive liquid, reducing the overlap area between the liquid and the electrodes, and thereby inducing an electrical current. The bubbles continue to expand until they touch the membrane, at which point they rapidly collapse as the dielectric fluid escapes. This method does not rely on an external mechanical energy source. Bubble self-oscillation naturally occurs when external pressure is applied to the device. The oscillation frequency is controlled by the gap between the membrane and the electrodes, fluid viscosity, and applied pressure. Experimental results have shown a peak power density of nearly 100 W/m^2 at a bias voltage of 4.5 V, similar to previous outcomes for the conventional REWOD device,[34] due to limitations imposed by dielectric film quality and electrical breakdown stress. Furthermore, the bubbler also has the potential to be scaled up from an output of 10^{-6} W to exceeding 10 W by appropriately adjusting the size of the bubble array, enabling

the fabrication of compact, lightweight energy-harvesting devices with a wide range of power outputs at very low frequencies, well below 1 Hz.

Hsu et al.[49] further investigated the bubble oscillation mechanisms in REWOD systems, proposing an analytical and computational framework to model the collapse and rebound dynamics of the gas-liquid interface. In their formulation, the collapse time $t_{collapse}$ is derived from a balance between the applied pressure difference and the inertia of the surrounding conductive liquid, given by Eq. 13. For the rebound phase, a spherical cap geometry is assumed, and the growth time t_{growth} is expressed as Eq. 14. The total oscillation period T is approximated as the sum of the collapse and growth times, i.e., $T = t_{collapse} + t_{growth}$, and the frequency is estimated as $f = 1/T$. Their results indicate that the oscillation frequency increases with pressure and decreases with bubble radius, while the effects of fluid viscosity and gap thickness are comparatively minor. The model predictions were validated by both CFD simulations and experimental measurements, demonstrating that self-oscillation frequencies exceeding 2 kHz can be achieved under moderate pressures (e.g., $\Delta P \approx 0.08$ bar using mercury). Furthermore, the internal high-frequency response enables energy harvesting even from low-frequency mechanical excitations (< 1 Hz). Reported instantaneous power densities above 10^4 W/m^2 under high-frequency and biased conditions further underscore the potential of bubble-based REWOD systems for efficient energy conversion.

$$t_{collapse} = \sqrt{\frac{\rho R^2}{\Delta P}} \tag{13}$$

$$t_{growth} = \sqrt{\gamma \cdot \frac{\rho R^2}{\Delta P}}, \gamma = \frac{6}{\beta(3+\beta^2)} \cdot \frac{h}{R} \tag{14}$$

where ρ is the liquid density, ΔP is the pressure difference between the gas and the liquid, and R denotes the radius of the conductive liquid inlet boundary, β is the aspect ratio of the bubble, and h is the electrode gap height.

2.4. Applications

Unlike traditional energy harvesting technologies such as electromagnetic, electrostatic, or piezoelectric harvesters, REWOD can effectively capture energy sources that are difficult to utilize by other methods. It enables harvesting energy from various intermittent and aperiodic mechanical forces and displacements in the environment, operating at frequencies ranging from several Hz to well below 1 Hz[101].

This unique capability makes it particularly suitable for scenarios where conventional energy harvesters struggle to operate efficiently. For example, REWOD excels at capturing energy from human motion, making it especially well-suited for powering wearable and implantable devices. These devices typically require power ranging from sub-watt to several watts, such as personal GPS and inertial positioning systems (~0.1 W),[111,112] medical prosthetic devices (~0.1 W to 1 W),[113–115] smartphones (~1 W),[116–118] and two-way radios (1 W to 10 W).[119–121] Additionally, REWOD has also been applied for self-power sensors[101].

2.4.1. Energy harvesting as power sources

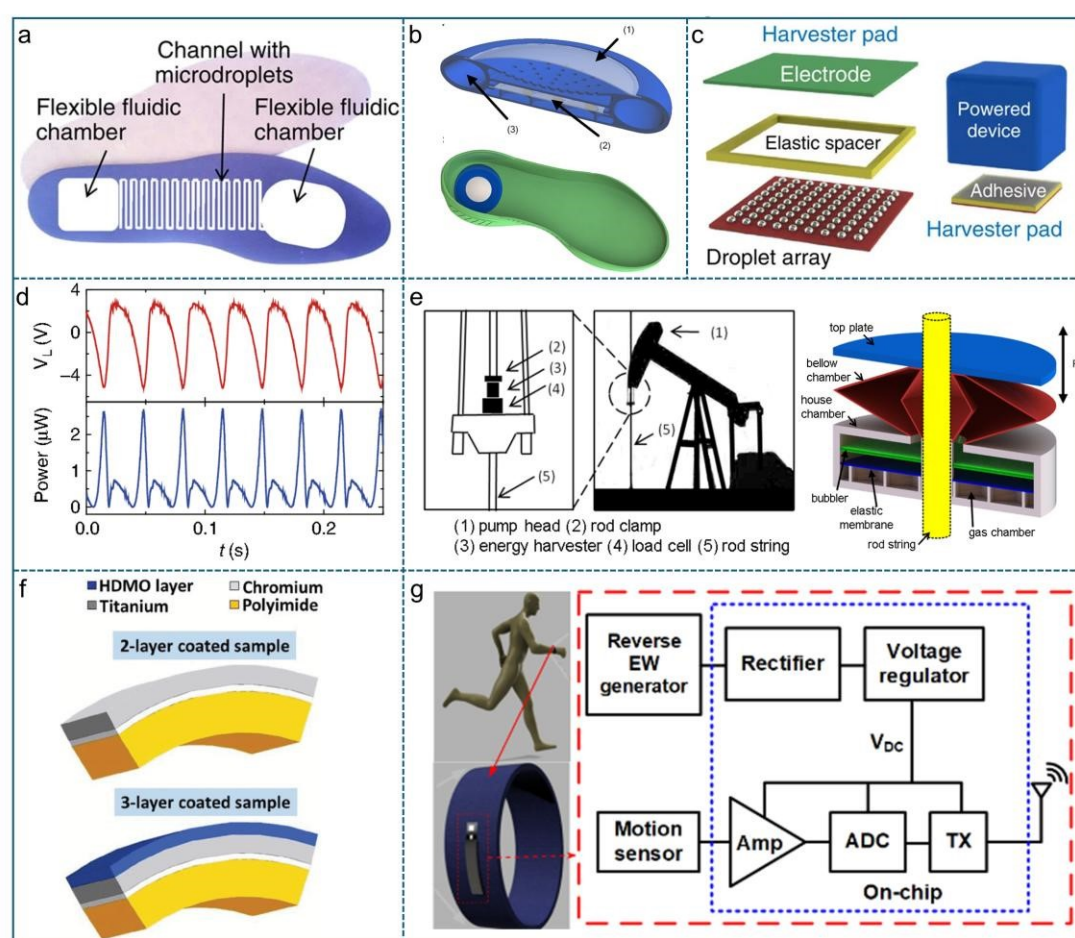Figure 5. Application of REWOD as power sources. a) Schematic of a footwear embedded REWOD microfluidic energy harvester. Reproduced with permission.[34] Copyright 2011, Springer Nature. b) Cross-section of a footwear-integrated energy harvester based on the bubbler approach. Reproduced with permission.[101] Copyright 2015, Springer Nature. c) A REWOD-based vibration harvester. Reproduced with permission.[34] Copyright 2011, Springer Nature. d) Experimental results: voltage drop and instantaneous power with time for the case of a 14 droplets REWOD system. Reproduced with permission.[35] Copyright 2013, Springer Nature. e) (i) Schematics of oil pump and the possible location where to place the bubbler; (ii) The schematics of

the bubbler showing. Reproduced with permission.[101] Copyright 2015, Springer Nature. f). Schematic of flexible electrodes. Reproduced with permission.[122] Copyright 2024, IEEE. g). A REWOD unit for a wearable sensor system. Reproduced with permission.[26] Copyright 2020, IEEE.

In the realm of human locomotion, the concept of harvesting energy using footwear embedded harvesters is well-established.[123–126] Literature[126] indicates that up to 10 W per foot can be generated without adversely affecting gait—remarkably high when compared to the power consumption of mobile devices such as cell phones (~1 W). Krupenkin and Taylor[34] proposed a system comprising a 2-m-long train of 1,000 conductive droplets, each 1 mm in length and separated by 1 mm spacers, confined within a 1-mm-diameter circular channel extending over 4 m (as illustrated in **Error! Reference source not found.**a). This channel occupies an area of approximately 40 cm², less than one-quarter of a typical human footprint. It contains about 4 ml of liquid, making it well suited for integration into footwear. Assuming a heel area of about 20 cm², the required midsole compression to displace this liquid volume is estimated to be around 2 mm, which is small enough to avoid affecting gait. With a film stack capacitance of 16 nF/cm², as reported in the lierature,[34] the average generated power per foot can be estimated to exceed 2 W at bias voltages over 35 V and reach up to 10 W at bias voltages over 75 V. Although increasing the dielectric film's capacitance can further reduce the required bias voltage, the current bias voltage levels do not present a major practical obstacle. After all, standard DC to DC boost converters can easily step up the 3.7 V output of lithium-ion batteries to the necessary voltage.

Hsu et al.[3,12] also illustrate a simple bubbler device (a type of REWOD component mentioned in Section 2.2.3) integrated into footwear to enable energy harvesting from human locomotion (about 1 Hz frequency), as shown in **Error! Reference source not found.**b. Bubbles self-oscillate naturally whenever external pressure is applied to the device, allowing effective coupling with mechanical energy sources across a wide range of forces, displacements, and frequencies. The bubbler chip is located between two chambers filled with the pressurized gas. During the heel strike, the top elastic chamber is compressed, forcing the gas through the REWOD chip and inducing thousands of bubble oscillations, each converting a portion of the heel strike's mechanical energy into electrical energy. During the toe-off process, the compressed gas flows from the bottom chamber back to the top chamber through an auxiliary bypass check valve, completing the cycle. This device was estimated to generate about 1 W of

usable electrical power. These examples demonstrate the feasibility and potential of footwear-based REWOD energy harvesters for powering wearable or portable electronic devices.

The REWOD process can also harvest mechanical energy from vibrations, a common source found in floors, stairs, vehicles, and equipment housings. This process enables novel harvester architectures that greatly increase power output. For example, Krupenkin and Taylor[34] demonstrated a REWOD-based vibration harvester that uses an array of conductive droplets squeezed between two dielectric-coated electrodes, separated by a millimeter-thick elastic spacer, which also acts as a mounting 'pad' for the load device (as shown in **Error! Reference source not found.**c). In this system, mechanical vibrations cause periodic changes in the solid–liquid contact area, generating electrical current. With a film stack capacitance of 10^2 nF/cm^2, the power density can be scaled up to 10^{-1} W/cm^2 at a vibration frequency of 50 Hz, allowing for the development of producing power outputs of several watts.

Additionally, the water-bridge REWOD is well-suited for utilizing vibrations and holds significant potential for future microfluidic power generation systems. This system uses water instead of liquid metal, with the ions in the water serving as charge carriers. It can provide AC current power without requiring an external bias voltage source (shown in **Error! Reference source not found.**d). Moreover, the use of water eliminates the toxicity risks associated with liquid metals.

Hsu et al.[17] introduced another bubbler device capable of harvesting energy from machine motions (**Error! Reference source not found.**e). This device is located at the point where the rod string is attached to an oil pump head and can power the pump load cell and associated equipment. As the pump head moves up and down (about 0.2 Hz frequency), the force exerted by the rod string on the harvester's top plate alternates, causing periodic compression of the bellows chamber. This motion displaces the dielectric fluid contained in the chamber through the REWOD chip, generating electrical power. This device was estimated to generate more than 5 W of electrical power.

Traditional REWOD components rely on rigid planar electrodes, which limits their suitability for powering wearable sensors. For the next generation of these devices, continuous and sustainable operation under various bending conditions, without bias voltage, is essential. To address this limitation, Adhikari et al.[48] developed a bias-free

voltage REWOD component for powering wearable sensors. They used a 3D-printed polydimethylsiloxane (PDMS) and carbon black flexible substrate as the bottom REWOD electrode. The flexible substrate was first coated via electron-beam physical vapor deposition (EBPVD) with ~200 nm Ti conductive layer, followed by ~50 nm Cr adhesion bilayer, and then~200 nm Al_2O_3 dielectric layer. The top conductive electrode was a doped Si wafer coated with a 100 nm Ti layer. Using a 50 μL electrolyte droplet, a maximum AC current of ~340 nA was generated at 2 Hz. This study demonstrated the feasibility of implementing a REWOD for powering wearable sensors using flexible electrodes.[46]

Coating on the polyimide substrate is more consistent compared to PDMS and exhibits greater thermal stability at high temperatures (>200 ℃) encountered during the EBPVD deposition process.[127] Kakaraparty et al. designed a REWOD device using a polyimide sheet (Kapton) as flexible electrode.[44] The top electrode was fabricated on a 0.11 mm polyimide sheet via EBPVD (see in **Error! Reference source not found.**f), with a 50 nm Cr layer followed by a 150 nm Ti layer. The bottom electrode was similarly coated with 50 nm Cr and 150 nm Ti, with an additional 100 nm Al_2O_3 dielectric layer. A 50 μL DI water droplet was encapsulated between the electrodes. When the electrodes were maintained in a planar configuration without any bias voltage, the REWOD generated a maximum power density of 0.002 μW/cm^2 at 5 Hz. When the flexible electrodes were bent to a 60° angle, the power density reached 0.05 μW/cm^2, about 25 times higher than that in the planar state. This is due to the reduced gap between the electrodes in the bent state, which increases the contact area between the electrodes and the electrolyte, thereby leading to a higher capacitance. Moreover, a narrower gap reduces electrical resistance across the electrodes, minimizing energy dissipation.[127] This output is relatively high with no bias voltage and is sufficient to power ultra-low-power bio-wearable chips, which typically require only nanowatt-level power to operate.[128]

Kakaraparty et al.[122] transitioned to a polyimide substrate for the flexible electrodes and employed a sputtering-based physical vapor deposition technique to deposit a high-dielectric metal oxide (MnO_2) onto the polyimide sheet. This modification led to a significant increase in power density, reaching 476.21 μW/cm^2 with a 50 μL droplet. These studies represent an important initial step toward

developing a single electrolyte encapsulated flexible REWOD component, with the long-term goal of characterizing arrays of REWOD structures for future applications.

When considering the entire system, some researchers have begun integrating the REWOD component into circuitry to power motion sensors. Adhikari et al.[66] developed a novel bias-free REWOD unit to power motion sensors, capable of generating an unconditioned AC output of 95–240 mV using a 50 μL droplet of 0.5 M NaCl electrolyte. When integrated with commercial components, this AC signal was rectified, boosted, and amplified. A seven-stage rectifier utilizing Schottky diodes with a forward voltage drop of 135–240 mV and a forward current of 1 mA, converted the AC signal into DC voltage. The boost converter produced approximately 3 V DC, demonstrating the feasibility of this system in powering motion sensors.

Tasneem et al.[26] reported a self-powered motion sensor based on REWOD energy harvesting. The energy harvester (as shown in Figure 5g) includes a rectifier and a voltage regulator to provide the DC supply voltage to the analog front-end and the transmitter for wireless data transfer from the motion sensor. The on-chip circuitry includes a seven-stage voltage-doubler based rectifier, an amplifier, an analog-to-digital converter, and a transmitter. The recycled folded cascode based charge amplifier has a closed-loop gain of 53 dB within the bandwidth of 1150 Hz, which is suitable for detecting low-frequency motion signals. The wireless motion sensing device using REWOD is suitable for quantitatively monitoring the motion-related data as a wearable sensor.

Sah et al.[129] also proposed a REWOD-based system where the REWOD-generated charge is amplified by a charge amplifier with a gain of 2 V/V to improve the signal-to-noise ratio and transmitted to a digital receiver. To prevent power flickering, the rectifier's filter circuit was integrated with a supercapacitor, ensuring a constant power supply for 5 minutes with a power conversion efficiency of over 80% at 1 Hz.
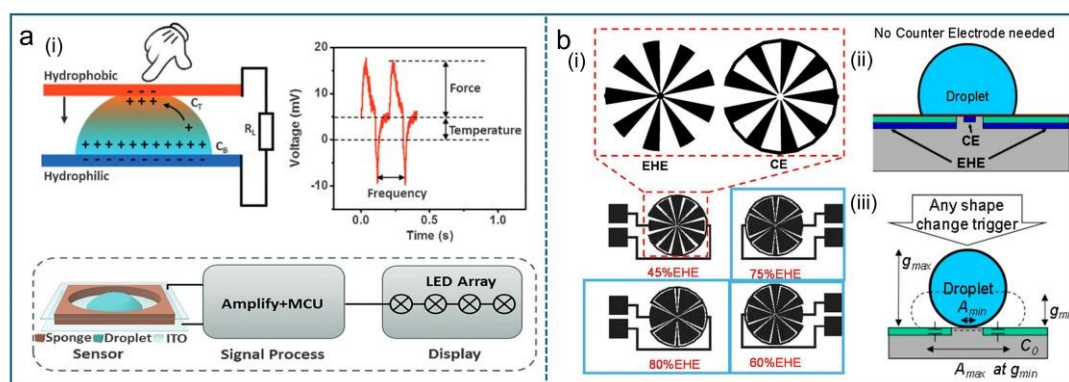
2.4.2. Self-powered sensors

Figure 6. Application of REWOD as self-powered sensors. a) (i) Schematic structure and principle of the sensor; (ii) The voltage-time curve of a droplet-based sensor when a coupled temperature and force stimuli is applied; (iii) Schematic representation of the integral sensing system. Reproduced with permission.[27] Copyright 2016, Wiley. b) (i) The structures of electrode with different EHE area ratios; (ii) Side view of c-planar REWOD configuration, where CE and EHE both situate on the bottom plate, leaving design flexibility on top structures. Reproduced with permission.[130] Copyright 2022, IEEE.

In both everyday life and industrial settings, sensors are essential for precise monitoring and control across various applications. The demand for diverse functionalities has driven the development of sensors based on multiple operating principles, including resistance sensors,[131–133] capacitive sensors,[134] piezoelectric sensors,[135–137] thermoelectric sensors,[138] and field-effect transistor devices.[139] Due to its ability to generate electrical signals in response to external stimuli, REWOD can also function as self-powered sensors, offering several advantages over conventional sensing technologies.

In recent years, temperature- and force-sensing networks have become increasingly important to meet the demands of electronic skins (e-skins) and artificial intelligence systems.[27,140–143] Simultaneous sensing of temperature and force has gained significant attention to mimic the functionality of human skin. To achieve this, most existing designs rely on separate temperature and force sensors, thereby detecting multiple stimuli independently.[144–146] However, developing a true multimodal sensor capable of measuring both temperature and force within a single sensing unit remains a challenge. While some researchers have proposed potential solutions,[147,148] many of these approaches involve nanoscale fabrication or micro-level current/voltage signals, leading to complex manufacturing processes and post-signal processing. Consequently, there is a pressing need for a novel sensing strategy that offers high accuracy while

maintaining a simplified architecture. Liu et al.[27] developed a self-powered multimodal temperature and force sensor based on REWOD and the thermogalvanic effect in a $K_3[Fe(CN)_6]/K_4[Fe(CN)_6]$ droplet, as shown in Figure 6a. The droplet's deformation enables force detection, while the temperature difference across the droplet generates both an alternating pulse voltage and a direct voltage, enabling simultaneous sensing of external force and temperature. To demonstrate this capability, the researchers constructed an integral system in which the droplet sensor responds to both external temperature and force stimuli. The sensor exhibits a displacement detection sensitivity of at least 0.05 mm, while the minimum force detection sensitivity depends on the mechanical properties of the external support structure. Upon receiving an external stimulus (e.g., a single press), the droplet sensor converts it into a voltage signal, which is then amplified and processed by a microcontroller unit. Finally, four two-tone light-emitting diodes respond spontaneously to the stimuli, indicating the object's temperature and the magnitude of the applied force through changes in color and the number of LEDs activated. These results demonstrate the potential of the droplet sensor as a multimodal temperature and force sensing for artificial intelligence applications.

Moyo et al.[130] developed a facile coplanar REWOD structure for sensing applications. Traditionally, REWOD units adopt a two-plate configuration, consisting of a top counter electrode and a bottom energy-harvesting electrode coated with a dielectric layer.[27,34,46] In contrast, the coplanar design integrates both the counter electrode and the dielectric-coated energy-harvesting electrode into a single planar structure. To maintain a constant ratio between the solid-liquid contact area on the bottom dielectric-layer-coated electrode and the total liquid-electrode contact area during the spreading and deformation of a centered droplet, the coplanar electrodes were patterned symmetrically in a "flower petal" configuration (as see in Figure 6b(i)). Figure 6b(ii) and Figure 6b(iii) show side views of the coplanar REWOD configuration. A vibrating top plate (without a metal electrode) can be added to assist in controlling droplet deformation and spreading (The vibrating plate is not shown in Figure 6b). The exposed top surface in this coplanar REWOD structure offers significant potential for expanding sensing applications, such as raindrop energy harvesting. Furthermore, when integrated with flexible/stretchable electrodes, the coplanar REWOD system shows promise for tactile sensing and motion detection in soft robotics.[27,34,46,130,149]

2.5. *Challenges and opportunities*

As highlighted in the reviews, these devices offer a green approach to energy harvesting and hold tremendous potential as a renewable energy source and self-powered sensors by harnessing ambient, low frequency mechanical energy.[24] However, the power output of these devices has yet to reach a significantly high level. Before large-scale implementation and practical deployment of REWOD energy harvesters, several key challenges need to be addressed.

Although classical REWOD units require a bias voltage to charge electrons to improve output power, recent advancements have shifted toward bias-free operation to enhance the practical applicability of REWOD. Despite these advancements, further improvements in bias-free REWOD output energy are necessary. Scaling up power generation in such systems will require precise synchronization and control of thousands of droplets with respect to their positions and velocities.[150] Currently, most studies are limited to proof-of-concept devices using only a single droplet. Future work is expected to focus on the development of electrolyte-enclosed structures incorporating multiple droplets,[127] which would significantly increase the electrolyte–electrode interfacial area, thereby enhancing interfacial capacitance and overall power output. Furthermore, future research should further investigate the effects of dielectric film thickness, variations in electrolyte volume, and electrolyte composition on overall device performance, as well as the development of high-dielectric constant metal oxide-coated array structures.[44,122] These efforts will collectively contribute to improved output power and energy conversion efficiency, advancing the development of practical and scalable REWOD systems.

In addition, advances in flexible electrode technology are essential. The development of flexible conductive materials with good electrical conductivity and mechanical stability, as well as the ability to accommodate deformations such as bending or stretching, can ensure the stable performance of REWOD systems under practical operating conditions. Furthermore, integrating flexible electrodes with micro-structured surfaces is expected to further enhance droplet control and improve energy conversion efficiency.

Moreover, eliminating reliance on costly materials and complicated fabrication processes is another critical factor for large-scale adoption. Enhancing output by evaluating commercial off-the-shelf metalized polymer films for REWOD or

experimenting with spin coating to deposit low-cost dielectric layers for REWOD electrodes are promising directions for further research.[45,46,151,152]

3. Triboelectric nanogenerators (TENGs)

3.1. Basic working principle

Since developed by Zhong Lin Wang's research team in 2012,[153] TENGs have gained prominence in self-powered sensing,[69,154–156] environmental energy harvesting,[29,157–159] low-frequency power generation[160] etc. Unlike traditional electromagnetic generators that depend on coils and magnets, TENGs utilize the interaction between triboelectrification (contact electrification) and electrostatic induction, making them well-suited for capturing mechanical energy from movements such as human motion,[161] ocean waves,[162] and environmental vibrations.[163] When two triboelectric materials with differing electron affinities come into contact and then separate, electrons transfer from the material with a lower electron affinity (which easily loses electrons) to the material with a higher electron affinity (which tends to gain electrons). This charge transfer process creates an electrostatic potential difference between the materials, leading to localized charge accumulation on their surfaces. When an external circuit is connected, this potential difference induces electron flow through the circuit and generates electricity.

While the basic working principle of TENGs can be described through contact electrification and electrostatic induction, a deeper and quantitative understanding of their current generation mechanism requires a shift to electromagnetic theory. Classical Maxwell's equations were originally formulated for static or uniformly moving media, and do not fully account for the dynamic interfacial charge redistribution and moving dielectric boundaries intrinsic to TENG operation. Recent theoretical advancements particularly those by Wang's group highlight the critical role of displacement current in TENGs, and propose extensions to the conventional Maxwell framework to incorporate moving dielectric interfaces and time-dependent surface polarization.

Maxwell's equations, formulated by James Clerk Maxwell, describe the fundamental interactions between electric field, magnetic fields, charge density and current density.[164] In Maxwell's equations, the displacement field (D) is generally expressed as:[165]

$$D = \varepsilon_0 E + P \tag{15}$$

where P denotes the polarization vector, E represents electric field and ε_0 represents the vacuum permittivity. In isotropic materials, this simplifies to $D = \varepsilon E$, where ε is the material's permittivity. In the absence of an external electric field ($E = 0$), polarization does not occur ($P = 0$), eliminating displacement current $\frac{\partial D}{\partial t}$. However, in practical scenarios, polarization can also arise from strain-induced effects (piezoelectricity) and surface contact-electrification (triboelectricity), which are independent of an applied electric field.[165] In TENGs, surface charges form due to physical contact between different materials. To incorporate the effects of contact-electrification-induced electrostatic charges, Wang[164] introduced an additional surface polarization term P_s in the displacement field expression:

$$D = \varepsilon_0 E + P + P_s \tag{16}$$

Here, the term P accounts for polarization due to an external electric field, while P_s represents surface charges arising from contact electrification. Unlike P, P_s is independent of any applied electric field and represents the polarization induced by mechanical motion, generated due to the relative movement of charged media surfaces triggered by mechanical action. By substituting Eq. 11 into Maxwell's equations and defining:

$$D' = \varepsilon_0 E + P \tag{17}$$

Maxwell's equations can be rewritten as a new set of self-consistent equations such as:[165]

$$\nabla \cdot D' = \rho_f - \nabla \cdot P_S \tag{18}$$

$$\nabla \cdot B = 0 \tag{19}$$

$$\nabla \times E = -\frac{\partial B}{\partial t} \tag{20}$$

$$\nabla \times H = J + \frac{\partial D'}{\partial t} + \frac{\partial P_S}{\partial t} \tag{21}$$

where B represent the magnetic field, while H is the magnetization field, ρ_f is the free charge density, and J is the current density. Here, the total displacement current is:

$$J_D = \frac{\partial D'}{\partial t} + \frac{\partial P_S}{\partial t} \tag{22}$$

The term $\frac{\partial D'}{\partial t}$ corresponds to the displacement current arising from the time-dependent variation of the electric field. Meanwhile, $\frac{\partial P_S}{\partial t}$ describes the current generated due to changes at the material boundaries, commonly known as the Wang term.[166] These expressions serve as key foundations for analyzing the output characteristics of TENGs.

31

Further, If the surface charge density function $\sigma_{s(r,t)}$ on the material surfaces is defined by a shape function $f(r,t)$, where time t accounts for the instantaneous shape of the material under external influence (Figure 7.), then the equation for P_s can be expressed as:[165]

$$P_s = -\nabla \varphi_{s(r,t)} \tag{23}$$

where φ_s represents the surface potential generated by charge transfer. The expanded form is[165]

$$P_s = -\frac{1}{4\pi} \nabla \int \left[\frac{\sigma_{s(r',t')}}{|r-r'|} \right] ds' \tag{24}$$

The total displacement current is obtained by integrating the current density over the surface of the receiving electrode (Figure 7. b)[166]

$$I_{D(t)} = \int \left[\frac{\partial D'(r,t)}{\partial t} + \frac{\partial P_{s(r,t)}}{\partial t} \right] ds \tag{25}$$
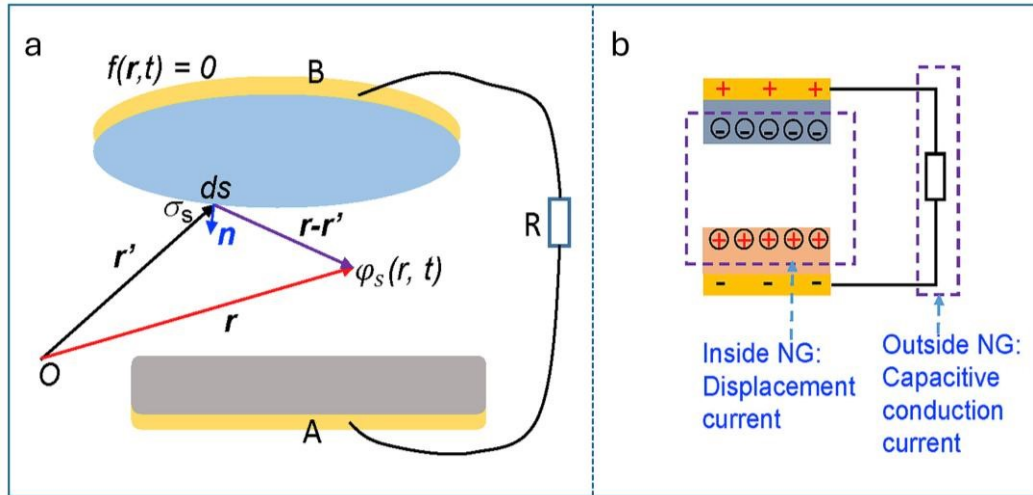

Figure 7. a) A schematic illustration of a TENG connected to an external load, along with the corresponding coordinate system used for mathematical modeling and analysis. b) Schematic showing Displacement current and conduction current in TENG. Reproduced with permission.[165] Copyright 2020, Elsevier.

Additionally, the voltage across the TENG is determined by the path integral of the electromotive force.[166]

$$V(t) = \int [E(r,t) + v(t)B(r,t)]dL \tag{26a}$$

Here, $v(t)$ represents the translational velocity of the moving medium such as dielectric or electrode surface. The term $v(t)B(r,t)$ represents the electric field induced by mechanical motion through the magnetic field, contributing to the total voltage induced across the device. If the surface integral is taken over a fully enclosed surface, applying the law of charge conservation gives[166]

$$I_D(t) = \frac{\partial}{\partial t} \int \nabla \cdot [D'(r,t) + P_s(r,t)]dr = \frac{\partial}{\partial t} \int \rho \, dr = \frac{\partial Q(t)}{\partial t} \tag{26b}$$

Lab on a Chip Accepted Manuscript

Here, Q represents the total free charge on the electrode. Eq. 26 serves as the fundamental basis for formulating the transport equations in TENGs. And the power supplied to the load across R is given by[166]

$$p = \left(\frac{\partial Q}{\partial t}\right)^2 R \tag{27}$$

Having established the fundamental principles and the expression for the generated power in TENGs, we now turn our attention to practical developments and applications. In recent years, TENG has emerged as a promising approach for energy conversion and harvesting, with significant studies made in the contact electrification between the solid materials.[167] A solid–solid TENG involves the interaction of two solid surfaces, typically relying on periodic contact and separation or sliding to generate triboelectric charges. Despite significant research efforts, certain challenges remain due to the inherent properties of solids. Issues such as wear[168] and heating during friction[168] reduce the durability and efficiency of TENGs. Additionally, due to surface roughness and microscopic irregularities,[169,170] achieving full contact between solid materials is difficult. External factors like humidity[171] further impact electrical output. Moreover, electric breakdown[172–174] at the solid–solid interface causes electron loss, significantly reducing performance.

To overcome these limitations, researchers have turned their attention to liquid-based TENGs, which utilize the fluid nature of liquids to achieve more reliable and efficient contact electrification. Their fluidity[175] ensures full contact, reducing wear[176] during the process. Humidity has little or even no impact, especially when using water.[177] In this section, we will focus on liquid based TENGs, specifically liquid–solid TENGs, where a liquid interacts with a solid surface and liquid–liquid TENGs which involve contact between two immiscible liquids. Although contact electrification at liquid–gas interfaces have also been studied,[178,179] but research in this area remains limited. The low density of gas and the slow motion of liquid make it difficult to achieve sufficient contact electrification for direct observation.[180]

Operational Modes of TENGs

TENG operates in four primary modes based on charge transfer mechanisms including:[181] contact-separation mode, sliding mode, single electrode mode, and freestanding tribo-electric layer mode.

1. **Contact-separation mode:**[182] In the contact-separation mode (Figure a), charge transfer occurs as a liquid repeatedly comes into contact with and separates from a dielectric surface (insulating polymer film). When the liquid first makes contact, triboelectric charging occurs due to the difference in electron affinity between the two materials. The solid dielectric layer acquires negative charges, while the liquid retains positive ions, forming an EDL at the interface. As the liquid retracts from the dielectric, the electrostatic potential difference between the two electrodes increases. This potential difference drives electron flow through the external circuit, generating current. This mode is advantageous for energy harvesting from mobile objects without requiring grounding.[181] And it is usually used in energy harvesting from discrete mechanical motions such as water droplets,[183] as well as from environmental mechanical motion or surface vibrations.[184,185] Additionally, it finds applications in sensing tasks such as liquid detection and biomedical monitoring.[186]

2. **Sliding mode:** The sliding mode (Figure b) operates on a similar contact separation triboelectric principle but involves lateral movement of a liquid film or flow over the solid surface. A well-known demonstration of this mode is provided by Lee et al.[187] where an aluminum plate coated with PTFE slides periodically in and out of water. When the PTFE surface contacts the water, contact electrification occurs and electrons transfer from water to PTFE, making the PTFE negatively charged and the water positively charged. As the plate emerges from the water, the separation of charged surfaces induces a potential difference between the underlying aluminum electrode and the water, causing electrons to flow through the external circuit and generate current. This current reaches its peak when the PTFE is fully out of the water. As the plate slides back in, the process reverses electrons flow in the opposite direction, completing the AC cycle. This repeated immersion and emergence modulates the electric field and charge distribution, enabling stable AC generation in the sliding-mode TENG. This mode is generally used for harvesting energy from fluid flow or oscillating liquid interfaces, as seen in designs like that of Nahian et al.[188] for water flow energy harvesting.

3. **Single-electrode mode:** The single-electrode mode (Figure c) operates on the triboelectric principle but differs from other modes by utilizing a single grounded electrode instead of a pair. For example, as explained by Lin et al.[189] when a water droplet falls onto a PTFE-coated surface (dielectric surface), triboelectric charging occurs due to differences in electron affinity, leaving the PTFE negatively charged while the droplet retains positive ions, forming an EDL. As the droplet spreads or moves away, the charge equilibrium is disrupted, creating a potential difference between the grounded electrode and the surface. This imbalance induces electron flow from the electrode to the ground, generating a negative current pulse. When another droplet impacts the surface, the pre-existing negative charges on PTFE attract positive ions from the new droplet, reversing the potential difference and causing electrons to flow back from the ground to the electrode, generating a positive current pulse. As a result, the repeated droplet impacts generate a continuous AC output. It is usually used to harvest energy from falling droplets,[159] such as in rainfall collection or from condensed droplets captured from fog,[158] and detecting liquid or water leakage in containers and pipelines.[190,191]

4. **Freestanding triboelectric-layer mode**: In the freestanding mode of TENG, a pair of electrodes is typically positioned symmetrically beneath a thin dielectric surface (Figure d). As liquid moves across this dielectric layer, charges are generated due to the friction between the liquid and the solid. Simultaneously, the underlying electrodes experience electrostatic induction. As the liquid continues to travel across the surface, the distribution of induced charges becomes uneven, creating a potential difference between the two electrodes.[192,193] This potential drives electron flow through the external circuit, resulting in AC output that reflects the direction and motion of the liquid. This mode enables energy harvesting from a moving object while keeping the system mobile and independent of grounding[181] and is usually used to harvest energy from water waves[194] and for fluid flow sensing[195] using the movement of liquid across the surface to induce charge between electrodes.
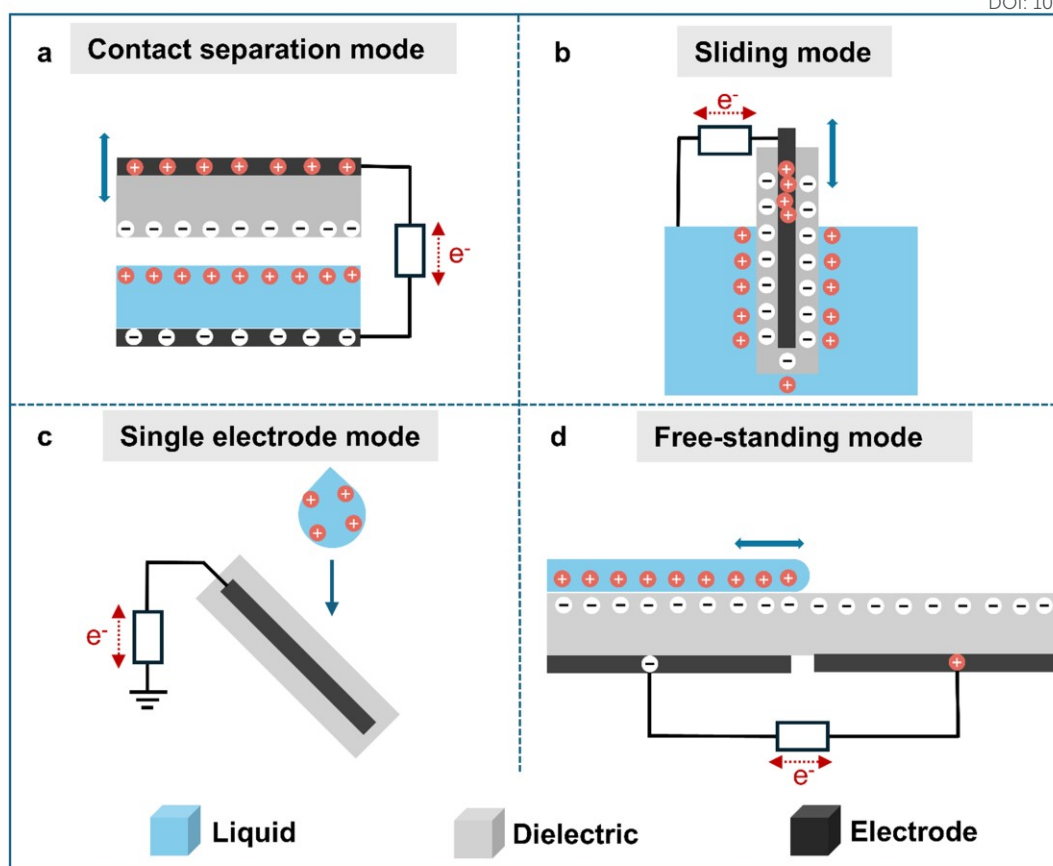
Figure 8. Basic modes of operation. (a) Contact-separation mode, (b) Sliding mode, (c) Single-electrode mode (d) Free-standing mode TENGs, respectively. Blue bidirectional arrows indicate the periodic mechanical motion. Red bidirectional arrows labeled "e⁻" represent the cyclic electron flow in the external circuit that changes direction during different phases of the mechanical cycle.

Since Lin et al. first introduced liquid-solid TENGs in 2013,[182] this technology has undergone significant development. Initially they designed a system where a PDMS surface interacted with water inside a tank, generating electricity through periodic contact and separation. Over time, liquid-solid TENGs has evolved to capture energy from droplets, waves, and fluid motion.[196–198]

A thorough understanding of contact electrification at the liquid interface is critical for improving Liquid based TENG performances. Xu et al.[199] developed the electron-cloud-potential-well model, often termed the "Wang Transition" model, to describe electron transfer mechanisms at material interfaces. When two materials come into contact, electrons transfer due to an asymmetric double-well potential created by overlapping electron clouds (Figure 7). As the materials separate, the transferred electrons remain trapped in the receiver material due to a potential barrier. However, as temperature increases, this barrier weakens, making it easier for electrons to escape.
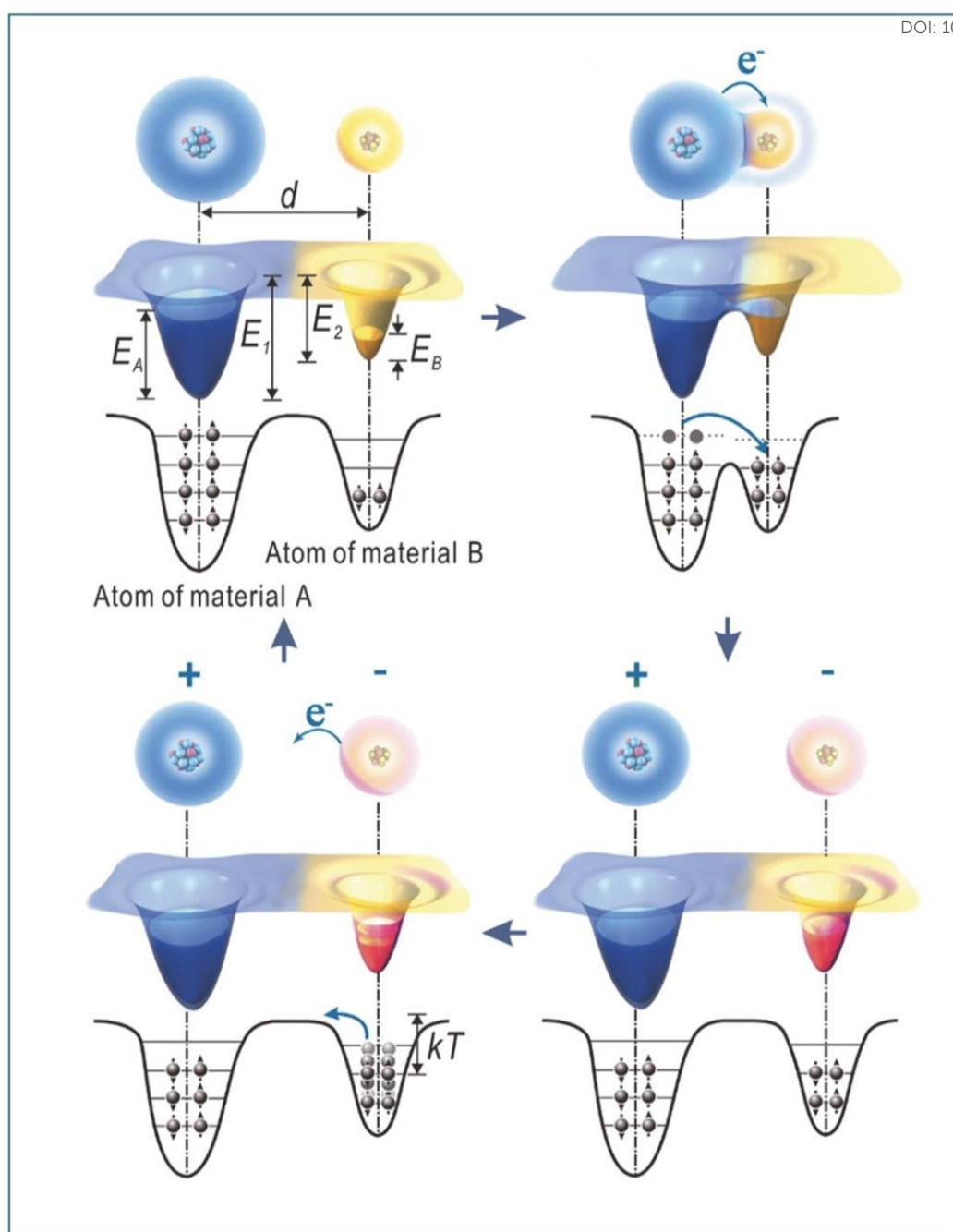
Figure 7. Electron-cloud-potential-well model. Reproduced with permission.[199] Copyright 2018, Wiley-VCH GmbH.

Various theoretical and experimental studies have been carried out to better understand the mechanisms of contact electrification showing electron transfer dominance at the interface. At the atomic level, theoretical models confirm that electron transfer occurs during contact electrification.[200] Nan et al. used density functional theory (DFT) to study how electrons transfer between water and seven commonly used polymers in liquid-solid TENGs. They analyzed factors like bonding style, functional groups, work function, and contact distance affecting electron movement. Their

findings showed that the LUMO (lowest unoccupied molecular Orbital)-HOMO (highest occupied molecular orbital) energy gap plays a key role in determining the strength of electron transfer.[201,202] Similarly, molecular dynamics simulations have verified electron transfer at the Pt(111)-water interface in water-metal interactions.[203] Experimental studies have further substantiated electron transfer in contact electrification and revisited the formation of the EDL, previously believed to be primarily driven by ion transfer.[204,205] For water-polymer interactions, Nie et al.[206] examined charge transfer in droplets contacting a PTFE membrane. Their findings demonstrated that the observed charge transfer significantly exceeded predictions based solely on the ion-transfer model, indicating that electron transfer is the predominant mechanism at the liquid-solid interface, accounting for over 90% of total transferred charges.

Various studies including above ones have provided strong evidence for the "two-step" mechanism proposed by Wang et al.[207] in explaining how the EDL forms at the liquid-solid interface. In the first step, electron transfer occurs when the liquid comes into contact with the solid surface. This process leads to the formation of a sparse distribution of surface charges, meaning that only a small fraction of atoms on the solid surface (i.e., approximately one in every 30,000) carries a charge. In the second step, ions present in the liquid reorganize near the interface due to electrostatic forces. These ions arrange themselves in response to the surface charge, creating EDL.

Building on the understanding of contact electrification and EDL formation at the liquid-solid interface, these factors need special consideration for optimizing the performance and stability of TENGs: material selection, surface modification, and environmental control. When choosing solid materials for liquid-solid TENG, their position in the triboelectric series[208] matters. This relative position in the triboelectric series helps determine how well they gain or lose electrons when in contact with a liquid. A stable electron and ion transfer direction at the interface improves charge transfer, making the TENG more efficient. PDMS, fluorinated ethylene propylene (FEP), polyethylene terephthalate (PET), and PTFE are commonly used solid materials in liquid-solid TENG due to their strong hydrophobic nature and high tribo-negative characteristics. Likewise, using deionized (DI) water is preferable because ionic screening in more conductive solutions can hinder electron transfer.[206,209,210] In general, as ion concentration increases beyond a certain threshold, excess ions accumulate near

the solid surface, resulting in screening effects that weaken the interfacial electric field and suppress charge transfer efficiency.

The efficiency of charge transfer in liquid based TENGs is closely linked to surface properties. Hydrophilic surfaces favor ion-based transfer through ionization reactions, while hydrophobic surfaces primarily support electron transfer.[211] Environmental factors, such as high temperatures, can further reduce performance by causing thermionic charge leakage.[211] Despite ongoing research, the power output of liquid–solid TENGs remains limited typically below $1\,W\,m^{-2}$ due to fundamental constraints at the interface.[212] For instance, increasing surface roughness of hydrophobic surface can enhance charge transfer. However, if the roughness is too high, it may trap air at the solid–liquid interface, which reduces effective contact and limits electrification. As a result, optimizing wettability requires balancing contact area and hydrophobicity. These interfacial factors ultimately restrict surface charge generation. Strategies to address such challenges are discussed in detail in Section 3.2.

3.2. Strategies to improve electrical output

To overcome the limitations discussed above, recent developments have focused on strategies such as charge injection[213,214] to boost surface charge density, surface functionalization to improve interface charge transfer, and wettability engineering including superhydrophobic and slippery liquid infused porous surfaces (SLIPS) to enhance liquid motion. In parallel, structural innovations like bulk-effect-based electrode configurations,[90] and hybrid systems[215] have demonstrated significant improvements in output and stability.

3.2.1. Increase surface charges

To increase surface charges, a commonly adopted approach is to embed additional charges directly onto the tribo-surface through techniques such as electrowetting-assisted charge injection and corona charging. The theoretical importance of increasing surface charge has also been quantified through a device-level figure of merit (FOM) model developed by Peng et al.[216] Their work demonstrates that the output power density (P) of a TENG is quadratically proportional to the surface charge density, i.e., $P \propto \sigma_s^2$. The FOM is expressed as:

$$FOM_{device} = 0.064 \times \frac{(\sigma_s^2 \bar{v})}{\varepsilon_0} \qquad (28)$$

where $\bar{v}$ is the average mechanical actuation velocity and ε_0 is the vacuum permittivity. This relationship provides a simple yet robust mathematical framework to understand how even modest improvements in σ_s, achieved via charge injection techniques, can significantly enhance output power, aligning with experimental observations. For example, Wu et al.[213] significantly improved the kinetic-to-electrical energy conversion efficiency by pre-charging silicon wafers coated with a hydrophobic amorphous fluoropolymer. Through combined high-speed imaging and electrical measurements, they systematically studied droplet impact conditions such as drop height, tilt angle, and surface charge density and their effects on energy harvesting. For silicon wafers pre-charged via electrowetting-assisted charge injection (EWCI), the surface charge density ranged from −0.07 to −0.35 mC/m². Additionally, they tested ITO coated surfaces (amorphous fluoropolymer), where repeated identical droplet (more than 500) impact led to charge densities between −0.12 and 0.16 mC/m². Their findings demonstrated that higher surface charge densities notably increased electrical output, with peak currents reaching up to 2.2 mA, leading to a record energy conversion efficiency of approximately 2.5%, significantly surpassing previous reports of 0.01%.[90,189]

In another related study, Wu et al.[214] introduced a charge trapping-based electricity generator that employed an advanced homogeneous electrowetting-assisted charge injection method (**Error! Reference source not found.Error! Reference source not found.**a). By pre-charging hydrophobic fluoropolymer surfaces, they obtained an exceptionally high and stable negative surface charge density of 1.8 mC m⁻². This innovative approach yielded unprecedented performance metrics, including instantaneous currents exceeding 2 mA, power densities surpassing 160 W m⁻², and energy conversion efficiencies exceeding 11%. These results further validate pre-charging as an effective method to substantially enhance TENG performance.

Jang et al.[217] proposed a monocharged electret technique for improving surface charge density in liquid-solid TENGs (**Error! Reference source not found.Error! Reference source not found.**b). By employing a simple corona charging method to pre-inject stable negative charges into an amorphous fluoropolymer layer, they achieved an exceptionally high surface charge density (as demonstrated by the significant increase in electrical output). For instance, compared to pristine FEP which generated only ~4 V, corona-charged FEP produced 17 V (~4 times increase), while

corona-charged cyclized perfluoro-polymer (CYTOPcorona) reached ~130 V (~33 times increase). This pre-charging approach led to a remarkable 1000-fold improvement in peak power output, increasing from ~1 µW in pristine FEP to 1 mW in CYTOPcorona. Furthermore, the injected charges exhibited excellent stability, maintaining ~80 V output even in highly conductive electrolyte solutions (e.g., 1 M NaCl) which typically degrade TENG performance. Even after two days, the charge-stabilized surface retained 15 times higher output voltage than uncharged FEP, confirming the long-term effectiveness of charge injection. Their results further illustrate the substantial potential of pre-charging techniques in enhancing TENG robustness and performance.
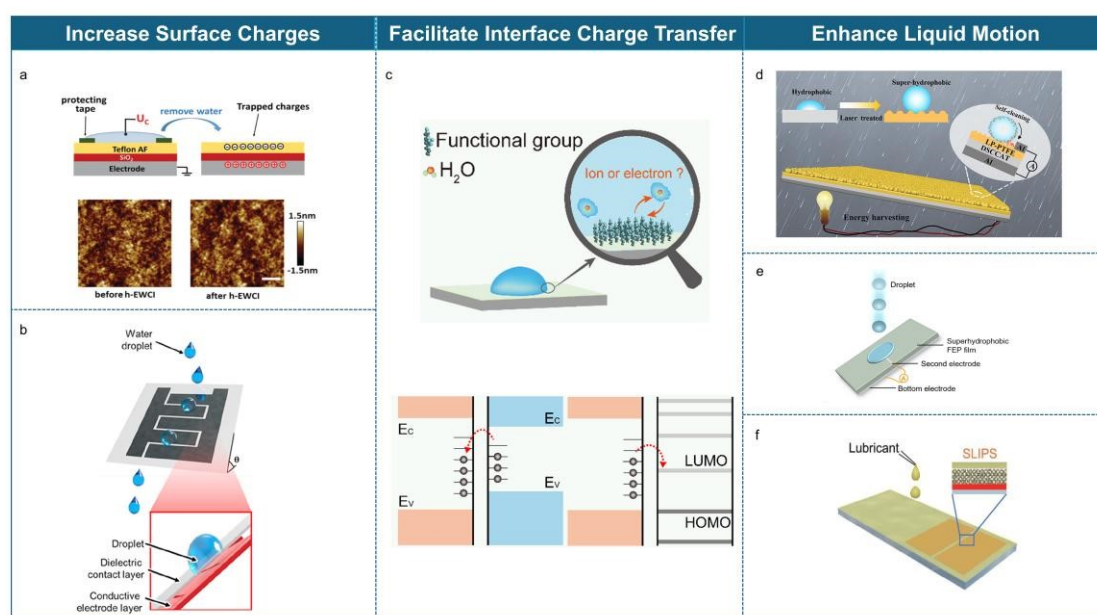

Figure 8. Increase surface charges by a) charge injection using homogeneous-EWCI method. Reproduced with permission.[214] Copyright 2020, Wiley-VCH GmbH. b) corona charging on CYTOP surface Reproduced with permission.[217] Copyright 2020, Elsevier. c) functional group impact on SiO₂ surfaces using silane coupling agents Reproduced with permission.[218] Copyright 2020, American Chemical Society. Enhance liquid motion by d) laser direct writing method for PTFE surface wettability. Reproduced with permission.[219] Copyright 2023, American Chemical Society. e) reactive ion etching modifying FEP surface Reproduced with permission.[220] Copyright 2021, Wiley-VCH GmbH. and f) novel SLIPS-TENG. Reproduced with permission.[221] Copyright 2019, Oxford University Press.

Where electrowetting-assisted charge injection and corona charging embed extra charge within the surface layer, an alternative route is to store charge in a subsurface capacitor and discharge it only at the moment of droplet contact. This internal-reservoir strategy avoids both surface ion screening and the lengthy waiting intervals required between successive impacts of droplets. Wu et al.[222] exemplify this

approach with the first externally charge-pumped liquid–solid TENG. A high-insulation ceramic layer beneath a super-hydrophobic Kapton/FEP film acts as a charge-storage capacitor that is continuously biased by a rotary triboelectric pump fitted with a coaxial polarity commutator (Figure 11a). When a 50 µL water droplet spreads and briefly bridges the pre-charged ceramic to an offset aluminum strip, the stored electrons are released as a displacement-current burst. This design delivers a short-circuit current density of 50.31 µA cm^{-2} and a peak power density of 231.8 W m^{-2}, a 1.43-fold improvement over the previous liquid–solid record; a single droplet can light 600 commercial LEDs, and a continuous droplet train sustains stable output for 30 min in a 3 × 3 array test. These results establish external charge pumping as a powerful means of elevating surface charge density and, consequently, overall TENG performance.

After showing that a mechanical pump can "force-feed" the surface with charge from below, we next look at a strategy where visible light becomes the charger itself, growing fresh trap sites inside the tribo-layer every time it shines. Chen et al.[223] boosted a PDMS-based TENG by embedding a g-C$_3$N$_4$/MXene–Au carbon-cluster composite into the tribo-layer. Under ≈60 mW cm^{-2} visible-light irradiation, g-C$_3$N$_4$ creates photo-generated carriers that act as charge traps, while Au nanoclusters (via surface-plasmon "hot" electrons) and highly conductive MXene sheets stabilize additional carriers, together building a dense trap network that allows much greater charge accumulation per cycle (Figure 11b). A 4 cm × 4 cm device employing this composite delivered an output voltage of 510 V, a current of 80 µA, and a peak power of 20 mW at impedence of 2 MΩ and output power density of 12.5 µW mm^{-2} representing roughly a six-fold improvement over an undoped PDMS control, while its internal impedance dropped by about 50 %.

Surface charge density in triboelectric nanogenerators is typically governed by the intrinsic chemical and physical properties of materials, which sets a natural upper bound for output performance. To overcome this limitation, Shao et al.[224] developed a field-effect-enhanced droplet electricity generator (FE-DEG), where a bias voltage is applied to a bottom electrode to regulate the surface potential at the dielectric interface. The device consists of a p-doped silicon bottom electrode, a thermally grown SiO$_2$ dielectric layer (~2 µm), and a spin-coated Hyflon top layer that provides hydrophobicity and serves as the contact surface (Figure 11c). Upon applying a bias

Lab on a Chip

voltage, an electric field is established across the dielectric, inducing polarization and pre-conditioning the surface prior to droplet impact. This pre-polarized interfacial state enhances droplet–solid contact electrification, resulting in increased charge transfer. The authors demonstrated real-time modulation of charge output by adjusting the gate voltage, confirming dynamic tunability of device performance. Under optimized conditions, the FE-DEG achieved a peak instantaneous power density of 576.1 W m^{-2} at a load resistance of 6.2 kΩ. Additionally, the device exhibited stable output under humid environments and across a pH range of 4 to 11. The charge output of the FE-DEG exceeded that of several previously reported droplet energy harvesting devices, validating the effectiveness of the field-effect modulation strategy. By enabling electrostatic control of surface potential without altering material composition, this method introduces a robust and tunable mechanism for enhancing energy harvesting efficiency.
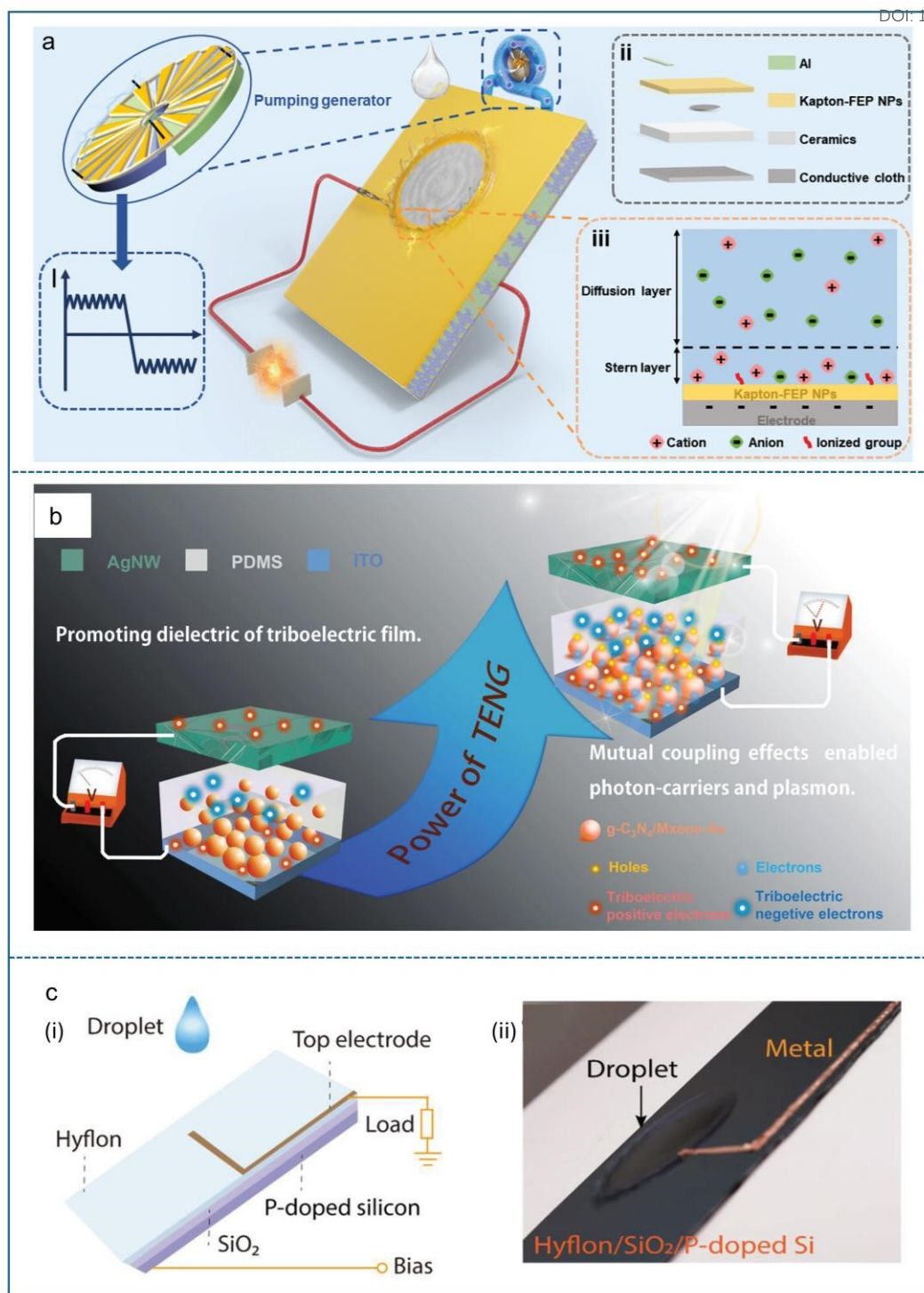
Lab on a Chip Accepted Manuscript

Figure 11. a) Externally charge-pumped liquid–solid TENG. Reproduced with permission.[222] Copyright 2024, Wiley-VCH GmbH. b) enhance TENG performance through charge trapping facilitated by photon-induced carrier generation.[223] Copyright 2021, Wiley-VCH GmbH. c) field-effect-enhanced droplet electricity generator.[224] Copyright 2023, Wiley-VCH GmbH

3.2.2. *Facilitate interface charge transfer*

Addition of chemical/functional groups to the solid surfaces alters the material's ability to donate or accept charges, enhancing its surface charge density and interfacial charge transfer characteristics. In addition to methods that actively inject charge onto a surface, surface chemical functionalization offers a direct and material-selective approach to increasing surface charge density in TENGs.[225] Since the fundamental driving force for contact electrification is rooted in the chemical potential difference between two interacting surfaces, modifying the terminal functional groups on a dielectric can effectively tune its surface potential.[226] This allows for enhanced charge transfer characteristics at the interface without altering the bulk material. Given that the output power of TENGs scales quadratically with surface charge density, as discussed in Section 3.2.1, such surface-specific chemical tuning provides a powerful strategy for performance optimization. This modification increases the surface potential difference between the solid-liquid interface, thereby improving charge transfer efficiency and enhancing triboelectric performance.[215]

Lin et al. [218] examines how different chemical functional groups affect electron and ion transfer in contact electrification between liquids and silicon dioxide (SiO_2) surfaces. The researchers modified SiO_2 using silane coupling agents with perfluorododecyl, oxypropyl, dodecyl, and aminopropyl groups to see how these changes impact charge transfer. They found that both electrons and ions contribute to contact electrification when DI water is used, but electron transfer is more affected by surface functional groups. Perfluorododecyl, which has a high electron affinity, tends to gain electrons, while aminopropyl, with low electron affinity, donates electrons. However, when organic liquids like cyclohexane and dichloromethane were used, electron transfer became the main mechanism since these liquids do not contain free ions. Importantly, the study found that electron transfer in organic liquids does not depend on functional groups because these liquids lack the ability to influence electron exchange significantly. To explain these effects, the researchers proposed an energy band model (**Error! Reference source not found.Error! Reference source not found.**c) showing how functional groups change electron energy barriers and charge transfer efficiency. When a solid like SiO_2 comes into contact with a liquid, electron transfer occurs based on their energy band structures. In DI water, hydrogen bonding and dissolved ions create impurity states, which introduce additional energy levels.

Since these states are at a higher energy level than the surface states of SiO_2, electrons transfer from water to SiO_2, leading to charge redistribution. This transfer can be influenced by surface functionalization with high electron affinity groups (e.g., perfluorododecyl) which introduce low-energy unoccupied states, increasing electron transfer from water to SiO_2, whereas low electron affinity groups (e.g., aminopropyl) introduce high-energy occupied states, making SiO_2 more likely to donate electrons to water. In contrast, organic solvents lack hydrogen bonding and impurity states, so charge transfer occurs through their molecular orbitals. When SiO_2 contacts an organic solvent, electrons move from its surface states to the LUMO of the organic molecules, causing SiO_2 to become positively charged. However, because molecular orbitals are localized and discrete, electron transfer is highly limited (typically at most two electrons per molecule), and modifying the SiO_2 surface has minimal effect on charge transfer with organic solvents. This distinction highlights how electron transfer in water is strongly influenced by surface functionalization, while in organic solvents, it follows a more restricted molecular orbital model. These changes affect how much charge stays on the surface after contact.

In another study, Vu et al.[227] developed a high-performance liquid-solid TENG using a functionalized polyvinylidene fluoride (PVDF) membrane, modified with silica nanoparticles (SiNPs) and 1H,1H,2H,2H-perfluorooctyltriethoxysilane (FOTS), forming the FOTS/SiNPs/PVDF (FSiP) membrane. The proposed membrane integrates fluorine-bearing silane chains, which enhance interfacial polarization, significantly improving its hydrophobicity and dielectric constant. These enhancements lead to a 10.8-fold increase in power density to 420 mW/m², along with improved current (5.79 µA) and voltage (28.3 V) output.

3.2.3. *Enhance liquid motion (surface wettability)*

Surface wettability significantly influences the performance of liquid-solid TENGs by affecting both charge transfer and liquid motion.[189,196,228] In particular, superhydrophobic surfaces and SLIPS are designed to repel liquid droplets efficiently, minimizing adhesion and enhancing droplet mobility. According to the Cassie-Baxter model,[229] an increase in the roughness can increase the apparent contact angle by trapping air within surface asperities, reducing the liquid-solid contact area, and enhancing hydrophobicity. This effect promotes faster and more efficient droplet detachment, improving surface water repellency. This effect is particularly

advantageous for droplet-based energy harvesting systems, as any residual liquid can interfere with subsequent charge transfer, reducing overall efficiency.[215] Additionally, higher contact angles are often associated with improved contact electrification, aiding in the efficient capture of energy from rapidly moving droplets.[230]

To achieve optimal performance, surface roughness must be carefully engineered to balance the trade-offs between effective charge generation and droplet mobility.[187] Some nanostructured superhydrophobic surfaces (with increased roughness) have demonstrated higher electrical outputs, possibly because high-velocity droplet impacts collapsed the trapped air layer, increasing the contact area and enhancing the charge transfer.[189,231] However, at lower droplet impact speeds, the persistent air layer can reduce the effective contact area and limit the extent of electrification.[229] Thus, for practical applications, surface roughness should be carefully engineered to optimize triboelectric charge transfer while maintaining efficient solid-liquid interactions, ensuring stable and effective energy harvesting. The most common ways to increase the contact angle involve modifying the surface's morphology or adding texture layers, followed by coating with a low surface energy material such as fluoropolymers. This can be done through morphological changes like laser direct writing,[232,233] etching[220] and many other ways.

The femtosecond laser direct writing method is a highly effective technique for modifying surface roughness, enhancing both charge transfer efficiency and triboelectric performance in liquid-based TENGs. This process creates a porous micro/nanostructured layer on hydrophobic solid surfaces, significantly improving their hydrophobicity and surface charge density without altering the material's chemical composition. Zhang et al.[219] applied a line-by-line femtosecond laser scanning approach using a 1035 nm wavelength, 10 kHz pulse frequency, and 350 fs pulse width, with an optimal laser power of 1.07 W (Figure 10d). This treatment increased the water contact angle from 105° to 160°, preventing liquid residues and improving self-cleaning properties. More importantly, the modification played a crucial role in charge transfer dynamics by optimizing the contact area. While the superhydrophobic nature of the treated PTFE initially reduced droplet contact at low speeds, its porous microstructure expanded the effective contact area at high impact speeds, leading to greater charge induction. Additionally, the rapid spread and retraction of droplets on the modified surface further enhanced triboelectric output by accelerating charge transfer. Due to the

enhanced contact electrification, the open-circuit voltage and short-circuit current output increased by factors of 3 and 1.5, respectively.

Wang et al.[220] demonstrated the effectiveness of reactive ion etching in modifying FEP surfaces to achieve superhydrophobic properties (Figure 10e). Using reactive ion etching treatment in a plasma-therm chamber for 15 minutes, they created a highly water-repellent surface with a contact angle of 168.5°. The modification played a crucial role in droplet-based energy harvesting, significantly improving the anti-wetting behavior of the surface. One of the major advantages of this superhydrophobic FEP surface was its ability to prevent droplet coalescence, ensuring that each droplet detached instantly instead of forming a continuous liquid layer. This property was particularly beneficial under high-frequency droplet impacts exceeding 140 Hz, where maintaining individual droplet separation was essential for maximizing energy conversion. A direct comparison between the superhydrophobic surface-based droplet electricity generator (SHS-DEG) and a conventional droplet electricity generator (DEG) demonstrated a significant enhancement in output performance. Specifically, the average voltage output of SHS-DEG reached 14.63V, which was three times higher than that of DEG, while the average current output increased to 3.98 µA, which was twice that of DEG.

Unlike superhydrophobic surfaces, SLIPS-TENGs maintain stable electricity generation even in harsh environments due to their unique liquid-infused surface, which forms a smooth and continuous liquid-liquid interface. Xu et al.[221] in 2019 introduced a SLIPS-based TENG by incorporating a perfluorinated lubricant (PFPE) into a porous PTFE structure (**Error! Reference source not found.**f). They present SLIPS-TENG as a superior alternative to conventional superhydrophobic surface-TENGs (SHS-TENGs), addressing issues like surface wear, ice formation, and contamination. By integrating a lubricant-infused surface, SLIPS-TENG enhances mechanical durability, charge transfer efficiency, and environmental stability. A key discovery is the charge transparency phenomenon, where a critical lubricant layer thickness maintains charge transfer like solid-liquid interfaces, akin to wetting transparency in graphene. Unlike SHS-TENGs, which suffer from droplet bouncing and reduced charge efficiency, SLIPS-TENG ensures sustained droplet contact, leading to higher energy conversion rates. Its self-healing ability enables stable power generation even after surface damage. Additionally, it excels in extreme conditions, including low temperatures (-3 °C), high

humidity, and submerged environments, where SHS-TENGs typically fail. Experimental results show an order-of-magnitude improvement in energy harvesting, with SLIPS-TENG charging a 1 μF capacitor to 5V within 55 seconds at -3°C, demonstrating its efficiency in harsh environmental conditions.[221]

3.2.4. Bulk effect/ electrode design

The concept of the bulk effect and its structure optimizations in TENGs have been extensively reviewed by Xu et al.[215] The bulk effect, first introduced by Xu et al.[90] in 2020 (Figure 12a), marked a major breakthrough in liquid-solid TENG by significantly enhancing charge transfer efficiency in droplet-based electricity generators by placing an extra top electrode . Unlike conventional liquid-solid TENGs, which rely on interfacial charge transfer, the bulk effect facilitates directional and rapid charge transfer between electrodes, enabled by the integration of an additional aluminum electrode alongside the ITO layer. This closed-loop system allows efficient charge movement from ITO to aluminum during droplet spreading and a backflow of charge from aluminum to ITO during droplet retraction, leading to enhanced charge transport efficiency, improved charge retention, and significantly higher energy conversion efficiency.[90] Subsequent research has focused on optimizing this effect through structural modifications, resulting in two primary device configurations: the transistor-like design and the universal single-electrode design.
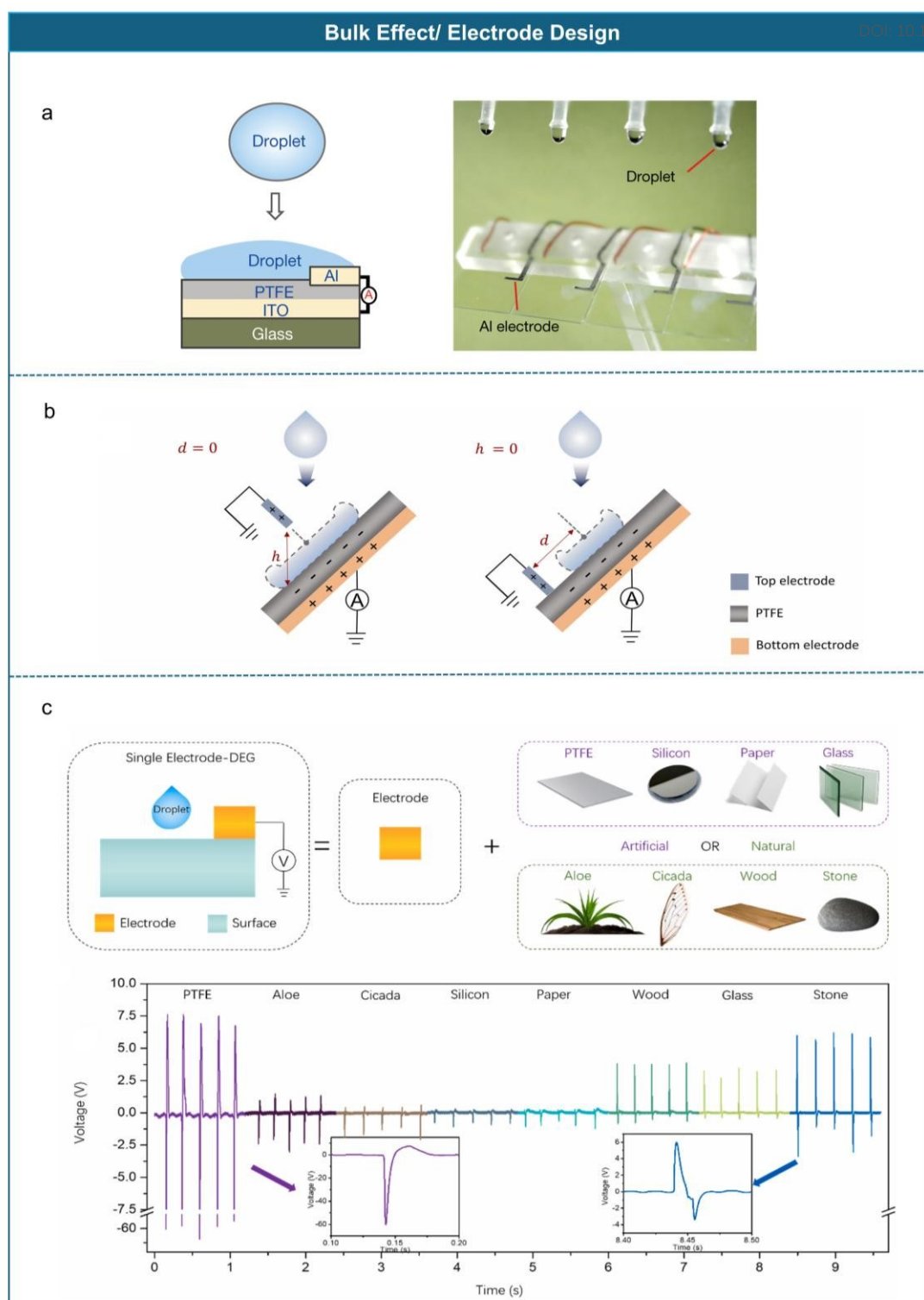
Lab on a Chip Accepted Manuscript

Figure 12. a) First bulk effect droplet-based electricity generator. Reproduced with permission.[90] Copyright 2020, Springer Nature. b) Transistor-Like Design for Droplet Energy Harvesting. Reproduced with permission.[234] Copyright 2023, Elsevier. and c) Universal Single-Electrode Configuration. Reproduced with permission.[235] Copyright 2021, Elsevier.

The transistor-like architecture, originally introduced by Xu et al.[90] revolutionizes the charge transfer process in liquid-solid TENGs by shifting from a

surface-dominated mechanism to a bulk-driven charge transfer process. This design consists of PTFE tribo-surface sandwiched between an ITO bottom electrode and an aluminum strip top electrode. Unlike conventional TENGs, where charge transfer is confined to the liquid-solid interface, this bulk-driven approach enables charge movement through the entire water droplet, significantly enhancing energy conversion efficiency. This setup allows the water droplet to act as a conductive bridge, simultaneously interacting with the PTFE surface, ITO electrode, and aluminum electrode, thereby increasing the effective charge separation and transfer (Figure 12a). As a result, this transistor-like droplet energy generator achieves an energy conversion efficiency of approximately 2.2%, which is several orders of magnitude higher than that of traditional single-electrode liquid-solid TENGs. Furthermore, this architecture facilitates an impressive charge transfer of 49.8 nC per 100 μL droplet, making it one of the most efficient designs for high-output energy harvesting in droplet-based TENGs.

Several optimization strategies have been proposed to enhance transistor-like droplet electricity generators. Wang et al.[236] found that incorporating a CYTOP intermediate layer between the tribo-surface and bottom electrode improves charge retention, with factors such as increased thickness, roughness, and surface charge injection all contributing to improved performance. Zhang et al.[234] investigated the effects of electrode positioning, demonstrating that placing the top electrode directly at the droplet's maximum spreading radius ($d = 0$) or at zero vertical distance ($h = 0$) from the tribo-surface shown in Figure 12b results in the strongest polarization and highest charge density. Extending the bulk effect beyond individual droplets, Zhang et al.[237] proposed a water-column-based energy harvester, in which a 10 cm water column slides through a tilted PTFE tube, achieving a record-breaking output of 904 V, 509 μA, and 118.1 mW at ~2 MΩ load. This approach highlights the scalability of bulk-effect-based energy harvesting beyond single droplet interactions.

Building upon the advancements in transistor-like architectures, the lubricant-armored transistor-like electricity generator[238] introduces a novel approach to bulk-effect-based energy harvesting by integrating a SLIPS with a transistor-like electrode configuration. This design incorporates a lubricated PTFE membrane, which forms a low-friction, transparent interface that enhances droplet movement during droplet impact. As a droplet contacts both the top and bottom electrodes, it momentarily establishes a closed-loop circuit, facilitating effective charge redistribution analogous

to a transistor gating mechanism. This architecture significantly improves energy conversion efficiency while ensuring robustness in challenging environmental conditions, such as high salinity, extreme pH variations, and fluctuating humidity. Under optimized conditions, featuring a 46 μm SLIPS layer thickness and a 0.1 M NaCl solution, the lubricant-armored transistor-like electricity generator has demonstrated an instantaneous power density of 118 W/m², a peak voltage of 65 V, and a current of 200 μA, outperforming conventional SLIPS-based TENGs.[238] Additionally, its scalable structure, developed on a printed circuit board (PCB) substrate, minimizes wiring complexity and enhances integration, making it well-suited for large-scale water energy harvesting applications.

To increase design flexibility, Zhang et al.[235] introduced the universal single-electrode liquid-solid TENG, which eliminates the bottom electrode, allowing any solid tribo-surface with a top electrode to function as an energy harvester (Figure 12c). Here, charge transfer occurs through the solid surface, droplet, top electrode, and ground, with water droplet movement serving as the switching mechanism for charge exchange. The output voltage V in this system follows the equation:

$$V \approx \frac{Q}{C} \qquad (29)$$

where Q represents the surface charge, and C is the EDL capacitance at the droplet–electrode interface. By eliminating interfacial charge screening, this configuration achieves a peak output of 62.2 V and 86.5 μA on PTFE, which represents 28 times and 1450 times improvement, respectively, compared to conventional single-electrode TENGs. Additionally, its feasibility has been demonstrated on natural surfaces such as aloe, wood, stone, and glass, confirming its adaptability for real-world applications.

A comparative study by Li et al.[239] analyzed the performance differences between universal single-electrode and transistor-like liquid-solid TENGs. Their findings indicate that universal single-electrode devices exhibit lower internal impedance, enabling them to operate efficiently with smaller optimal load resistances. Furthermore, an increase in water-to-ground capacitance extends the electrical relaxation time, leading to enhanced energy harvesting efficiency. This distinction highlights that while the transistor-like design excels in absolute power output, the universal single-electrode configuration provides greater adaptability and reduced impedance constraints.

While bulk-effect-based TENGs typically employ vertically stacked, transistor-like architectures to guide charge flow across dielectric interfaces, recent developments in coplanar electrode design present an alternative route for achieving high output through electrostatic interaction and droplet-bridging-triggered charge redistribution. In the droplet energy harvesting (DEH) panel developed by Xu et al.[240], both source and drain electrodes are positioned on the same substrate surface in a planar layout. The source electrode is fully encapsulated by a FEP dielectric, while the drain remains exposed (Figure 13a). When a water droplet lands on the FEP-covered source region, triboelectric charge separation occurs at the dielectric–droplet interface, generating a negative surface charge on the FEP and a corresponding positive charge on the droplet. As the droplet spreads to contact the adjacent drain electrode, it forms a transient conductive bridge that facilitates electron flow through the external circuit (Figure 13b). This electrostatic bridging event avoids vertical capacitive stacking and thus minimizes parasitic capacitance, resulting in faster circuit response and reduced energy loss.

Beyond its architectural elegance, the DEH panel demonstrates strong spatial adaptability and system-level efficiency. Xu et al.[240] designed two panel-topology strategies: a checkerboard electrode layout for structured droplet impacts, and a strip-like U-shaped drain configuration optimized for spatially random rain events. The A4-sized panel supports asynchronous, position-independent droplet activation, with each event triggering a localized output without signal interference. Instead of assigning a separate rectifier to each unit, all outputs are routed through a single full-wave bridge rectifier. This is possible because each droplet-induced current pulse lasts only a few milliseconds. Natural droplet impacts occur at low frequencies with minimal overlap, allowing the system to combine signals without interference or loss. The device achieves an average open-circuit voltage of 266.6 V and a short-circuit current of 273.6 µA. It is further shown to successfully power a wireless forest monitoring system including temperature and smoke sensors by charging a 10 mF capacitor to 10.69 V under natural rainfall.

While vertically stacked and coplanar TENG architectures, such as Xu et al.'s[240] droplet energy harvesting panel, have improved output via enhanced spatial charge collection and reduced parasitic losses, they still rely on AC output and require external rectifiers. As a further advancement in electrode configuration, Dong et al.[241] proposed a bioinspired total current nanogenerator (TCNG) that achieves DC output without

rectification, drawing design cues from the electrical discharge organs of rays. By embedding voltage-gated switching into the electrode system, the TCNG eliminates the need for external rectifiers and synchronization, offering a scalable solution for high-power DC output with simplified circuit design and easier integration into power conversion modules (PCMs).

The TCNG features a multi-channel structure consisting of eight charge-collecting needles (CCNs) positioned above a PTFE triboelectric surface (Figure 13c). Water droplets serve as charge carriers, generating triboelectric charges upon contact and transferring them to the CCNs and a shared bottom electrode. A gas discharge tube (GDT) connects the electrodes and functions as a voltage-controlled switch, initiating synchronized discharge once the accumulated potential exceeds ~600 V. This configuration enables asynchronous charge accumulation and timed energy release, producing stable, rectifier-free DC output.

The device operates through five stages: charge splitting, negative charge transfer, spatiotemporal charge separation, positive charge transfer, and charge neutralization. During this cycle, displacement current (I_d) builds up and is converted into conduction current (I_c) upon GDT activation, with the total output defined as $I_t = I_d + I_c$. The TCNG achieves an open-circuit voltage of 3000 V, a short-circuit current of 12 mA, and demonstrates practical capability by powering 1260 LEDs in a single discharge cycle.

More recently, Li et al.[242] advanced the TCNG architecture by introducing a fully integrated droplet-based nanogenerator system designed for real-world applications. Their platform combines a water-charge-shuttle design with a field effect–enhanced triboelectric interface, a DC–DC buck converter for power management, and physical compatibility with solar panels. This system reaches a record-high open-circuit voltage of 4200 V, powers 1440 LEDs, and supports smart greenhouse applications such as Bluetooth monitoring and thermohygrometer operation. These results demonstrate how total current based architectures can evolve from single-event demonstrations into scalable, field-deployable energy platforms, reaffirming the importance of electrode structure, charge routing, and system-level integration in next-generation liquid–solid TENG design.
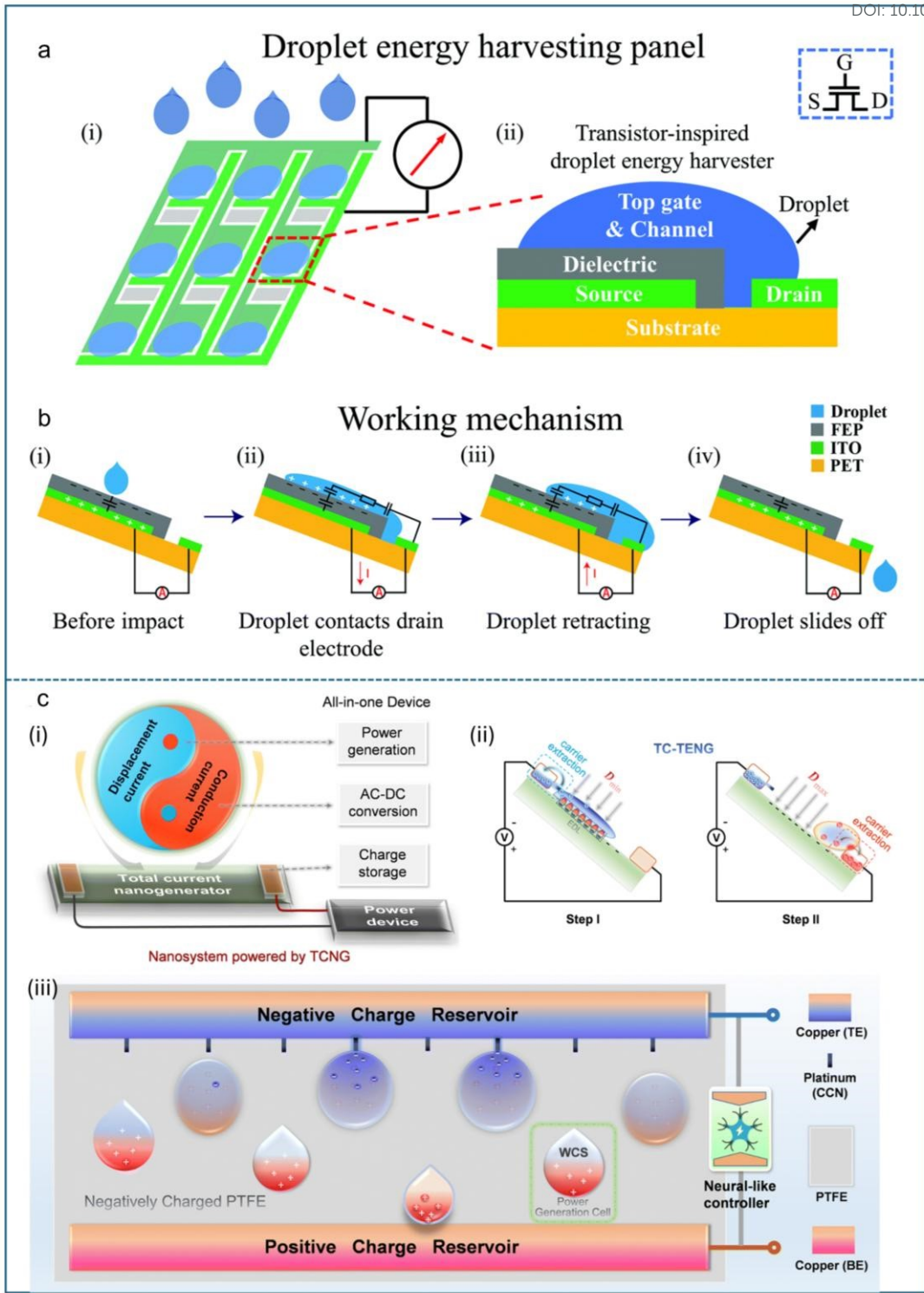
Figure 13. (a) Schematic of the droplet energy harvesting (DEH) panel and its transistor-inspired unit cell. Reproduced with permission.[240] Copyright 2022, Royal Society of Chemistry (b) Working mechanism illustrating charge transfer from source to drain upon droplet spreading, followed by charge recovery as the droplet retracts and exits. Reproduced with permission.[240] Copyright 2022, Royal Society of Chemistry (c) (i) Conceptual framework of TCNG systems integrating power generation and management. (ii) Representative charge induction steps in TC-TENG operation. (iii) Bioinspired TC-TENG design featuring dual charge reservoirs and neural-like

regulation. Reproduced with permission.[241] Copyright 2023, Royal Society of Chemistry.

3.2.5. Structure/hybrid structures

Enhancing the structural design of TENGs plays a critical role in improving their energy output and efficiency. Two primary strategies have emerged: (1) high-density configurations[215] that integrate multiple TENG units into an array[240] and (2) hybrid structures that combine TENGs with other energy harvesters to maximize energy extraction from various sources.[243]
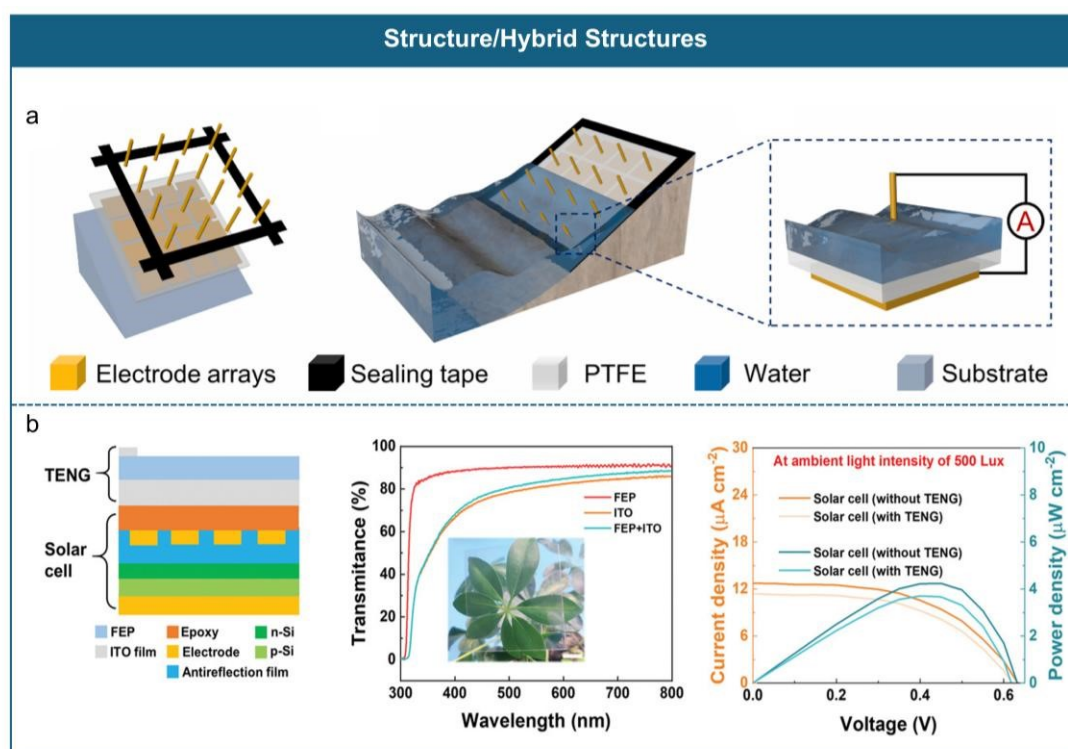

Figure 14. a) Wave Energy Harvester Utilizing a liquid-solid TENG Planar Array. Reproduced with permission.[244] Copyright 2021, Elsevier. b) Stacked Configuration of liquid-solid TENG and Solar Cell. Reproduced with permission.[245] Copyright 2023, Wiley-VCH GmbH.

The high-density design approach aims to increase the power density by arranging multiple liquid based TENG units in a structured array. This configuration ensures continuous charge transfer by enabling multiple points of contact. A recent advancement in this area was demonstrated by Gu et al.[244] who developed a wave energy harvester using 3D electrodes that interact with moving water (Figure 14a). The high-density electrode array increases the number of active liquid-solid TENG units per unit time by optimizing contact with the flowing liquid, leading to improved charge transfer and enhanced energy harvesting. This system achieved an instantaneous power

density of 11.7 W/m², demonstrating the effectiveness of structural innovations in boosting mechanical energy harvesting efficiency.

Another promising approach is hybrid integration, where liquid-solid TENGs are combined with complementary energy harvesting technologies, such as solar cells, piezoelectric nanogenerators, or electromagnetic generators. This synergy bridges the energy gap during periods when the liquid-solid TENG operates below the optimal conditions. For instance, Ye et al.[245] recently introduced a vertically stacked liquid-solid TENG and solar cell hybrid system, where a transparent liquid-solid TENG was placed above a solar cell. This configuration not only maintained light transmission but also boosted power density from 37.03 mW/m² to 40.80 mW/m² under simulated rainy conditions (Figure 14b). Such hybrid designs leverage multiple energy sources efficiently, ensuring a more stable and enhanced power output. Both high-density and hybrid structural designs continue to evolve, offering innovative pathways to enhance the practicality and efficiency of liquid-solid TENGs for real-world applications.
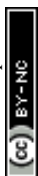
3.3. *Applications*

3.3.1. *Energy harvesting as power sources*

The range of TENG applications in liquid energy harvesting spans from small-scale droplet impacts to large-scale ocean waves. To clarify each system's application scope, we group the discussion into two categories: droplet electricity generators and bulk liquid (e.g., wave and pipe flow) based generators. This framework differentiates continuous flows like waves or pipe flow energy from discrete liquid interactions such as raindrops. It also highlights integrated autonomous setups and miniaturized designs for personal use.

3.3.1.1. *Droplet electricity generators*

Droplet electricity generators utilize the movement of liquid droplets to generate electricity through triboelectric charge transfer. As the droplet spreads or moves away, the charge equilibrium is disrupted, creating a potential difference between the electrode and the surface as explained in operational modes of TENGs (Figure c). Unlike conventional liquid-solid systems, droplet electricity generators can leverage both interfacial charge transfer and the bulk effect (Section 3.2.4) by incorporating additional electrodes and optimized liquid interfaces, leading to significantly higher power density.[90] Various advancements, including bioinspired surface engineering[158]

and functional material integration, have expanded the potential applications of these systems.

A notable example of droplet electricity TENG is the cactus-inspired droplet electricity generator,[158] which enhances droplet motion and charge transfer through an asymmetric amphiphilic surface. Inspired by cactus spines and Namib Desert beetle elytra, the system features an amphiphilic cellulose ester coating that provides hydrophilic sites for droplet nucleation from fog and hydrophobic regions for efficient removal (Figure 15a). A hydrophobic FEP channel guides the droplets smoothly toward the collection area. The spines are inclined at 60 degrees, optimizing Laplace pressure to drive droplets toward the hydrophobic channel. As droplets impact the droplet electricity TENG surface as shown in Figure 15a(ii), they generate triboelectric charges, leading to electrostatic adsorption. This process enables the TENG to generate an open-circuit voltage of 103.2 V, capable of lighting 400 commercial light emitting diodes (LEDs), while maintaining a surface charge of 42.6 nC after 770 droplets. By combining bioinspired structural engineering with triboelectric charge transfer, the system achieves a high water-harvesting efficiency of 93.18 kg/m²·h, making it one of the most effective triboelectric-enhanced water collection technologies.[158]

Another examples is the raindrop TENG developed by Xu et al.[159] for rainwater energy harvesting (Figure 15b). Using PCB technology, they fabricated a copper electrode array coated with a hydrophobic PTFE layer, ensuring smooth droplet rolling. Operating in single-electrode mode, this device harnesses charge transfer as droplets move across the PTFE surface, generating a potential difference that drives current through an external circuit. Under a rainfall intensity of 71 mm/min, this TENG exhibited an average short-circuit current of 15 µA, an open-circuit voltage of 1800 V, and a peak output power of 325 µW. Similarly, Ye et al.[245] developed a raindrop-TENG optimized for raindrop energy harvesting (Figure 15c). By layering a FEP film on an ITO electrode, they achieved efficient triboelectric charge transfer as raindrops rolled over the surface. To prevent signal disruption caused by excessive droplet impacts during heavy rainfall, they refined the array structure of the raindrop-TENG by optimizing electrode arrangement, spatiotemporal separation of raindrops and panel tilt angle to minimize charge cancellation and enhance energy output. This optimization resulted in a consistent average power density of up to 40.8 mW/m².

Expanding based upon droplet electricity triboelectric systems, liquid-liquid TENG has emerged as another promising alternative, leveraging liquid interfaces to enhance charge transfer and enable self-replenishing operation. Nie et al.[29] introduced a liquid-liquid TENG that utilizes precharged and grounded liquid membranes to harvest energy from falling water droplets. Unlike conventional liquid-solid TENGs, this system achieves energy conversion entirely at the liquid-liquid interface, offering unique advantages in permeability and self-healing capability. The permeability of the liquid membrane which let droplets pass through continuously ensures uninterrupted energy production. This sets it apart from conventional solid surfaces, which can trap leftover liquid and reduce charge collection efficiency. Moreover, the membrane's self-healing nature allows it to regain its structure after each droplet impact, enabling consistent operation. The design consists of two liquid membranes: a pre-charged liquid membrane and a grounded liquid membrane (Figure 15d). The pre-charged membrane accumulates positive charges induced by an adjacent negatively charged FEP film, which is pre-charged through triboelectric contact with a nylon film. The grounded membrane serves as a charge collector. When a neutral water droplet contacts the pre-charged membrane, the positive charges redistribute between the droplet and the membrane. As the droplet detaches, it removes a portion of the charge, disturbing the electrostatic balance. To restore equilibrium, charges are replenished from the ground to the liquid membrane, inducing a current flow and enabling continuous energy generation. This system demonstrated a peak power output of 137.4 nW for 40 μL droplets, making it highly effective for energy harvesting in rainwater collection, irrigation currents, microfluidic systems, and electrostatic charge removal from solid surfaces.

In another example, Zhang et al.[157] introduced a liquid-liquid TENG utilizing hydrofluoroether (HFE7500) fluid as a triboelectric material to efficiently charge rainwater droplets via electron transfer (Figure 15e). As droplets pass through HFE7500, electrons transfer from water to the fluid, progressively increasing the positive charge of the droplets. A ring-shaped electrode positioned around the droplet path generates a displacement current via electrostatic induction, ensuring efficient energy conversion. Due to the fluidity of the triboelectric layer, the contact surface is constantly refreshed, preventing charge saturation and maximizing energy output. The system achieves a charge density of 3.63 μC/L and sustains triboelectric charge exchange for up to 1200
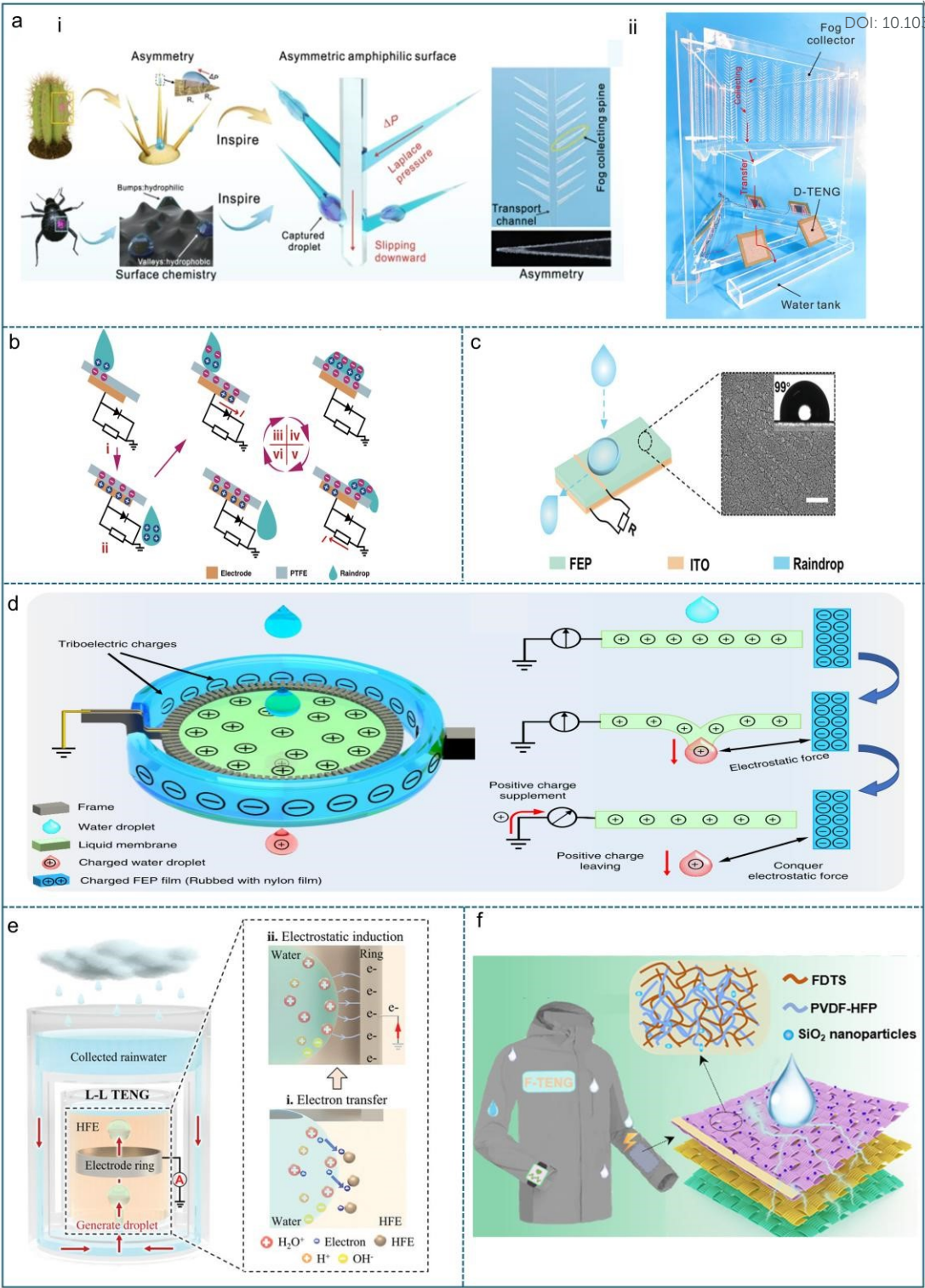
seconds before saturation. With a crest factor (evaluates stability of output signal) of approximately 1.1, the device exhibits stable output and is capable of generating DC, eliminating the need for rectifiers and reducing energy loss from switching components. Beyond rainwater energy harvesting, this approach is adaptable to microfluidic systems, hydropower applications, and self-powered environmental sensors, paving the way for scalable liquid-based energy solutions.

Advancements in material science have greatly enhanced the efficiency of droplet electricity TENGs. One such innovation is the all-fabric triboelectric nanogenerator, which incorporates a superhydrophobic surface made of SiO_2 nanoparticles, polyvinylidene fluoride-hexafluoropropylene (PVDF-HFP), and perfluorodecyltrichlorosilane (FDTS) coatings (Figure 15f). This multi-layered fabric structure provides high breathability, self-repairing hydrophobicity, and long-term durability. The device efficiently converts raindrop impacts into electrical energy through triboelectric charge transfer. Compared to conventional polymer-based triboelectric nanogenerators, the fabric TENG delivers stable performance even under prolonged environmental exposure, making it a promising solution for wearable electronics and outdoor energy harvesting applications.[246] Another example is the waterproof and fabric-based multifunctional TENG, which combines water-repellent ethylene-vinyl acetate friction layers with conductive and mesh fabric layers.[247]

Figure 15. Droplet electricity generator. a) Cactus inspired droplet electricity generator. Reproduced with permission.[158] Copyright 2022, Springer Nature. b) Raindrop energy-powered autonomous wireless hyetometer. Reproduced with permission.[159] Copyright 2022, Springer Nature. c) a hybrid solar panel with a TENG array for simultaneous raindrops and solar energy harvesting. Reproduced with permission.[245] Copyright 2023, Wiley-VCH GmbH. d) Rainwater energy captured using a combination of pre-charged and grounded liquid films. Reproduced with permission.[29] Copyright 2019, Springer Nature. e) Liquid-liquid TENG system for rainwater energy harvesting, utilizing HFE

for electron transfer and electrostatic induction for displacement current generation. Reproduced with permission.[157] Copyright 2022, Wiley-VCH GmbH. f) A self-repairing hydrophobic textile designed for efficient water droplet energy harvesting. Reproduced with permission.[247] Copyright 2019, Wiley-VCH GmbH.

3.3.1.2. Bulk liquid

Bulk liquid-based TENGs are designed to harness the ocean and pipe flow energy through frictional interactions between moving liquid masses and triboelectric layers. Ocean waves, water currents, and continuous flowing liquids provide a continuous and sustainable energy source, making bulk liquid TENGs a promising approach for energy harvesting. Various designs have been developed to optimize energy conversion efficiency, structural flexibility, and long-term durability. Different types of bulk liquid based TENGs have been extensively reviewed by Wang et al..[248] One notable design is the oblate spheroidal TENG (OS-TENG),[249] which extracts ocean energy through a steel tape coated with multiple dielectric triboelectric layers (Figure 16a). This study introduces a TENG network utilizing plane-like power cables composed of spring steel tapes and three polymer films. The steel tape functions as both the structural framework and an electrode, ensuring network stability while minimizing electrostatic interference from seawater ions. The outer porous PTFE film, which is highly hydrophobic, facilitates electricity generation through liquid-solid interface contact, working in conjunction with the steel tapes. The study systematically examines the power cable's working mechanism and output performance, reporting a maximum open-circuit voltage of 34 V and a transferred charge of 25 nC per cycle. The charge output can be enhanced by integrating multiple OS-TENG units. Similarly, another ocean-energy-based system is the dynamic electric double-layer TENG,[185] which captures wave-induced mechanical motion through an asymmetric array structure (Figure 16b). This system operates based on the formation and disruption of electric EDLs at the interface between water and the device's surfaces. In this setup, a polypropylene (PP) film serves as the positive dielectric layer, while a FEP film functions as the negative dielectric layer. When submerged, the water fills the gap between the films, leading to the formation of opposite EDLs that neutralize surface potentials and drive charge flow through external electrodes. As the water level fluctuates, the EDLs are periodically constructed and deconstructed, inducing the movement of free charges between the electrodes and generating an AC output. Under fluctuating water wave conditions, the device achieves a stable output current of 60.0

μA, an output voltage of 60.0 V, and an average power density of 5.38 W/m³. Its scalable design allows it to be implemented as an array, which has been successfully used to power signal spotlights, a digital thermometer, and a water quality detector, demonstrating its potential for real-world energy harvesting applications.[185]

Munirathinam et al.[250] introduced a liquid-metal-based TENG for energy harvesting from flowing water in pipes/channels. It features a Galinstan liquid-metal electrode encapsulated within a PDMS friction layer, utilizing a liquid-solid interface for triboelectric charge generation (Figure 16c). It generates electricity through contact electrification and electrostatic induction as flowing water interacts with the PDMS layer, creating an electrostatic potential difference that induces charge transfer in the Galinstan liquid-metal electrode. This Liquid-metal based TENG exhibits superior performance with a peak output of 6.2 V and 3.6 μA at a flow rate of 2.5 L/min, attributed to its flexibility and larger contact area. As water flows over the PDMS friction layer, the PDMS deforms and stretches, causing a reduction in its thickness due to the Poisson effect.[251] This decrease in thickness shortens the distance between the triboelectric charges in water and the Galinstan electrode, thereby increasing the electrostatic force acting on the electrode. Since electrostatic force is inversely proportional to the separation distance, a thinner PDMS layer enhances charge induction, leading to improved energy conversion efficiency. Additionally, the low Young's modulus of Galinstan allows it to stretch in response to PDMS deformation, further increasing the effective contact area between the electrode and the friction layer. This dynamic adaptation enhances triboelectric charge generation and charge transfer efficiency, leading to higher electrical output. Conversely, if the PDMS layer is too thick, the increased separation distance weakens the electrostatic attraction between the triboelectric charges and the electrode, thereby reducing the number of induced charges and lowering overall device performance. This design is highly effective for remote water flow monitoring in pipelines. In addition, it is also capable of powering LEDs and liquid crystal displays. Its ability to resist corrosion and prevention of electrode cracking ensures extended durability, even under low flow rates and continuous operation.

In another example, Deng et al.[184] developed a liquid-metal-based TENG optimized for low-frequency and multidirectional vibrations (Figure 16d). The fluidic nature of the liquid metal enhances its responsiveness to vibrations, maximizing energy
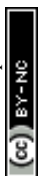
conversion. The device operates in freestanding mode, meaning the liquid metal is not fixed to any electrode but moves freely within a sealed chamber, functioning as an independent triboelectric layer. It generates electricity through contact electrification and electrostatic induction as the liquid metal moves freely within a sealed chamber, repeatedly making and breaking contact with the Kapton triboelectric layers due to external vibrations. This contact-separation motion induces charge transfer, creating an electrostatic potential difference, which drives electron flow through the external circuit, resulting in AC output. By combining freestanding movement with contact-separation charge generation, the device achieves a peak voltage of 252 V. It successfully charged a 10 μF capacitor to 6.46 V in 60 seconds at 7.5 Hz and demonstrated its capability by powering 100 LEDs during walking tests. With a power density of 33,000 mW/m³, the device is well-suited for applications in marine buoys and vehicle suspensions, offering an effective approach for vibration energy harvest.
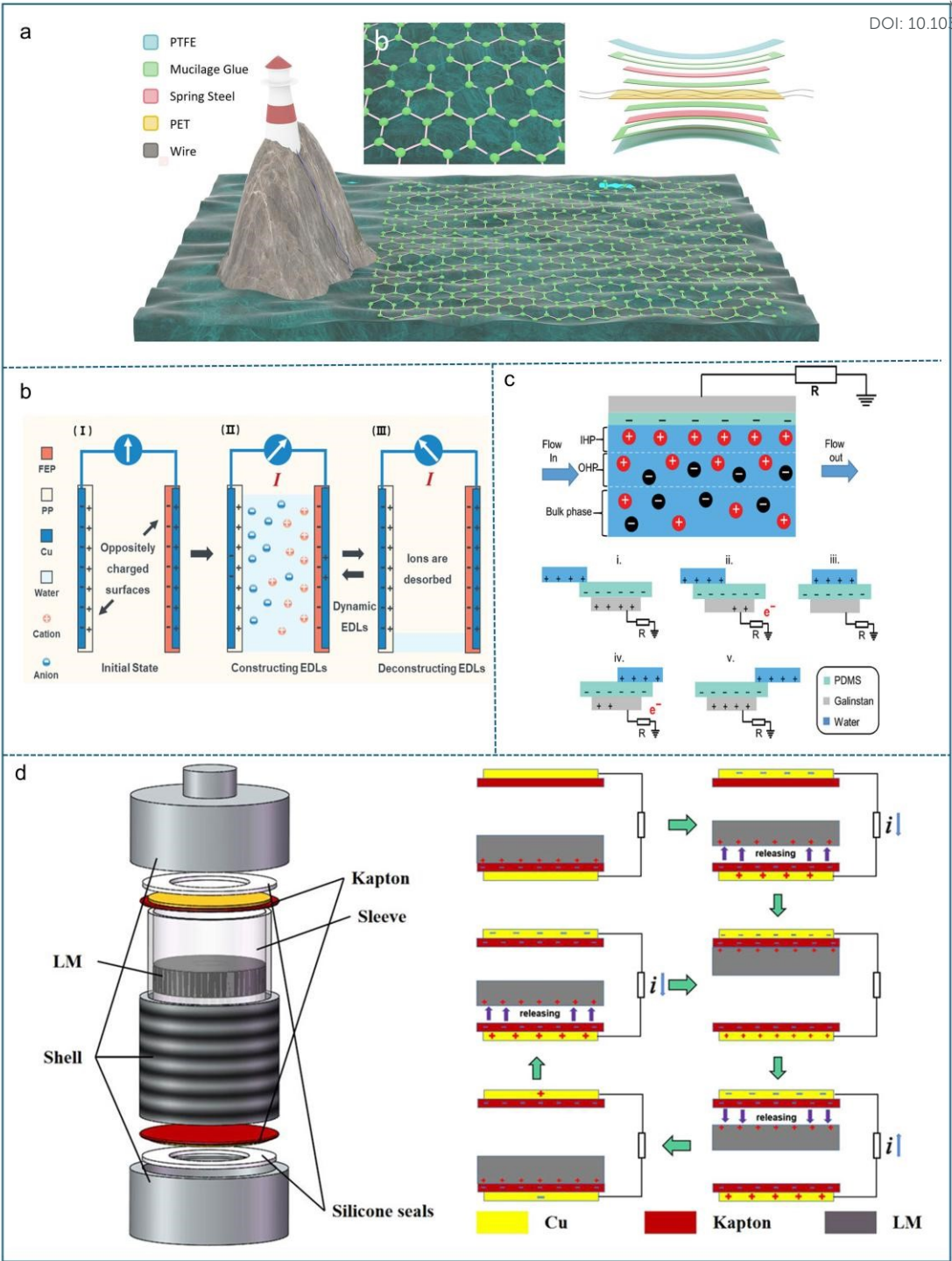
Figure 16. Bulk liquid based generator. a) Illustration of the OS-TENG structure and its potential for large-scale ocean wave energy harvesting. Reproduced with permission.[249] Copyright 2020, Elsevier. b) Asymmetric plate structure of the dielectric layer-based TENG. Reproduced with permission.[185] Copyright 2023, Wiley-VCH GmbH. c) Schematic of liquid metal-TENG harvesting energy through continuous water flow in and out. Reproduced with permission.[250] Copyright 2023, Wiley-VCH GmbH. d) Liquid-metal-based TENG optimized for low-frequency and multidirectional vibrations. Reproduced with permission.[184] Copyright 2021, Frontiers Media S.A.

3.3.2. *Self-powered sensors*

This section explores the advancements in liquid-based TENGs and their expanding role in sensing applications. It covers their fundamental working principles, mechanisms of charge generation, and integration into biomedical, environmental, and chemical monitoring systems. The discussion includes how these devices utilize liquid-solid and liquid-liquid interactions to generate measurable electrical signals, enabling real-time detection, analysis, and classification of various physical and chemical phenomena.

3.3.2.1. *Biomedical monitoring and sensing*

Solid–liquid TENGs are still in the early stages of medical application. A major innovation in this field is the bioresorbable triboelectric sensor (BTS)[252], designed to detect vascular occlusion events in real time inside the body. The BTS monitors pressure changes in blood vessels using a contact-separation mechanism that works in sync with the heart's systolic and diastolic phases. During systole, the blood vessel contracts, compressing the BTS and increasing voltage output. During diastole, the vessel relaxes, reducing the pressure and lowering the voltage output. These voltage fluctuations help in continuous monitoring of vascular blockages. Made from 4% poly(lactic acid)-chitosan (PLA/C), the BTS is attached to blood vessels, where it converts changes in blood flow due to occlusion into measurable electrical signals (Figure 17a). The sensor functions for about five days before it starts degrading and fully dissolves within 84 days, eliminating the need for surgical removal and minimizing health risks.[252]

A further medical-oriented design involves a tube-shaped liquid-solid TENG with a circular cross-section to monitor clinical drainage procedures.[186] This device employs a superhydrophobic SiNPs layer as the triboelectric surface and trimmed copper electrodes on the inner wall of a silicone rubber tube. By connecting the tube to a smaller-diameter drip line, pulsed current outputs are different for various liquids such as HCl, urine, blood, NaOH, and PBS demonstrate its potential for clinical IoT applications. As shown in Figure 17b(i), the triboelectric layer, along with trimmed copper electrodes, is positioned on the inner wall of a round silicone rubber tube. This tube is connected to a smaller-diameter silicone tube, which facilitates the flow of test liquids in droplet form through a tubular drop counter. When these droplets pass through the drop counter, they generate a pulsed current output, as depicted in Figure

17b(ii). The recorded current variations correspond to different liquid droplets, demonstrating the system's ability to differentiate between fluids. These findings highlight the potential of the fabricated droplet counter for clinical monitoring applications, as illustrated in Figure 17b(iii).[186]

Jiang et al.[156] introduced a dual-signal dopamine detection sensor utilizing a single-electrode solid-liquid TENG, composed of a PTFE film, copper electrode, and glass substrate. Dopamine detection is facilitated by its self-polymerization into polydopamine (PDA) on the PTFE surface which modifies surface charge properties and hydrophilicity, leading to distinct electrical responses. Two primary signals were generated: I_{TENG}, resulting from contact electrification and electrostatic induction at the oil–water–PTFE interface, and $I_{interface}$ arising from electrostatic effects within the oil–water interface (Figure 17c). Experimental findings demonstrated that contact angle measurements decreased with increasing PDA concentrations (0–500 μM L^{-1}), confirming effective surface modification. Furthermore, the dual-signal detection approach yielded detection limits of 5.15 μM for I_{TENG} and 3.96 μM for $I_{interface}$, establishing a sensitive and selective dopamine sensing platform.

A TENG-based nanosensor[253] (Figure 17d) was developed for high-throughput drug screening by detecting electrical signal variations caused by molecular interactions. This platform measures voltage changes when molecules bind to its surface, making it effective for identifying drug-protein interactions. Using FK506-binding protein (FKBP) rapamycin system as a model, the sensor successfully detected drug interactions with the autophagy-related cysteine protease ATG4B. It identified S130 and Tioconazole as inhibitors, while Dexamethasone exhibited no binding effect. To validate the findings, Kelvin probe force microscopy measured surface potential shifts, confirming how drugs alter the charge distribution on the sensor. Additionally, enzyme activity assays verified the inhibitory effects of certain compounds, ensuring precise drug screening. This self-powered platform provides a sensitive, reliable, and cost-effective solution for drug discovery.[253]
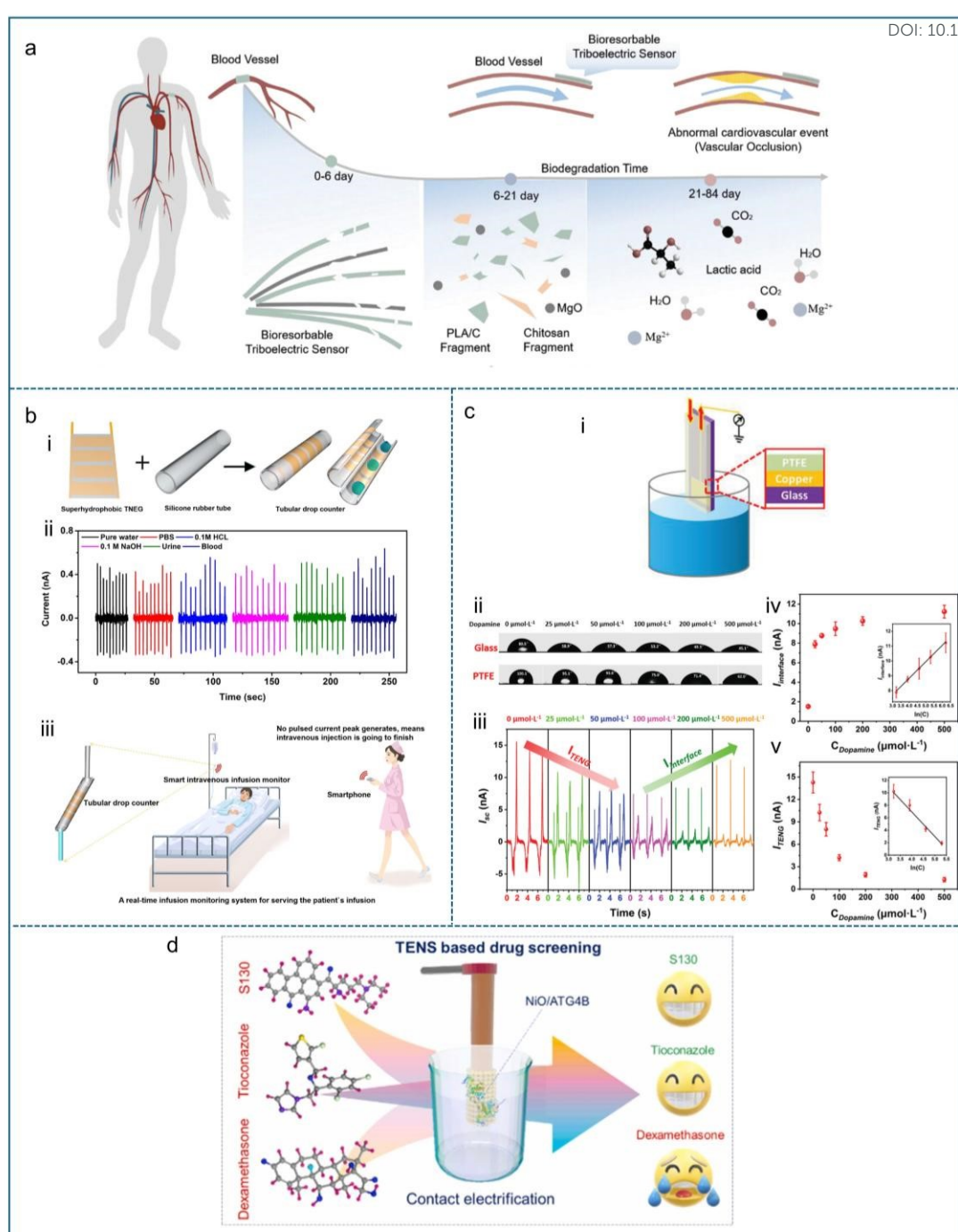
Figure 17. Biomedical monitoring and sensing. a) Liquid-solid TENG used for blood flow monitoring, designed to break down and be absorbed by the body over time. Reproduced with permission.[252] Copyright 2021, Wiley-VCH GmbH. b) a self-powered flow sensor for monitoring biofluids in healthcare system. Reproduced with permission.[186] Copyright 2020, American Chemical Society. c) a dual-signal self-powered device utilizing solid-liquid TENG for precise dopamine concentration detection. Reproduced with permission.[156] Copyright 2019, Wiley-VCH GmbH. d) triboelectric nanosensors for label-free screening of anti-tumor drugs. Reproduced with permission.[253] Copyright 2024, Elsevier.

3.3.2.2. Chemical sensing

TENGs have been widely employed for chemical sensing, including the detection of enzymes,[69] pesticides,[254] heavy metal ions,[154] and microplastic particles.[155] In one study, Huang et al.[155] developed a self-powered system integrating liquid-solid TENG with a deep learning model for detecting five microplastic types: polyethylene (PE), PP, polyvinyl chloride (PVC), PET, and polystyrene (PS). The liquid-solid TENG generates electrical signals through contact electrification and electrostatic induction when the FEP film interacts with water. As the device oscillates in the liquid, water droplets strike the FEP surface, initiating charge transfer. When pressure decreases, positive charges are transferred to the copper electrode, generating an electrical signal. The variations in voltage correspond to different microplastic types and concentrations, allowing for precise detection. Quantitative experiments in DI water at concentrations of 0.025%, 0.1%, 0.175%, and 0.25% demonstrated a direct correlation between microplastic content and voltage output (Figure 18a). A Convolutional neural network (CNN)-1D deep learning model was employed to classify the microplastic types, achieving an average recognition efficiency of 86.7%, with 100% accuracy for PS and 82% for PET.

Chatterjee et al.[255] developed a triboelectric nanosensor based on liquid-solid contact electrification for catechin detection, while also optimizing liquid-solid TENG performance (Figure 18b). The sensor uses TiO_2 nanosheet arrays as the solid triboelectric material, with water, ethanol, and acetone serving as the liquid contact mediums. Catechin molecules interact with the TiO_2 surface, forming a ligand-to-metal charge transfer complex, which alters surface charge density and improves electron transfer efficiency. This interaction leads to a measurable increase in voltage, reaching 1.2 V at 80 μM catechin concentration. Ultraviolet photoelectron spectroscopy analysis confirmed that catechin adsorption reduced the TiO_2 work function from 6.54 eV to 5.52 eV, indicating improved charge transfer.

Similarly, Gao et al.[254] developed a TENG-based self-powered urea sensor with high sensitivity and specificity by incorporating enzyme-catalyzed reactions into a dual-electrode configuration. The sensing mechanism relies on the hydrolysis of urea by urease, which alters the pH of the solution. This pH change influences the triboelectric charge transfer between the PDMS surface and the liquid, modifying the electrical output of the TENG. The device effectively detects urea concentrations as low as 4 μM and remains unaffected by common fertilizer ions. High-performance

liquid chromatography validation confirmed a strong correlation between output voltage and urea concentration, demonstrating its applicability in agricultural.

Chen et al.[256] further expanded TENG sensing to microfluidics, creating a capillary-tube triboelectric nanogenerator (ct-TENG) for non-destructive microliter sampling (0.5 μL) (Figure 18c). By harnessing Maxwell's displacement current from liquid flow, electrical outputs indicated variations in total aerobic count (TAC) in barreled water. The ct-TENG senses TAC by detecting changes in its electrical signals (voltage, current, charge transfer) as microbial growth increases. Bacteria release charged byproducts that weaken the triboelectric effect, causing a progressive decline in output signals. Over time, increased TAC led to decreased current, voltage, and charge transfer signals, enabling determination of optimal drinking intervals before water quality deteriorated.
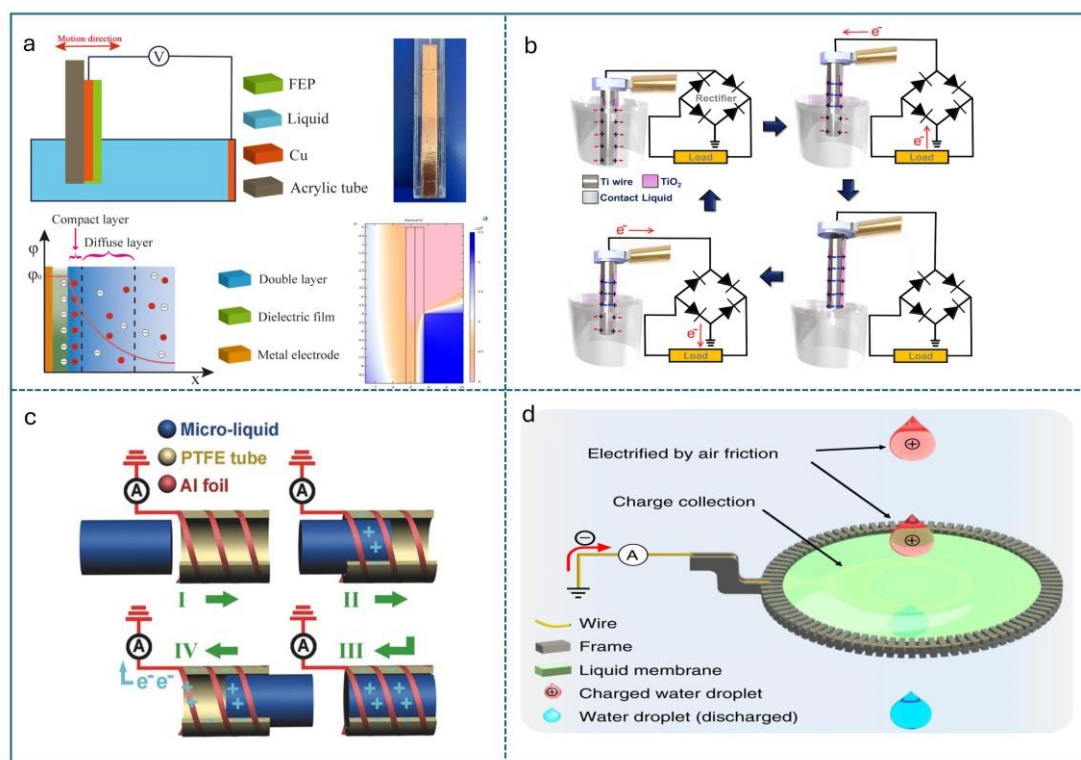

Figure 18. Applications of Liquid-Based TENGs in Sensors. a) Detection and classification of microplastics using deep learning integrated with liquid-based TENG technology. Reproduced with permission.[155] Copyright 2023, American Chemical Society. b) Working mechanism of TiO2-based liquid-solid Triboelectric nano-sensor for catechin detection. Reproduced with permission.[255] Copyright 2020, Elsevier. c) Working mechanism of capillary-tube triboelectric nanogenerator. Reproduced with permission.[256] Copyright 2018, Wiley-VCH GmbH. d) Rainfall sensing: establishing an approximately linear relationship between rainfall intensity and the device's electrical output. Reproduced with permission.[29] Copyright 2019, Springer Nature.

3.3.2.3. Environmental and other sensing

Beyond chemical and biomedical uses, liquid based TENGs have proven effective in environmental monitoring. Nie et al.[29] and Zhang et al.[257] both developed liquid-liquid TENG that can harvest energy from rainwater and also serve as rainfall sensors. In their work, they established a quantitative relationship between the TENG's electrical output and the intensity (or amount) of rainfall. As rainfall intensity (rate of precipitation per unit area) increases, the measured triboelectric signals (voltage or current) correlate with the number or volume of raindrops hitting the device. Specifically, Nie et al.[29] investigated the voltage and short-circuit current generated when droplets of different volumes flowed through a liquid film, observing a nearly linear increase in both voltage and current as droplet volume rose (Figure 18d). This approach mimics varying rainfall intensities by changing the droplet size. Similarly, Zhang et al.[257] showed a linear relationship between open-circuit voltage and actual rainfall amounts. Using this correlation, they designed a rainfall alarm system that monitors and flags certain rainfall levels based on the TENG's output voltage. Essentially, higher rainfall intensity leads to a greater triboelectric output, enabling real-time measurement and warning if thresholds are exceeded.

In the maritime domain, Wang et al.[68] designed a ring-shaped TENG for ship tilt angle detection. The device consists of a PTFE ring tube with an external copper electrode; an internal liquid layer moves as the ship tilts, leading to contact electrification and generating electrical signals open-circuit voltage, short-circuit current, and transferred charge correlate with the tilt-induced arc length of fluid displacement. An integrated LED provides real-time feedback, while an alarm system warns the crew if the tilt angle surpasses a critical threshold, ensuring timely evacuation measures.

3.4. Challenges and opportunities

Liquid based TENGs show significant promises for both energy harvesting and self-powered sensors, yet critical challenges persist regarding long-term stability, environmental adaptability, and methods to continuously boost energy output. Moreover, most TENGs currently generate only microwatts of power, which is sufficient for certain microsensors but inadequate for powering larger devices. This limitation underscores the need to enhance energy conversion efficiency to achieve continuous and higher power outputs.[197]

Durability remains a critical challenge for liquid based TENGs, as factors like electrode corrosion, material wear, contamination, and wetting[258] can degrade performance over time. Mechanical deformation and abrasion can lead to electrode delamination and tribo-surface degradation, particularly in wearable and portable applications. Strategies to enhance durability include material engineering for stronger tribo-surfaces, hydrophobic modifications to prevent wetting and contamination, and corrosion-resistant electrode designs.[259,260] Additionally, SLIPS have emerged as an effective solution, offering self-healing properties, anti-icing capabilities, and stable performance under extreme environmental conditions.[221,261] These approaches are essential for improving the longevity and reliability of liquid based TENGs in real-world applications

Environmental conditions play a crucial role in the performance of liquid based TENGs and should be carefully considered. Temperature is a key factor where liquid based TENGs exhibit a decline in electrical output as temperature increases.[209,262] This reduction occurs because higher temperatures accelerate electron dissipation into the environment, following the principles of thermal emission theory. Light is another influential factor, typically enhancing TENG performance.[263] Exposure to photons increases the concentration of electron-hole pairs, boosting charge generation.[264] The extent of this enhancement depends on wavelength and light intensity. The shorter wavelengths and higher light intensity lead to greater output performance since they produce higher luminous flux, resulting in more electron-hole pair generation at the triboelectric interface.

Researchers have explored various strategies and advancements aimed at enhancing TENG performance and facilitating its industrialization. In Section 3.2, we discussed in detail the methods to improve the performance of TENGs including increase surface charges, facilitating interface charge transfer and enhancing liquid motion. Additionally, the bulk effect phenomenon, where an additional top electrode is incorporated to improve charge transfer efficiency, was examined. To further boost TENG output, high-density designs have been explored, where multiple arrays of TENGs are connected to amplify overall energy generation. Moreover, integrating TENGs into hybrid systems, such as solar or wind energy harvesters, can further optimize performance and expand practical applications. Another promising approach involves hybrid TENG designs that combine TENGs with electromagnetic generators

or other energy-harvesting methods. These hybrid configurations help broaden frequency response and improve overall power output. However, the complexity and high volume of such hybrid systems remain challenges, limiting their practicality. To address this, advancements in compact circuit designs and refined power management strategies are essential for maximizing overall system efficiency. While significant progress has been made in TENG technology, further innovations and optimizations are required to achieve large-scale commercialization. Continued research into materials, design scalability, and energy storage integration will be key to bridging the gap between lab-scale prototypes and real-world applications.

As the liquid based TENGs developed over time, production costs will decline, miniaturization will improve, and the scope of applications ranging from everyday water usage to wearable devices will continue to grow. With further exploration into sustainable materials, advanced structural designs, and robust circuit integration, liquid based TENGs are poised to play a central role in future energy solutions, promising both reliability and scalable power generation in practical settings.

4. Electrokinetic energy conversion (EKEC)

4.1. Basic working principle

Electrokinetic energy harvesting, as a promising renewable energy conversion technique,[265] is suitable for both small- and large-scale applications.[266–269] Electrokinetic was first studied by Helmholtz[70] in 1879, providing the foundation for subsequent theories on energy conversion working principle. The EKEC utilizes ion movement in a liquid interacting with a charged surface, where an EDL forms. When the liquid moves over the charged surface, it induces the movement of counterions in the EDL, creating a difference in potential that can be utilized as electrical energy.[270–273]

Water in nature exists in diverse forms, from bulk liquid (e.g., flowing streams and ocean waves) to droplets and vapor. The electrokinetic mechanisms can harvest energy stored in different forms of water. Compared with liquid-based TENG, which were discussed in the previous sections, EKEC systems represent a fundamentally different energy conversion mechanism. Although both rely on interactions between liquid and solid surfaces and are enhanced by fluid motion, their working principle diverge significantly. Liquid-based TENG generates electricity through contact

electrification and electrostatic induction. The surface charges are exchanged when a liquid contacts and separates from a dielectric surface, leading to transient current pulses. In contrast, EKEC exploits EDL formed at charged solid-liquid interfaces. As the liquid moves along the surface, it induces the transport of counterions in the EDL, producing an electrical output. Furthermore, the output from liquid-based TENG is typically AC due to its periodic contact-based operation, whereas EKEC can produce either AC or DC, depending on the specific flow. A more comprehensive comparison of these two technologies is provided in Table 2. To systematically explain how EKEC works for various forms of liquids, this section categorizes them into three main approaches: drawing potential, waving potential, and streaming potential.

4.1.1. Drawing potential

When an external force causes the relative motion of the liquid electrolyte droplet on conductive solid surfaces (e.g., graphene-based materials, conductive metals, MXenes, highly doped semiconductors, etc.), the counterions in EDL are adsorbed at the front edge and desorbed at the rear edge of droplet (Figure 19a). The counterions drawn electrons from substrate around the front edge region, resulting in potential difference comparing to the rear edge region. Yin et al.[274] first demonstrated in 2014 that electrical energy can be generated by sliding a NaCl solution droplet on a monolayer of graphene plane, which they termed as "drawing potential". Specifically, when the electrolyte droplet comes to rest on the graphene sheet, the ions distribute symmetrically on both sides of the droplets, and there is no potential difference between the front and rear edges. A thin electron accumulation layer forms on the graphene's surface, creating a pseudocapacitor with the cation layer. Once the droplet slides on the graphene surface, the cations are adsorbed on the front edge. The capacitance at the droplet front and rear edges can be considered as C_F and C_R, respectively (Figure 19d).[274] The advancing movement of droplet drives the C_F moving forward and draws electrons from the substrate, causing C_F charging. Simultaneously, the cations desorbed at the rear edge of the droplet result in C_R discharges, releasing electrons back into graphene. Compared to static conditions, the entire process results in an increase/decrease of electron density at the rear/front edge of a moving droplet. The charging of C_F and simultaneous discharging of C_R drive free electrons to move across through the solid substrate beneath the droplet from rear to front edge. When the droplet

moves along the surface with velocity v, the rate of change of the pseudo-capacitances at the front and rear can be calculated as:

$$\frac{dC_F}{dt} = -\frac{dC_R}{dt} = C_0 W v \tag{30}$$

where W is the width of the solid substrate under the droplet, and C_0 is the pseudo-capacitance per unit area of the solid substrate, v is the velocity of the moving droplet. The equivalent current can be determined based on the rate of electron transfer:

$$I = -\frac{dq_e}{dt} = \psi\frac{dC_F}{dt} = -\psi\frac{dC_R}{dt} = -\psi W C_0 v \tag{31}$$

where $\frac{dq_e}{dt}$ is the rate of transferred electrons, ψ is defined as the equivalent surface potential of the solid surface relative to the absorbed cation layer. The induced open-circuit voltage can be expressed as:

$$V = -l R_{sq} \psi C_0 v \tag{32}$$

where R_{sq} is the square resistance of the solid surface and l is the length of the droplet.

4.1.2. Waving potential

While electrolytes wave on conductive solid surfaces (e.g., graphene-based materials, conductive metals and oxides, highly doped semiconductors, etc.), an EDL boundary forms near the gas-liquid interface.[275] The moving EDL boundary on the surface converts mechanical energy from waving motion into electrical energy. In 2014, Yin et al.[83] first discovered that when a graphene sheet was inserted into an ionic solution or the liquid-air boundary moved along the graphene sheet, voltage signals could be generated (Figure 19b). They termed this phenomenon as waving potential. While the graphene sheet is partially immersed in NaCl solution, the EDL boundary forms near the gas-liquid interface on the graphene surface. Due to the graphene sheet having stronger adsorption to Na^+, more Na^+ will be adsorbed near the moving boundary of EDL than Cl^-. Their analysis of charge transfer showed that the graphene becomes hole doped by the EDL. The doping effect becomes stronger when graphene only adsorbed a layer of Na^+. As the graphene inserts into the solution, at the moving EDL boundary, the formation of diffuse layer lags behind of firmly adsorbed Na^+ layer. As a result, the charge of the Na^+ layer near the EDL boundary is not immediately screened by Cl^-. Therefore, excess electrons are absorbed from submerged sections of graphene, leading to higher hole concentration and electric potential in this region. The

higher local electric potential on graphene sheet drives a hole current from the liquid-air boundary toward the deeper region of graphene submerged in the solution. As a result, the potential difference is generated between two ends of the graphene sheet. Similarly, when the graphene sheet is withdrawn from the ionic solution, the EDL boundary shifts downward, reversing the hole current (Figure 19b). This movable EDL boundary can be modeled as a series of evenly spaced parallel capacitors ($c_1 - c_n$), where the solid substrate absorbing cations serves as the positive electrode, and the anions diffuse layer acts as the negative electrode (Figure 19e).[275] When the solid substrate is immersed in the solution, the capacitor c_n near the boundary of the moving EDL accumulates more charges and exhibits a higher potential compared to the rest of capacitors located lower in the solution ($c_1 - c_{n-1}$). As a result, c_n discharges its charge uniformly to c_1 through c_{n-1} via a local current I, expressed as:

$$I = q_0 W v \tag{33}$$

where q_0 is the discharging charges per unit area of c_n, W is the width of the solid substrate. The average current through each resistor can be expressed as: $i_m = \frac{m}{n} q_0 W v$, ($m = 1,2,3,...,n$), where m represents the position index of the resistor, and n is the total number of capacitors. The voltage across the graphene sheet can be expressed as:

$$V = \frac{1}{2} R_{sq} q_0 v d \tag{34}$$

where R_{sq} is the square resistance of solid substrate, d is the inserted depth of the solid surface. When the entire substrate is immersed in the solution, the distance d reaches its maximum value d_{max}, which corresponds to the length of the substrate between the two end electrodes. Under this condition, the peak voltage is expressed as: $V_{peak} = \frac{1}{2} R_{sq} q_0 v d_{max}$. Therefore, the V_{peak} increases with higher inserting speed.

4.1.3. Streaming current/potential

Due to the development of micro/nanofluidic techniques and material science, many experiments can be performed with micro/nanochannels and porous materials.[276,277] When the electrolyte flows over solid or immiscible liquid surfaces driven by pressure gradient, the counterions in the diffuse layer of EDL move along with the fluid, producing a streaming current.[278] If there are reservoirs at the ends of the

micro/nanochannels, the accumulation of counterions in the downstream reservoir induced ion concentration imbalance between the two ends of the channel, thereby generating a potential difference between the two reservoirs. In open-circuit measurement, the potential difference is known as the streaming potential (Figure 19c).[279] With the assumption of negligible surface conductance, thin EDL (channel height is much larger than Debye length), and Debye-Huckel limit (low $\frac{e\zeta}{\sigma T}$),[18] the streaming potential, V_s, and streaming current, I_s, can be defined with equations:[280]

$$V_s = \frac{\varepsilon \varepsilon_0 \zeta}{\eta \sigma} \Delta P \tag{35}$$

$$I_s = \frac{\varepsilon \varepsilon_0 \zeta}{\eta} \frac{\Delta P}{L} A \tag{36}$$

where ζ is zeta potential of the surface, η is dynamic viscosity of the electrolyte, σ is specific conductivity of the electrolyte, ΔP is pressure difference, L and A are channel length and cross section area, respectively (Figure 19f).

The EKEC efficiency is an important metric to quantify the performance of streaming potential systems. It is defined as the ratio of the harvested electrical power to the mechanical power input required to drive the flow. The EKEC efficiency η_{eff} can be mathematically expressed as:[60]

$$\eta_{eff} = \frac{P_{output}}{P_{input}} = \frac{I_s \cdot V_s}{\Delta P \cdot Q} \tag{37}$$

where Q is the volumetric flow rate of the electrolyte. This efficiency reflects how effectively pressure-driven fluid is converted into electrical energy through electrokinetic effects. In practical systems, this efficiency is typically low due to viscous dissipation and Joule heating, but it can be improved through surface engineering and optimization of fluid and system properties.
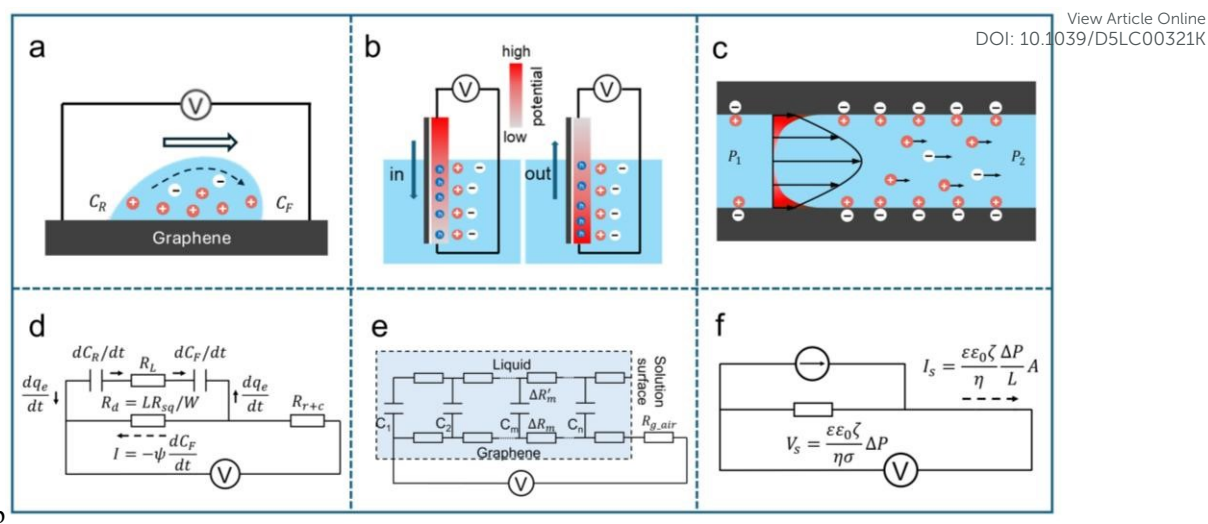
Figure 19. Basic working principles of electrokinetic energy conversion. a) Schematic illustration of pseudocapacitance formed at front and rear edge of moving droplet inducing the potential difference. b) Schematic of adsorption (left) and desorption (right) of ions on the graphene surface forming EDL and its boundaries, during insertion and withdrawal processes. The illustration also depicts the induced potential difference and the hole concentration gradient within the graphene sheet. c) Schematic of electrokinetic streaming current/potential generated through pressure driven electrolyte flow within micro/nano channels. The positive and negative charges are indicated with red and white circles. d) Equivalent circuit of drawing potential. e) Equivalent circuit of waving potential. f) Equivalent circuit for streaming potential.

4.2. Strategies to improve electrical output

Building upon the fundamental mechanism of electrokinetic energy conversion, enhancing electrical output requires strategic modifications at the solid-liquid or liquid-liquid interface as well as optimization of system structures. These improvements can be broadly categorized into three key aspects: (1) enhancing the interfacial zeta potential to increase electrokinetic efficiency, (2) promoting interfacial fluid slip to enhance ion transport, and (3) reducing channel dimensions to induce overlapped EDL, thereby enhancing counterions transportation in channels. The following sections will discuss these strategies in detail, emphasizing how surface engineering, structural design, and liquid-phase modifications can collectively contribute to improving electrokinetic performance.

4.2.1. Enhance interfacial zeta potential

Increasing the interfacial zeta potential is a widely recognized and effective strategy to enhance electrokinetic electrical output. The zeta potential, ζ, is the electric potential at the shear plane where hydrodynamic motion becomes possible.[280] For drawing potential, as shown in Eqs. 31 and 32, the output current is affected by

equivalent surface potential, ψ, which is the electric potential at the surface and can be equivalent to zeta potential in electrokinetics. Similarly, C_0 is the EDL capacitance and can be approximated as $C_0 \approx \varepsilon/\lambda_D$. For waving potential, the output current is influenced by discharged charge per unit area, q_0, during surface perturbation. The q_0 is set by the interfacial charge storage, which can be approximated as: $q_0 \approx C_0\zeta$. According to Eqs. 35 and 36, the streaming current and potential are directly proportional to ζ. A general expression of streaming current induced by flow velocity profile is: $I_s = \int_A \rho_e \boldsymbol{u} \cdot dA$ where ρ_e is electric charge density and $\boldsymbol{u}$ is velocity field vector. In the streaming potential mechanism, the EDL near the solid surface can be modeled as a parallel-plate capacitor, where the diffuse layer stores mobile counterions whose movement under flow contributes to current generation. Therefore, the electrokinetic output current density of drawing, waving and streaming modes can be generalized into a compact expression: $I_{output} \propto C_0\zeta u$. This generalized relation captures the shared physical principle of fluid-induced charge displacement governed by interfacial electrostatics. The zeta potential at the interface is influenced by multiple factors, including the surface properties of the solid material and the electrolyte parameters.

One direct strategy for increasing zeta potential is to enhance the intrinsic surface charge density. Metal oxides and their derivatives are well known for carrying substantial surface charges in aqueous suspensions.[281] Due to their high zeta potential, metal-based nanomaterials (e.g., nanoparticles and nanowires) are highly suitable for EKEC applications. For example, Al_2O_3 nanoparticles with a zeta potential of 40.3 mV have been incorporated into hydrophilic PET membranes, yielding a sustained voltage of 2.5 V and a current of 0.8 mA.[282] The output voltage from other metal oxides materials, such as Fe_2O_3, Mn_3O_4, TiO_2, showed positive correlation with the strength of their zeta potential.[282]

Furthermore, specific functional groups on solid surfaces, such as hydroxyl (-OH), carbonyl (-CO), and carboxyl (-COOH) groups, ionize in solution, imparting a negative charge to the solid surface and further enhancing the zeta potential,[283] thereby improving energy conversion efficiency (Figure 20a). For example, Li et al.[284] functionalized carbon nanoparticles with poly (sodium-p-styrene sulfonate) (PSS), 1,2,3,4-butanetetracarboxylic acid (BTCA), polyethyleneimine (PEI), and poly(diallyl dimethylammonium chloride) (PDADMAC). The corresponding zeta potentials of the

modified carbon nanoparticles shifted from the initial -30 mV to -58 mV, -35 mV, 20 mV, and 56 mV, respectively. Consequently, as shown in Figure 20b, the resulting streaming potential increased from 1.2 V to 3.0 V, 2.8 V, -2.5 V, and -1.5 V, respectively.

Besides optimizing solid material properties, the ionic properties (e.g., ion species, and ion concentration) of the electrolyte significantly influence the streaming potential/current in EKEC. Ion species also play a crucial role in electrokinetic phenomena,[285] influencing ion adsorption, hydration, and mobility at the solid-liquid or liquid-liquid interfaces. Zhang et al.[286] experimentally measured the streaming potential of LiCl, NaCl, and KCl solutions flowing through ion exchange membranes with the same ion concentration to determine the influence of ion species contributing to zeta potential. The zeta potential decreased in the order of $Li^+ > Na^+ > K^+$, which attributed to variations in ionic mobility.[287] Also, Yin et al.[274] experimentally measured the drawing and waving potential generated by LiCl, NaCl, KCl, NaF, NaCl, NaBr, and NaI solutions. As shown in Figure 20c, with a consistent 0.6 M concentration, the higher output voltage was generated with smaller ionic radius for both cations ($Li^+ > Na^+ > K^+$) and anions ($F^- > Cl^- > Br^-$). In addition, the higher valency of ions also enhances the zeta potential. Lobbus et al.[288] experimentally investigated the influence of mono-, di-, and trivalent counterions on zeta potential. The results indicated that electrolyte with trivalent counterions exhibit much larger zeta potential than electrolyte with di- and monovalent counterions.

In addition to ion size, higher electrolyte concentration can significantly reduce electrokinetic energy conversion efficiency. With higher ion concentrations in the electrolyte, higher fraction of the excess charge ions are in the Stern layer,[289] result in reducing the thickness of EDL and zeta potential on the solid surface.[290] By fitting various of experiment results,[291–294] the relationship between ζ and ion concentration, c, can be approximate as: $\zeta \sim -\log c$ for low ion concentration range (<1 M).[280,295] Kirby et al.[280] summarized that the zeta potential yields to linear relationship with pC ($-\log c = pC$) while different aqueous solution in contact with solid substrate.

4.2.2. Promoting interfacial fluid slip

At the no-slip boundary condition, the fluid velocity reduced to zero at the liquid-solid interfaces where counterions accumulate most densely.[296] Thus, the no-slip boundary condition will limit ion transport close to solid surfaces.[297] If fluid slip

presents at the solid-liquid or liquid-liquid interface, based on the Navier slip boundary condition, the fluid slip velocity at the slipping interface, u_{slip}, can be expressed as: $u_{slip} = b\frac{\partial u}{\partial y}|_w$, where b is the slip length, the extended length below the interfacial plane where fluid velocity reduces to zero as shown in Figure 20d, $\frac{\partial u}{\partial y}|_w$ is the shear rate at the wall. In the Debye-Huckel limit, the local charge density in the EDL decays exponentially as $\rho_e(y) = \rho_0 e^{-y/\lambda_D}$, where ρ_0 is the charge density at the wall.

To quantify the effect of slip on electrokinetic energy conversion, the Stokes equation can be solved under the Navier boundary condition. This yields a velocity profile: $u(y) = \frac{1}{2\eta}\frac{dp}{dx}(y^2 + (2b - H)y + 2b^2 - Hb)$, where H is the channel height. By substituting velocity and local charge density profile in streaming current equation, $I_s = \int_0^H \rho_e(y)u(y)dy$, the streaming current under Navier slip boundary condition yields: $I_s^{slip} \cong \frac{\varepsilon\zeta}{\eta}\frac{dp}{dx}A(1 + \frac{\lambda_D}{b})$.[298] For no-slip boundary condition, the streaming current results in: $I_s^{no-slip} \cong \frac{\varepsilon\zeta}{\eta}\frac{dp}{dx}A$.[280] Then, the streaming current enhancement factor is: $\frac{I_s^{slip}}{I_s^{no-slip}} \approx 1 + b/\lambda_D$. This results in an effective zeta potential ζ_e at slipping interface, which is higher than the intrinsic zeta potential at no-slip surface ζ, with $\zeta_e = \zeta(1 + \frac{b}{\lambda_D})$.[299] Ren et al.[300] theoretically analyzed the effect of varying slip lengths on energy conversion efficiency in nanofluidic channels. As shown in Figure 20e, for a 100 nm-high channel, increasing the slip length to 50 nm could theoretically boost the maximum conversion efficiency to approximately 40%.

Recent studies also suggest that surface charge distribution influences slip length. Xie et al.[301] found that strong Coulombic interactions between counter-ions and the non-uniformly charged surface increase friction, thereby reducing the slip length. In contrast, materials such as graphene and carbon nanotubes exhibit more uniform surface charge distributions, which contribute to enhanced slip.

A straightforward strategy to enhance slip length is utilizing slippery surfaces to reduce flow friction and improve energy conversion efficiency.[302] Inspired by lotus leaves, superhydrophobic surfaces can extend slip lengths to the submicron or even micron scale.[303] The superhydrophobic surfaces are characterized by a very high contact angle (>150º).[304] They are normally created by combining micro/nano scale textures with a low surface energy material.[305] The trapped air within these textures

minimizes the moving friction between liquid and solid surface, allowing liquid to flow more freely over the surface with higher slip length. Malekidelarestaqi et al.[306] simulated the EKEC efficiency on superhydrophobic surfaces with varying slip lengths. Their results showed that increasing the slip length from 0 to 144 nm could improve efficiency by a factor of 3.4. However, while superhydrophobic surfaces can increase slip length through trapped air pockets, the limited surface charge at the liquid-air interface negatively impacts EKEC efficiency. Squires[307] utilized Lorentz reciprocal theorem for the Stokes flow and proposed that if the slip region is uncharged, the effective electrokinetic flow is not enhanced compared to charged non-slip region. In addition, Zhao et al.[308] demonstrated that at moderate to high zeta potentials, electrokinetic flow over a charge-free liquid-gas interface generates lower streaming currents than that over a uniformly charged no-slip surface.

To overcome this limitation, SLIPS have been introduced. SLIPS combines micro/nano scaled textured materials with a lubricating liquid layer infused into those textures.[309] The liquid layer reduces friction and enhances fluid slip by preventing direct contact between the liquid and the solid surface. In the meanwhile, the liquid-liquid interaction provided higher surface charge density than the liquid-air interface in superhydrophobic surfaces.[310] These advantages make SLIPS a promising candidate for electrokinetic applications. Fan et al.[310–315] demonstrated that the SLIPS achieved higher figure of merit than superhydrophobic surfaces, using NaCl solution on SLIPS infused with a low-dielectric-constant lubricant oil. As shown in Figure 20f, they achieved a figure of merit enhancement of 0.043 mV/Pa, outperforming superhydrophobic surfaces with similar surface patterns.

Notably, theoretical and experimental studies have demonstrated that surface charge and boundary slip are intrinsically coupled rather than independent phenomena. Specifically, an increase in surface charge density corresponds to a decrease in slip length.[297,316,317] This dependence of slip length on surface charge inevitably influences fluid behavior at the micro- and nanoscale. Therefore, it is crucial to account for this interdependence while designing substrate.

These findings demonstrate that increasing interfacial slip is a useful strategy for enhancing EKEC efficiency. By reducing frictional losses and promoting ion mobility, approaches such as superhydrophobic surfaces and SLIPS significantly improve charge transport and power generation. The integration of these surface

engineering strategies offers a promising route toward higher electrokinetic performance and more efficient energy harvesting.

4.2.3. Overlapped EDL

In channels, the maximum fluid velocity occurs at the center of the channel. When the channel height (h) is sufficiently large and the EDLs do not overlap, as illustrated in Figure 20g, the majority of the electrolyte within the channel remains electrically neutral. The electrostatic potential decays rapidly within a distance on the order of the Debye length, and the potential at the channel center approaches zero. The neutral electrolyte doesn't contribute to electric output, resulting in low energy conversion efficiency.[318] However, when the channel height is reduced to the scale of the double-layer thickness, typically around hundreds of nanometers, the EDL overlaps. At this scale, the strong electrostatic repulsion from the charged channel walls inhibits the penetration of co-ions into the nanoconfined region, allowing only counterions to be transported. This selective ion transport leads to a higher energy conversion efficiency, a phenomenon commonly referred to as the formation of a unipolar solution.[319]

Osterle et al.[320] were among the first to employ thermodynamic analysis to couple fluid flow with electrical current. They predicted a maximum EKEC of approximately 0.9% in a 100 nm glass capillary. Their group further simulated that the efficiency can be improved to ~4% by reducing the characteristic length of the channel until the EDL overlap (less than twice of λ_D).[321] Ban et al.[322] developed a simple model for water flow without salts or dissolved gases to analyze the effects of overlapped EDL on electro conductivity and potential in the channel. As shown in Figure 20h, The potential distribution reveals a higher potential near the channel walls and a lower potential at the channel center. When the channel height is equal to or smaller than the Debye length ($kh = 0.5$, where $k = 1/\lambda_D$), the dimensionless potential at the channel center increases significantly. With advancements in microfabrication techniques and materials science, experimental verification of EKEC-based energy harvesting has become feasible. Das et al.[323] theoretically investigated the synergistic effect of dimensionless EDL thickness ($\bar{\lambda} = \frac{\lambda_D}{h}$) and ionic Peclet number ($R = \frac{U_c L_c}{\alpha}$, where U_c is characteristic speed, L_c is characteristic length, and α is the thermal diffusivity) on streaming potential. As shown in Figure 20i, the dimensionless streaming potential rise

rapidly with higher $\bar{\lambda}$ until EDL overlapped. After EDL overlapped, or large R ($R > 1$), the dimensionless streaming potential varies weakly with $\bar{\lambda}$. For $R \ll 1$, the dimensionless streaming potential continuously rise with higher $\bar{\lambda}$.

Although overlapping the EDL improves electrokinetic electric output by enabling unipolar ion transport, it may also significantly increase the viscous resistance and pressure drop required for driving liquid motion in the channel.[324] According to the Hagen-Poiseuille equation,[325] $\Delta P = \frac{8\mu Q L}{\pi r^4}$, the pressure drop increases sharply as the channel radius decreases. The hydraulic resistance, defined as $\Delta P/Q = \frac{8\mu L}{\pi r^4}$, scales inversely with fourth power of channel radius. For a cylindrical nanochannel with a radius of 100nm and a length of 1mm, maintaining a flow rate of 1 nL/min requires a pressure drop of $\sim 10^8$ Pa. Furthermore, the wettability of the channel wall plays a critical role by influencing both the direction and magnitude of the capillary pressure. The capillary pressure can be expressed with Young-Laplace equation:[326] $\Delta P_{cap} = \frac{2\gamma cos\theta}{r}$, where γ is surface tension, r is the radius of nanochannel, and θ is contact angle. For hydrophilic channel ($\theta < 90°$), the capillary pressure can serve as a passive driving force to assist fluid infiltration. The maximum assisting pressure can reach up to $\sim 10^6$ Pa. For hydrophobic surfaces ($\theta > 90°$), the $cos\theta$ becomes negative, effectively preventing spontaneous liquid infiltration, and increasing the difficulty of liquid flowing through the nanochannel. Therefore, the maximum critical threshold pressure for initiating flow in hydrophobic channel can reach to the order of $\sim 10^6$ Pa. As a result, the nanochannel with overlapping EDL demands enormous driving forces, making continuous flow energetically expensive and practically infeasible without external pumping. This comparison emphasizes the severe hydrodynamic constraints in overlapped-EDL systems, where electrical output gains must be carefully weighed against mechanical feasibility.
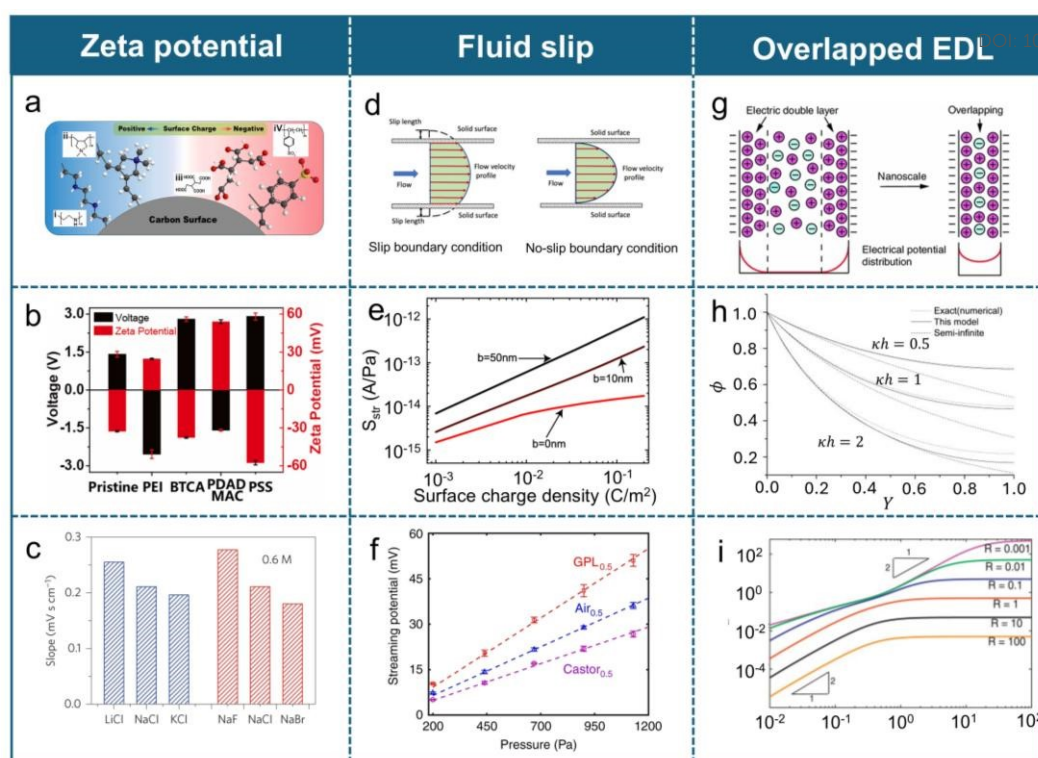
Figure 20. Strategies to improve electrical output. a) Schematic of different molecules modification on carbon particles. Reproduced with permission.[284] Copyright 2019, Elsevier. b) Streaming potential generated on different PSS, BCTA, PEI, PDADMAC modified surface with different zeta potential levels. Reproduced with permission.[284] Copyright 2019, Elsevier. c) The waving potential generated across electrolyte with different ion radius. Reproduced with permission.[274] Copyright 2014, Springer Nature. d) Schematic of velocity field near the interface with no-slip boundary condition (left) and Naiver-slip boundary condition (right) Reproduced with permission.[327] Copyright 2021, Elsevier. e) Increasing the slip length to from 0 nm to 50 nm could theoretically boost the maximum conversion efficiency. Reproduced with permission.[300] Copyright 2008, Wiley. f) The SLIPS can overperforming the generated streaming potential compared to flat and superhydrophobic surfaces with same pattern. Reproduced with permission.[310] Copyright 2018, Springer Nature. g) The overlapped EDL can significantly enhance the counterions concentration at center of channel. Reproduced with permission.[328] Copyright 2012, Springer Nature. h) As the ratio between channel height and Debye length increase, the dimensionless potential significantly reduced. Reproduced with permission.[322] Copyright 2010, American Institute of Physics. i) Variation of dimensionless streaming potential influenced by synergistic effect of dimensionless EDL thickness and ionic Peclet number. Reproduced with permission.[323] Copyright 2013, Elsevier.

4.3. Applications

EKEC has demonstrated great potential in diverse energy-harvesting applications, utilizing various electrokinetic mechanisms. By harnessing interfacial electrokinetic effects, EKEC offers a viable strategy for converting energy stored in fluid into electrical energy, enabling efficient and continuous power supply. These energy harvesters can operate across a wide range of environments, from microscale

85

fluidic systems to large-scale natural bulk water (e.g., ocean, river), making them highly adaptable for real-world applications. Based on their functionality, EKEC applications can be broadly categorized into two major areas: power sources and self-powered devices. The following sections will discuss recent advancements and practical implementations in both categories.

4.3.1. Energy harvesting as power sources

In recent years, significant advancements have been made in utilizing EKEC for diverse power supply applications, including droplet energy generators, wave energy generators, moisture energy generators, evaporation energy generators, and microfluidic energy generators. These systems exploit the movement, phase change, or concentration gradient of water to induce electrical energy through interfacial electrokinetic effects. The diverse mechanisms highlight the adaptability of this energy harvesting approach across different environments and applications.

4.3.1.1. Droplet energy generators

Droplets, which are abundant in nature (e.g., rain droplets, dew droplets, droplets from condensation, etc.), hold immense potential as a renewable energy source.[189,329–332] Over the past decade, extensive research has been conducted on droplet-based nanogenerators utilizing electrokinetic effects. In a pioneering study, Yin et al.[274] demonstrated electricity generation from NaCl solution droplets sliding over a monolayer graphene surface (Figure 21a(i)). As illustrated in Figure 21a(ii), when a 43 μL, 0.6 M NaCl droplet was dragged across a graphene surface at 2.25 cm/s, it induced a voltage of 0.15 mV. The voltage sharply dropped to zero once the droplet ceased movement. Reversing the droplet motion direction produced a voltage of the same magnitude but opposite polarity. The study revealed a direct correlation between the generated voltage/current and both the droplet's velocity and quantity. The electrical output showed a stable linear dependence on speed. Additionally, the output voltage was proportional to the number of droplets of the same size, with the slope for two and three droplets being nearly twice and three times the value of a single droplet, respectively. This finding paved the way for harvesting energy from raindrops. In a prototype rainwater energy-harvesting device (Figure 21a(iii)), an 80 μL, 0.6 M $CuCl_2$ droplet falling from 15 cm above a 70°-tilted graphene surface generated a ~30 mV pulsed voltage and a corresponding short-circuit current of ~1.7 μA. When connected

to a 17.4 kΩ external load, the system produced an output power of 19.2 nW, achieving an efficiency of approximately 1%.

Following this breakthrough, advancements in material science have led to the development of more efficient droplet energy harvesters. Zhao et al.[333] designed a flexible single-electrode raindrop energy harvester using a graphene/reduced graphene oxide (G/rGO) composite film. They recorded periodic current and voltage signals under continuous raindrop stimulation to evaluate the efficiency of converting rainwater into electricity. This device leveraged the pseudocapacitive charging/discharging cycle at the G/rGO-droplet interface, generating stable electrical signals for over 1000 s. By optimizing the graphene ratio, the harvester achieved a maximum output current in the sub-mA order per droplet and a voltage in the hundreds of mV order per droplet. However, prolonged exposure to rain led to ion-induced electron trapping, which degraded the performance.

Kong et al.[334] explored the potential of graphene-based droplet energy harvesting devices by optimizing the device architecture. They reported a graphene microchannel structure that significantly enhanced energy conversion efficiency. As shown in Figure 21b(i), when a 50 µL, 0.6 M NaCl droplet flows through the graphene microchannel at a velocity of 20.55 cm/s from left to right, an output voltage of 150 mV is generated. When the droplet moves in the opposite direction at the same velocity, an equal but opposite voltage is induced. The output performance far surpasses that of graphene in open planar configuration. To further investigate the effect of channel dimensions on energy harvesting performance, they systematically varied the channel width. As illustrated in Figure 21b(ii), when the channel width increases from 150 µm to 350 µm, the expanded liquid-solid interface enhances electron extraction from the graphene surface, thereby increasing the induced voltage. However, in channels wider than 400 µm, the droplet height cannot reach the top of channel during the flow, leading to certain loss in flow velocity. Therefore, the response of output voltage reduced in wider channel. Since the droplet motion is driven by a pressure gradient, the channel length also plays a critical role in energy output. As shown in Figure 21b(iii), when the channel length increases from 2 cm to 5 cm, the output voltage rises from 2.1 mV to 147 mV. However, further elongation of the channel length from 6 cm to 8 cm results in a gradual decline in voltage due to a reduction in flow velocity. Based on these findings, the optimal channel parameters were determined to be 350 µm in width and 5

cm in length, providing a well-balanced design for the maximum droplet-induced energy harvesting.

Furthermore, the drag-induced potential effect has been observed at the water interface of polymer-coated insulator-semiconductor structures.[335] Yang et al.[336] investigated the influence of polymer polarity on droplet energy harvesting by integrating different polymer/graphene layers onto a SiO_2 substrate (Figure 21c(i)). To simulate rainfall conditions, 5 mm-diameter, 0.6 M NaCl droplets continuously fell on a 60°-inclined surface at an initial velocity of ~1 m/s. As shown in Figure 21c(ii), graphene/PET films, which exhibit stronger Na^+ adsorption, produced a pulsed voltage of ~100 mV, whereas no detectable output was observed on graphene/PMMA surfaces. The results indicate that the polymer substrate plays a dominant role in attracting ions to the water/graphene interface, with the PET substrate exhibiting a significantly stronger attraction to Na^+ ions compared to the PMMA substrate.

Recent studies have identified molybdenum disulfide (MoS_2) as a promising alternative to graphene due to its higher electrical resistance, enabling greater voltage generation.[337,338] Aji et al.[339] developed a single-layer MoS_2-based droplet energy harvester (Figure 21d(i)), demonstrating a pulsed voltage of 6 V and a current of 5 nA when a 50 μL, 1 M NaCl droplet was deposited on a 45°-tilted surface, which is outperforming all previously reported droplet-based energy harvesters. They further investigated the impact of different substrates (polyethylene naphthalene (PEN), sapphire, and SiO_2/Si) on power generation. The PEN substrate, characterized by reduced n-type doping,[340,341] increased the MoS_2 film's resistance, resulting in a higher output voltage (Figure 21d(ii)). Similarly, Kumar et al. replaced the substrate with Si_3N_4/Si and achieved an output of 7.3 V and 11 nA when a 60 μL, 0.6 M NaCl droplet dropped from a height of 4 cm and slid across the MoS_2 surface.

These advancements highlight the potential of droplet-based energy harvesting as a viable and scalable approach for sustainable energy conversion. By leveraging novel material architectures and optimizing interfacial properties, researchers continue to push the limits of energy output, opening new possibilities for self-powered systems and environmental energy harvesting applications.
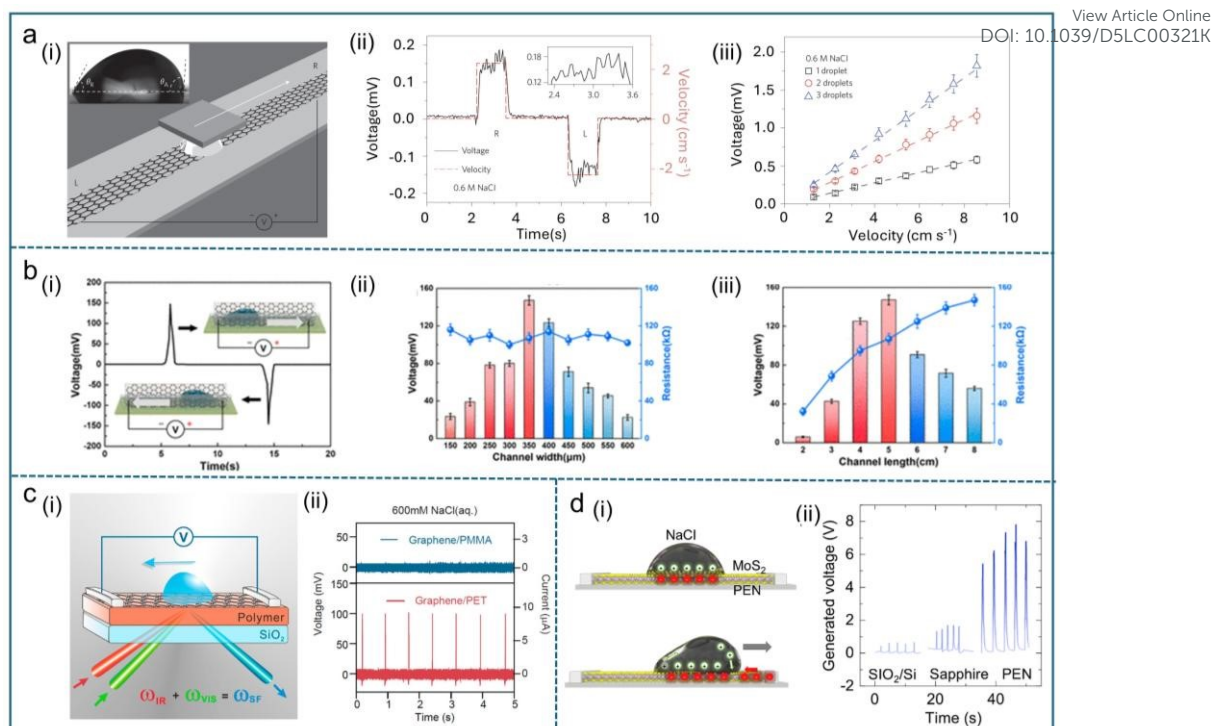
Figure 21. Application of droplet energy generator. a) (i) The droplet slides on the graphene sheet drawn by Si wafer, generating a drag potential. a) (ii) Drawing a droplet from the left end of the graphene strip to the right end and back again generates a voltage of 0.15mV. The reversed droplet velocity will generate a negative output voltage. a) (iii) The voltage induced when moving one, two, and three droplets. The output voltage is proportional to the number of droplets. Reproduced with permission.[274] Copyright 2014, Springer Nature. b) (i) The voltage generated by a 0.6 M NaCl solution when it moves in a graphene microchannel. The voltage direction varies with the flow direction of the droplet. b) (ii - iii) The output voltage of the graphene microchannel device changes at different channel widths and heights. Reproduced with permission.[334] Copyright 2022, American Chemical Society. c) (i) The droplet energy generator consisted of graphene/polymer film on SiO_2 plate. c) (ii) The graphene/PET film can generate 100mV pulse voltage, while it is undetectable on the graphene/PMMA. Reproduced with permission.[336] Copyright 2018, American Chemical Society. d) (i) Mechanisms of electricity generation while the droplet sliding on MoS_2 film. d) (ii) Voltage generated while MoS_2 film underlying on different substrates. Reproduced with permission.[339] Copyright 2020, Elsevier.

4.3.1.2. Waving energy generators

In addition to individual water droplets, bulk water in nature, such as oceans, rivers, and streams, also present immense potential for energy harvesting when subjected to waving motions.[342,343] Yin et al.[275] were the first to develop graphene-based waving energy generators (Figure 22a(i)). They discovered that once a graphene sheet was inserted into an ionic solution, a significant voltage could be induced even in the absence of a pressure gradient. As shown in Figure 22a(ii), the induced fluctuation potential is proportional to the insertion speed and the size of the sheet. When a

graphene sheet is inserted into a NaCl solution at a speed of 3.1 m/s, a 2×10 cm² graphene sheet can generate a voltage as high as 3 mV. When the graphene sheet is withdrawn, an opposite voltage is generated. Notably, as shown in Figure 22a(iii), the voltage generated by the insertion of the graphene sheet increases linearly with speed, while the voltage generated by withdrawal remains almost unchanged once the speed exceeds the critical threshold. This is because the electrolyte cannot detach from the graphene sheet in time. By connecting multiple devices in series and parallel, voltages as high as 0.1 V and currents up to 11 µA can be generated, sufficient to stimulate the frog's sciatic nerve and induce a sharp contraction of the gastrocnemius muscle. This novel device expands the development of remote power generation in environments such as oceans and rivers.

Inspired by the advancement of waving potential, Tan et al.[344] developed a thin-film wave energy generator by mixing graphene and carbon black with aqueous polyurethane, then casting the mixture onto substrates such as glass, plastic, and ceramics (Figure 22b(i)). By optimizing parameters such as the carbon dose, wave frequency, tilt angle, and seawater temperature, the generator, with a size of 15 cm², can produce voltages greater than 20 mV and currents greater than 10 µA (Figure 22b(ii)). Under continuous wave impacts, these thin-film generators can maintain stable output for more than five hours. This method of harvesting wave energy offers new opportunities for low-investment, scalable power output with high stability.

Fei et al.[345] improved the wave energy harvester by using a dual-graphene-sheet system. Unlike the fluctuation potential observed in single graphene sheets, the voltage in the dual-graphene system is generated within the solution. In such a system, as shown in Figure 22c(i), the moving graphene sheet serves as the driving force for ion motion, while the stationary graphene acts as a reference electrode. Due to the low carrier density and high ion adsorption/desorption capacity of the graphene sheets, when a certain number of ions are adsorbed onto the graphene, there are insufficient electrons to shield the ion charges. As a result, a noticeable current can be induced in the external circuit outside the solution. As shown in Figure 22c(ii), when a single graphene sheet (Gr_R) is inserted into the liquid surface, the voltage across the resistor gradually increases and peaks at 60 mV. After pulling Gr_R from the solution, the voltage drops significantly and reaches -120 mV before the sheet completely stops near the liquid surface. Shortly thereafter, the voltage returns to zero as the system reaches equilibrium.

They also calculated the output power per unit area of graphene, which shows a nonlinear relationship with the external resistance. As shown in Figure 22c(iii), during the insertion of graphene, the maximum output power occurs when the external resistance is 0.1 MΩ. During the withdrawal of graphene from the liquid surface, the maximum output power is observed at 0.6 MΩ, reaching approximately 1.6 mW/m². They simulated that simultaneous movement of the graphene sheets in opposite directions could further enhance instantaneous power. This method of collecting water energy provides new insights for the development of wave energy harvesters.

The ongoing advancement of material science, particularly the exploration of novel composites and coatings, will likely lead to even more efficient, cost-effective, and environmentally friendly wave energy harvesting technologies.
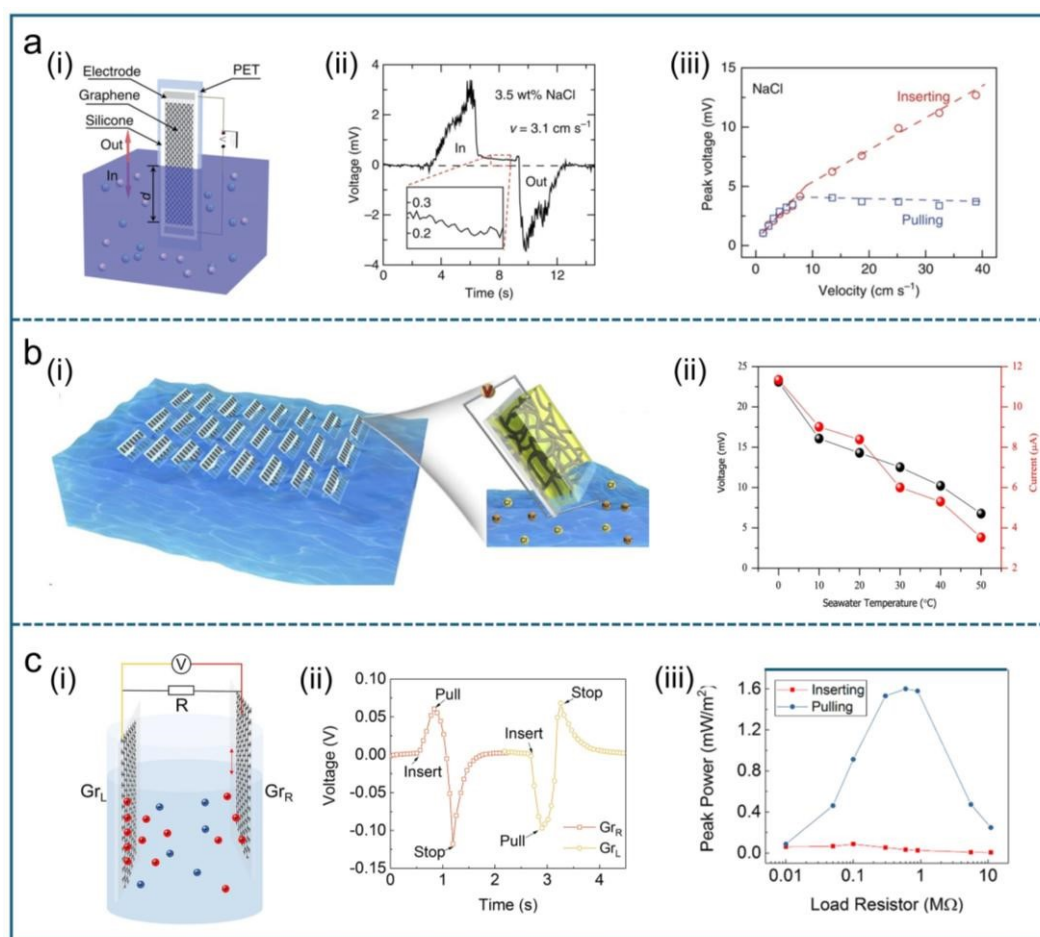
Figure 22. Application of waving energy generator. a) (i) The graphene is placed on a PET substrate and moved vertically on the water surface in the container to generate waving potential. a) (ii) The voltage signals generated when the sample is inserted and pulled out of a 0.6 M NaCl solution at a speed of v = 3.1cm/s. a) (iii) The relationship between the magnitude of the positive peak voltage and the negative peak voltage and the speed at which graphene moves across the surface of a 0.6 M NaCl solution. Reproduced with permission.[275] Copyright 2014, Springer Nature. b) (i) The schematic

of wave energy generation stations in the ocean. b) (ii) Optimized output performance with 80 wt% G-CB films at different seawater temperatures. Reproduced with permission.[344] Copyright 2018, Elsevier. c) (i) The schematic of two graphene system waving energy generators. c) (ii) The voltage generated while separately moving each graphene across NaCl solution. c) (iii) The output power density of graphene with different external resistance while inserting and pulling across NaCl solution. Reproduced with permission.[345] Copyright 2019, Elsevier.

4.3.1.3. Moisture energy harvester

As a fundamental and abundant form of water in nature, moisture has inspired extensive research on moisture-induced energy generators for sustainable power generation.[2,346–350] Moisture energy conversion typically occurs when moisture absorption or transport within materials induces charge separation and electrical output.[278,351–353] This procedure requires neither temperature variation nor mechanical movement, and produces no pollutant byproducts, making it an attractive option for environmentally friendly energy harvesting. Recent advancements have led to the development of various moisture energy generation devices that harness this renewable energy source.

Zhao et al.[283] reported a graphene oxide (GO) film with a carboxyl gradient capable of adsorbing and condensing moisture within its nanoscale pores. The oxygen-to-carbon (O/C) atomic ratio was approximately 0.52 at the bottom and 0.22 at the top of the film. Due to the strong hydrophilicity of carboxyl group, the device absorbs water molecules upon exposure to moisture. As the water molecules accumulate in the oxygen-rich regions of GO film, localize solvation effects weaken the O-H bonds within carboxyl group, leading to the release of free H^+ ions. In the GO film, the carboxyl group exhibit a gradient distribution, resulting in a corresponding H^+ concentration gradient. This gradient drives the diffusion of H^+ ions generating a streaming potential induced by moisture flow. The device, comprising a 2.8 mm-thick GO film clamped between two asymmetrically sized gold electrodes, produced a pulse voltage of ~20 mV and a current density of 5 µA/cm² at ~30% relative humidity (RH).

To expand moisture energy generators applications in portable electronics, Cheng et al.[354] developed a flexible in-plane moisture-electric converter (IPMEC) based on GO assembled films. The IPMEC device features two laser-rGO planar electrodes integrated with GO layers in between, exhibiting an oxygen-containing functional group gradient, ensuring full exposure to moisture sources. Water molecules in humid environments interact with GO and induce an ion concentration gradient along

the in-plane direction of the GO layers (Figure 23a), resulting in a substantial electrical output (~70 mV, 12 mA/cm²) in an external circuit.

Shen et al.[355] further enhanced moisture energy generators performance by constructing a hydrophilic TiO_2 nanowire network, which forms a 3D nanoconfined channel architecture to facilitate moisture absorption and diffusion (Figure 23b(i)). Under alternating high and low humidity conditions, the device generated a pulse output of 0.6 V and 4 μW/cm² (Figure 23b(ii)), outperforming previously reported carbon-based moisture energy generators by two orders of magnitude. Notably, moisture from human breath provides sufficient energy to power a commercial LED. The device also exhibited intrinsic flexibility, maintaining stable output characteristics even after 10,000 bending cycles.

The performance of moisture energy generators is significantly influenced by both ambient relative humidity and the hygroscopic properties of the materials. Insufficient hygroscopicity at low humidity may lead to inadequate ion dissociation, whereas excessive hygroscopicity at high humidity results in rapid saturation, limiting device longevity. To extend the sustainability of energy conversion, one promising strategy involves the design of nanostructured architectures to maintain moisture difference in the device with heterogeneous chemical structure. For instance, Huang et al.[356] proposed a sandwich-structured moisture energy generator composed of Ag/pristine GO/gradient-reduced GO/Au (Figure 23c). The bottom GO layer offers a rich supply of mobile electrons, while the Schottky junction at the GO/Ag interface rectifies ion flow and prevents electron backflow. This device effectively harvested energy from atmospheric moisture over a wide temperature (25.8°C–50.8°C) and RH (5–95%) range, maintaining a stable open-circuit voltage of 0.6 V for over 120 hours. By establishing a self-sustained humidity gradient, this strategy significantly reduces limitations associated with environmental conditions.

Xu et al.[357] introduced a novel approach using a flexible polyelectrolyte membrane, poly (4-styrenesulfonic acid) (PSSA), to achieve efficient moisture-induced power generation (Figure 23d(i)). Their polymer-based moisture energy generator, consisting of a 1 cm² PSSA membrane, delivered an open-circuit voltage of ~0.8 V (Figure 23d(ii)) and a short-circuit current density of ~0.1 mA/cm², sufficient to power various electronic devices. By integrating two polymer-based moisture energy generators in series, they designed a wearable mask capable of harvesting energy from

human respiration. During normal breathing, the device could charge a capacitor to 0.9 V in 30 minutes. Additionally, both boiling water vapor and mist from an ultrasonic humidifier effectively contributed to energy harvesting. As illustrated in Figure 23d(iii), six PMEG units were connected in series to power an LED light. When placed near a commercial ultrasonic humidifier, the generated mist gradually reached the PMEGs, successfully illuminating the LED. The remarkable flexibility and superior electrical output of PMEGs highlight their tremendous potential in wearable energy-harvesting systems. These groundbreaking studies highlight the immense potential of MEG technologies, paving the way for future research and further advancements in this field.
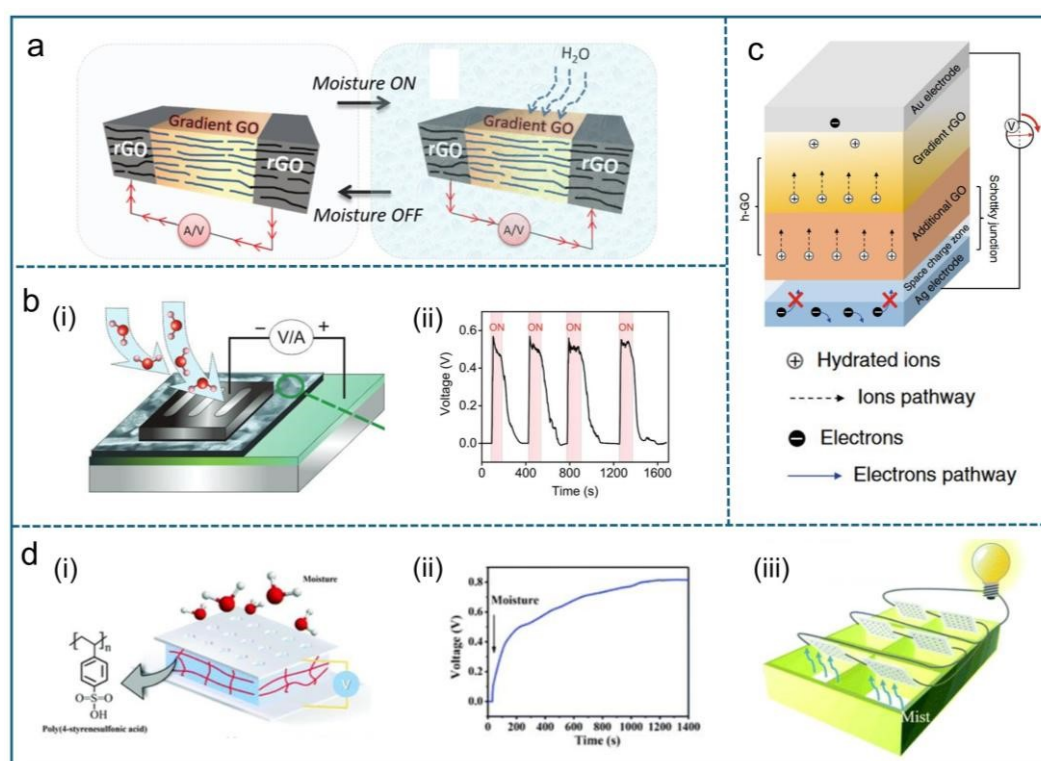
Figure 23. Application of moisture energy generator. a) Schematic of moisture-electric conversion cycle. The arrows represent induced voltage and current while moisture is in present and absence. Reproduced with permission.[354] Copyright 2018, Elsevier. b) (i) Schematic of TiO_2 based moisture energy generator generating electricity while harvesting moisture in the environment. b) (ii) Voltage generated in response to the 85% RH level. Reproduced with permission.[355] Copyright 2018, Wiley. c) Schematic of asymmetric sandwich structure of moisture energy generator. The feed layer with additional GO supplements the depletion of ions in the gradient rGO, and the special electrode/h-GO interface blocks the free electrons from passing through h-GO and regulates their flow direction, which greatly promotes the electrical output. Reproduced with permission.[356] Copyright 2019, Royal Society of Chemistry. d) (i) Schematic of PMEG, which consists of PSSA membrane between two gold electrodes. The upper electrode is manufactured with holes for efficient moisture access. d) (ii) The generated output voltage on a single 1 x 1 cm^2 PSSA membrane under constant moisture. d) (iii)

A mist powering system built by 6 PMEG units connected in series. Reproduced with permission.[357] Copyright 2019, Royal Society of Chemistry.

4.3.1.4. Evaporation energy generators

The evaporation of water through ambient heat absorption is a continuous and spontaneous natural process.[19] Evaporation energy generators typically employ the interaction between nano structures or porous materials and electrolyte flow induced by evaporation to generate streaming potential, achieving efficient low-grade thermal energy conversion.[358,359] In 2017, Xue et al.[353] pioneered the use of the electrokinetic principle to harvest electrical energy from the natural evaporation of water through carbon black (CB) films. This approach effectively harnesses low-grade thermal energy under ambient conditions. The device consisted of a porous CB film (Figure 24a) with multi-walled carbon nanotube electrodes deposited at both ends. Water was absorbed at the bottom of the device and transported upward through the CB film via capillary action. Water evaporated on the exposed CB surface to sustain the capillary flow. This CB-based device generated a continuous voltage of up to 1.0 V and an open-circuit current of 150 nA, marking a significant advancement in evaporation-driven electrokinetic generators.

Inspired by the high porosity of CB, Zhang et al.[360] explored the use of three-dimensional GO to construct evaporation-based energy harvesters. Their device, designed as a 3D GO sponge cup, achieved an output voltage of 0.63 V and a power density of 1.74 mW/cm². Subsequent studies employed chemical etching to disperse GO, increasing the concentration of carboxyl groups and nanopores on GO film, thereby further enhancing device performance. These modifications improved mass transport and evaporation rates, significantly boosting overall efficiency.

Metal oxides are considered to be charged in aqueous suspension due to amphoteric dissociation of surface hydroxyl groups or adsorption of hydroxo complexes from hydrolysis products.[281] They can achieve relatively high surface zeta potentials, making them highly suitable for evaporation energy harvesting, particularly in the form of nanoparticles and nanowires. Shao et al.[282] utilized Al_2O_3 nanoparticles coated hydrophilic PET films to collect evaporation energy. Their device produced a continuous voltage of 2.5 V and a current of 0.8 mA, with sustained operation for up to 10 days. Li et al.[361] fabricated a ZnO nanowire array with a 180 nm pitch, encapsulated in poly (vinyl chloride-co-vinyl-co-2-hydroxypropyl acrylate) (PVC). By inducing ethanol droplet evaporation on the ZnO surface, the device generated a voltage of 133

mV with a duration of 150 seconds. This study demonstrated that non-randomly distributed nanochannels can also effectively harvest energy from evaporation, highlighting the potential of nanowire structures for energy harvesting applications.

Biomass materials with intrinsic nanostructured channels, such as cellulose and lignin, offer excellent biocompatibility and degradability, making them promising candidates for environmentally friendly energy harvesting.[362,363] Zhou et al.[364] leveraged the abundant micro-scale channels in wood to harvest energy from evaporation (Figure 24b(i)). By optimizing surface potential and hydrophilicity through citric acid esterification of hydroxyl groups, the wood-based device generated a continuous voltage of 300 mV and a current of 10 mA. They investigated four different wood types for evaporation energy generation, evaluating the influence of wood species and microchannel orientation on electrical output. As shown in Figures 24b(ii - iii), measurements of a 5 cm × 5 cm × 1 cm wood device revealed that beech wood exhibited the highest performance, generating currents above 2 μA and voltages exceeding 30 mV. This performance variation was attributed to differences in hydrodynamic resistance due to their different porous dimension among wood materials (ranging from 5 μm - 40 μm). Additionally, comparing devices with identical wood types, vertically aligned channels demonstrated significantly higher current and voltage outputs than horizontally aligned channels, because the former is aligned with water evaporation direction. Similarly, Jiao et al.[365] developed a carbonized freeze-dried carrot slice device, achieving an open-circuit voltage of 0.8 V and a short-circuit current in the tens of milliamps per device.

Su et al.[366] adopted an innovative approach by using 160 plasma-treated wool strips coated with Ketjen black powder to absorb and evaporate seawater, successfully charging a supercapacitor to 1.6 V within 5.5 hours. However, continuous seawater evaporation led to salt crystallization on the evaporation surface, reducing the evaporation rate with time.[367–369] To address this issue, Peng et al.[370] designed an asymmetric fluid evaporator enabling gravity-assisted salt collection, and permeation-induced electrokinetic generation. The evaporator was fabricated by spray coating tannic acid modified MoS_2 nanosheets on partial area of metal-organic frameworks functionalized polyacrylonitrile textiles (PAN) to create asymmetrical structure. While drenching with water, the asymmetrically deposited textile induced varied ionic adsorption behavior at different sites, resulting in formation of gradient EDL. The salt

always tends to crystallize at one end of textile and fall off under the drive of gravity, improving the sustainability of the evaporation efficiency and electrical harvesting. Their experimental results demonstrate that after 60 hours of continuous operation in a 7.5 wt% saline solution, the device maintains a stable evaporation rate of 1.31 kg/m²·h and a voltage output of 0.514 V.

For evaporation energy devices, elevated temperatures can accelerate liquid evaporation, thereby significantly enhancing power output.[371] Thus, integrating photothermal materials can further improve water evaporation and energy generation efficiency. Xiao et al.[372] developed a solar-driven evaporator using a bilayer carbon nanotube/cellulose paper structure, asymmetrically modified with PDMS on half area of carbon nanotube substrate (Figure 24c(i)). When the hydrophobic PDMS coating is applied to the surface of carbon nanotubes (CNTs)/paper, it significantly alters the light path, enhancing the visibility of the black CNTs film on the reverse side. As a result, the paper's appearance changes from white to black. Under varying illumination intensities, as depicted in Figure 24c(ii), the CNT/paper device exhibited an increase in voltage and current from 0.47 V and 15 µA in darkness to 0.6 V and 22 µA under 500W of solar irradiation.

Harvesting energy from human body heat presents challenges due to the small temperature gradients involved.[373] Liu et al.[374] utilized a porous carbon membrane and DI water (Figure 24d) to generate electricity from body heat for directly powering the wearable wristband. Driven by evaporation under a low thermal gradient, this device highlights the potential for low-temperature thermal energy harvesting and self-sustaining wearable sensor systems. Their device achieved an open-circuit voltage of 0.89 V under a temperature difference of only 4.2 °C, sufficient to directly power electronic devices.

These advancements underscore the immense potential of evaporation-driven electrokinetic generators, offering promising pathways toward scalable, efficient, and multifunctional energy harvesting solutions.
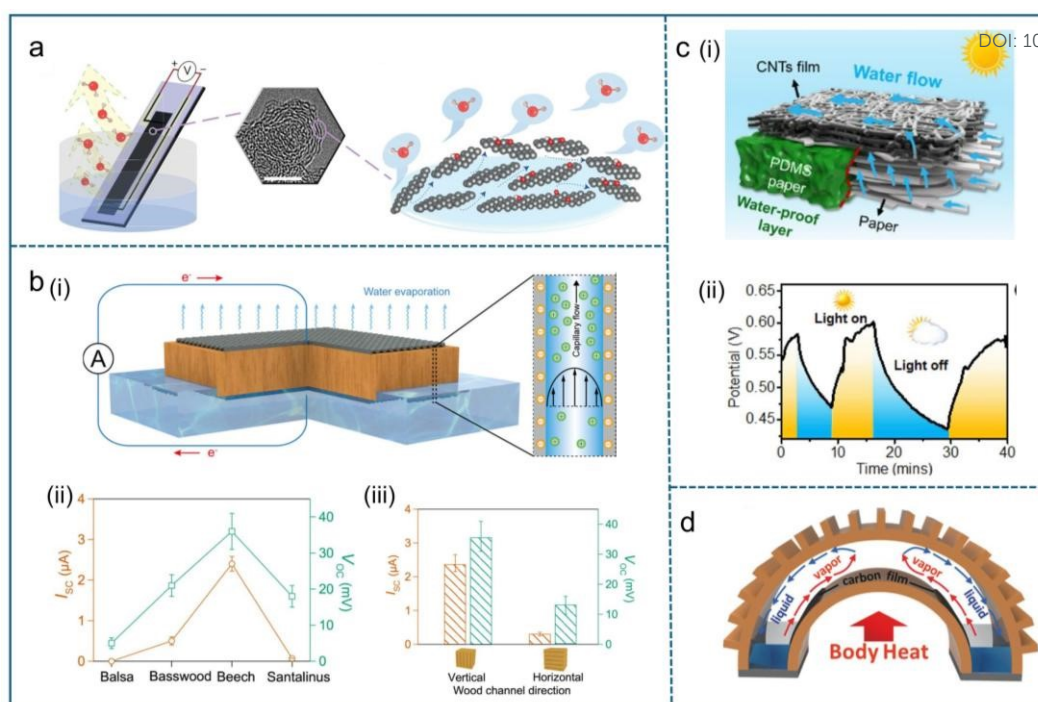
Figure 24. Applications of evaporation energy generator. a) Schematic of setup for harvesting energy from water evaporation through CB film. Reproduced with permission.[353] Copyright 2017, Springer Nature. b) (i) Schematic of the electricity generation induced by evaporation in a piece of wood. The microchannels of the wood piece are vertically aligned. When water flows in the microchannels, the inner surfaces of the channel are negatively charged, resulting in a positively charged flow. b) (ii - iii) Output voltage and current of different wood species and wood channel direction. Reproduced with permission.[364] Copyright 2020, American Chemical Society. c) (i) Schematic of solar-driven evaporator using a bilayer carbon nanotube/cellulose paper structure. c) (ii) Under solar irradiation, the electrical output enhanced compared to the dark environment. Reproduced with permission.[372] Copyright 2020, Elsevier. d) Schematic of self-powered wearable wristband. While the DI water evaporated driven by body heat, the porous carbon membrane harvesting the energy from evaporation to electricity. Reproduced with permission.[374] Copyright 2018, Wiley.

4.3.1.5. Microfluidic energy generators

Beyond bulk water in nature, electrokinetic technology is also highly applicable to microfluidic and lab-on-a-chip systems, as well as wearable microfluidic devices. When fluids flow through micro-/nanochannels, their mechanical energy can be converted into electricity via streaming potential.

Human daily activities involve many mechanical motions, providing an opportunity for energy harvesting. Li et al.[375] demonstrated a flexible microfluidic nanogenerator (MFNG) that utilizes streaming potential to convert ambient mechanical energy into electricity (Figure 25a(i)). The MFNG consists of ten microchannels, each with a width of 100 μm. When a force is applied to one end of the reservoir, the electrolyte flows through the microchannel under pressure, generating a streaming

potential. When the force is removed, the electrolyte backflows, producing an opposite streaming potential. They investigated the relationship between the generated voltage/current and the applied force. As shown in Figure 25a(ii), both voltage and current increase almost linearly with the applied force, suggesting that using larger force sources (e.g., footsteps) could further enhance the output. A simple finger press can generate a pulse voltage of ~1.5 V and a current of ~1 µA across a total effective cross-sectional area of 1 mm² in the microchannel, which is sufficient to power a commercial liquid crystal display (LCD) (Figure 25a(iii)). The output performance of MFNGs can be further optimized by adjusting parameters such as fluid type, solution concentration, microchannel surface properties, and geometric dimensions. This approach presents a promising strategy for developing power supply systems that harness mechanical energy from the human body.

Additionally, microfluidic systems are widely employed in biomedical diagnostics. The streaming potential effect can be utilized to convert the mechanical energy of fluid flow into electricity, powering other microfluidic devices. Zhang et al.[31] fabricated a microfluidic energy generator using soft lithography. They incorporated a patterned micropillar array in the channel, forming a quasi-porous structure, to increase contact area between liquid solution and channel walls. Compared to microchannels without internal structures, this design significantly enhanced power output by increasing the liquid-solid interfacial area. Furthermore, they developed a self-powered fluidic sensing system, where the microfluidic energy generator supplied energy to a single nanowire (NW)-based pH sensor (Figure 25b(i)). As illustrated in Figure 25b(ii), when a 1 µM KCl solution flows through the device at 0.4 mL/min, it generates a continuous voltage of ~160 mV and a current of 1.75 nA.
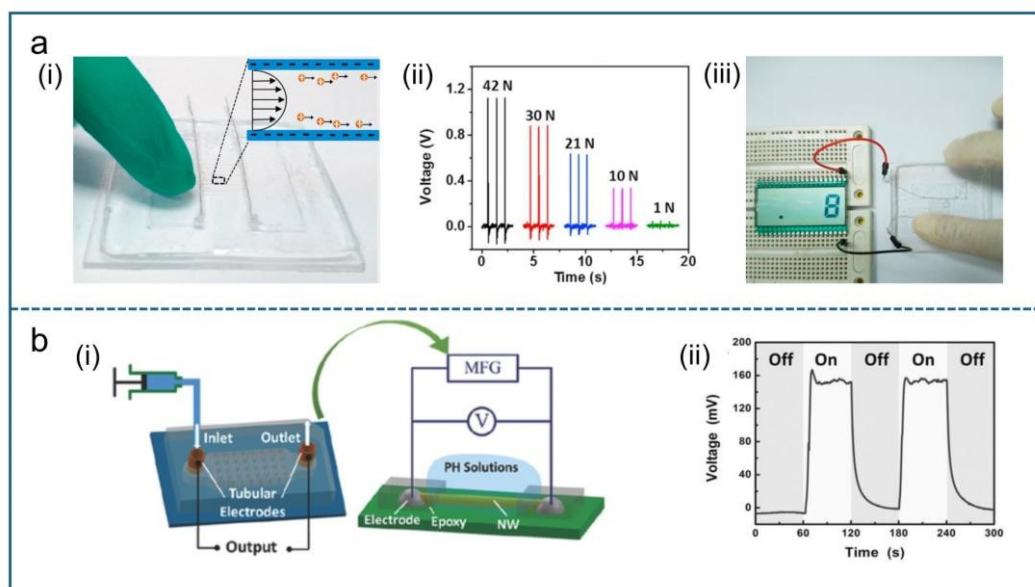
Figure 25. Applications of microfluidic energy generator. a) (i) Schematic of flexible MFNG consists of ten microchannels. The width of each channel is 100 μm. a) (ii) The voltage generated by MFNG at different external forces. a) (iii) Photo of LCD powered by MFNG directly. Reproduced with permission.[375] Copyright 2016, Elsevier. b) (i) Schematic of microfluidic nanogenerator with porous patterned structure in the microchannel, where the microfluidic nanogenerator supplied energy to a single NW based pH sensor. b) (ii) Voltage generated from microfluidic when a 1 μM KCl solution flows through the device at 0.4 mL/min. Reproduced with permission.[31] Copyright 2015, Wiley.

4.3.2. Self-powered devices

In addition to working as power supplies, electrokinetic technologies can function as self-powered sensors due to their ability to generate electrical signals in response to external stimuli. Self-powered devices can effectively enable remote sensing, computing, storage, and communication, significantly reducing wiring costs and conserving energy.[376]

The output electrical signal of EKEC exhibits high sensitivity to fluid motion, making them ideal for monitoring dynamic fluid properties. Newaz et al.[377] developed a graphene field-effect transistor (GraFET) to detect ionic concentration and flow rate in liquids. They fabricated microchannels with dimensions of 80 μm in height and 50 μm in width using soft lithography on PDMS and the transistor was sealed within the microchannel as a probe. When fluid flowed through the channel, the electrical signal of GraFET increased linearly with the local flow velocity. Additionally, at a constant flow rate, the output electrical signal exhibited an exponential decay with increasing

ion concentration. This graphene-based device demonstrated the capability to detect flow rates as low as 70 nL/min and ion concentrations down to 40 nM.

Similarly, the drawing potential generated by droplets moving across graphene surfaces exhibits a strong linear correlation with droplet moving velocity and direction, making it a promising candidate for droplet motion sensing. Yin et al.[378] further leveraged this phenomenon by designing a system that detects brush strokes using two pairs of orthogonally placed electrodes. As illustrated in Figure 26a(i), a square graphene sheet was integrated with two electrode pairs (E1+/E1- and E2+/E2-) positioned perpendicularly on four edges. When a brush was immersed with a 0.01M NaCl solution and wrote on the graphene sheet, the voltage V1 between E1+/E1- responded positively to horizontal strokes from left to right. And the voltage V2 between E2+/E2- responded positively to vertical strokes from top to bottom. By analyzing the voltage signals detected between the electrodes, fundamental brushstroke patterns could be easily recognized. (Figure 26a(ii)). Furthermore, more detailed information from electrical signals, such as brush tip sharpness, writing speed, and applied pressure, remains an area for further exploration.

Beyond directly sensing fluid velocity, energy sources that induce velocity changes can also be detected. Kong et al.[334] developed a flexible self-powered pressure sensor based on graphene/PDMS microchannels, utilizing the principle that energy conversion at liquid-solid interface correlates positively with pressure. As pressure increased, deformation and displacement of droplets within microchannel were enhanced, leading to greater motion speed and higher voltage generation. Due to the flexible mechanical properties of graphene/PDMS films and the low Young's modulus of liquid droplets,[27] the sensor remained highly responsive to external stimuli even under low pressures. They affixed the flexible device to a human wrist to monitor body posture. When the extended wrist transitioned into a bent state, the droplet deformation and displacement within the flexible device induced a rapid voltage response. Their testing demonstrated a response and recovery time of 36.4ms and 239.2 ms, respectively, under a 2.138 kPa load/unload cycle. Furthermore, under a 1.895 kPa pressure cycle, the sensor maintained a stable signal over 1000 cycles, further affirming its potential for wearable applications.

The sensitivity of self-powered electrical devices to temperature and humidity enables their application in environmental sensing. Water infiltration-induced

geological disasters often result in severe economic loss, casualties, and environmental damage.[379–381] To address this issue, a seepage early warning system based on EKEC was proposed (Figure 26b).[382] This system employed MoS_2-functionalized filter paper as the sensing material, capable of sensing water seepage as low as 2 μL. When the filter paper was exposed to water, spontaneous counterion adsorption occurred in the wet region, forming an EDL at the electrolyte-solid interface. This process generated a potential difference between the wet and dry regions of the paper. Under the influence of humidity gradient, water gradually migrated from the wet region to the dry region, carrying adsorbed ions and generating an electrical current. As evaporation progressed and moisture decreased, the output voltage and current correspondingly declined until disappearing completely upon full evaporation. Due to the strong hydrophilicity of filter paper, the system achieved a detection resolution on the order of seconds. When a droplet was introduced at the negative electrode of the filter paper, the voltage rapidly increased from 0 mV to 110 mV within 10s. Additionally, the system demonstrated stable multi-cycle alarm functionality. After 10 consecutive wet-dry cycles, the current decreased only from 18.3 μA to 14.7 μA, shown 80% of current was retained.

Besides environmental monitoring, self-powered electrical technology can also be used to detect the humidity emitted by the human body to promote the advancement of human health. Respiration and perspiration can serve as indicators of physiological conditions and can be monitored through periodic humidity variation. Zhao et al.[283] developed a breath sensor utilizing GO films to monitor breathing status. While humans are under resting conditions, with an average breathing rate of 13 times/minute (RH ~21%), the sensor generated an output voltage of ~18 mV. After one hour of jogging, the breathing rate increased to 28 times/minute (RH ~48%), and the sensor's voltage output rose to 30 mV. The frequency and amplitude of the pulsed voltage signals directly reflected breathing activity. With a similar framework, Li et al.[385] replaced GO with bio-compatible cellulose nanofibers and fabricated a smart mask capable of monitoring human breathing activities. The voltage pulses and amplitudes generated by the sensor closely correlated with respiratory rate and intensity. Additionally, this bio-nanofiber-based sensor exhibited high biocompatibility with human skin cells and could fully degrade in natural soil within 35 days, demonstrating its potential as a next-generation respiration sensor.

Due to sweat and moisture evaporation, the air surrounding human fingers generally exhibits elevated humidity levels. When fingers approach or touch objects, RH fluctuations occur in the vicinity. This property enables the development of self-powered touch sensors utilizing the high humidity sensitivity of electrical devices. Shen et al.[386] fabricated a tactile sensor based on TiO_2 nanowire networks that responded to the presence of a human finger by generating a pulse voltage of 150 mV upon contact. Cheng et al.[354] further advanced this concept by developing a rGO-based tactile sensor that responded to finger proximity without direct contact. As illustrated in Figure 26d, when the finger approached the device at distances of 1, 2, and 3 mm, the sensor generated corresponding current densities of 10, 8, and 4.5 mA/cm², respectively. This sensor could be utilized for real-time finger tracking applications.

Self-powered electrical technology also holds promise for information storage applications. Liang et al.[383] developed a fiber/rGO based moisture energy harvester to generate electrical signals (Figure 26c(i)). The device exhibited distinct voltage responses depending on whether it was laser-treated. The untreated units produce 0 mV output in response to humidity changes, representing the "0" (off) state. In contrast, the laser-treated units exhibit higher response voltages, representing the "1" (on) state. These flexible sensor units could be integrated into arrays and embedded within wearable fabric. Each sensor unit was positioned at different locations within the fabric and could be programmed to represent either "0" or "1" states, enabling the fabric to transmit digital information, thus offering potential applications in wearable data storage and communication systems. As shown in Figure 26c(ii), an array of 136 information units is woven into a 3 cm × 7 cm textile, with each unit programable to "0" or "1". Therefore, this fabric can convey 2^{136} different kinds of information. Each unit in the network is assigned a coordinate, presenting their position in the fabric. This highly integrated fabric retained excellent mechanical flexibility, allowing it to be conveniently bent to be attached to a person's wrist, or integrated to face mask as a new type of wearable electronic tag. Furthermore, electrochemical treatment could modulate unit voltage, further enhancing the diversity of electronic tag information expression. For example, Figure 26c(iii) shows a pattern expression of the "BIT" shape signal based on different voltage responses.
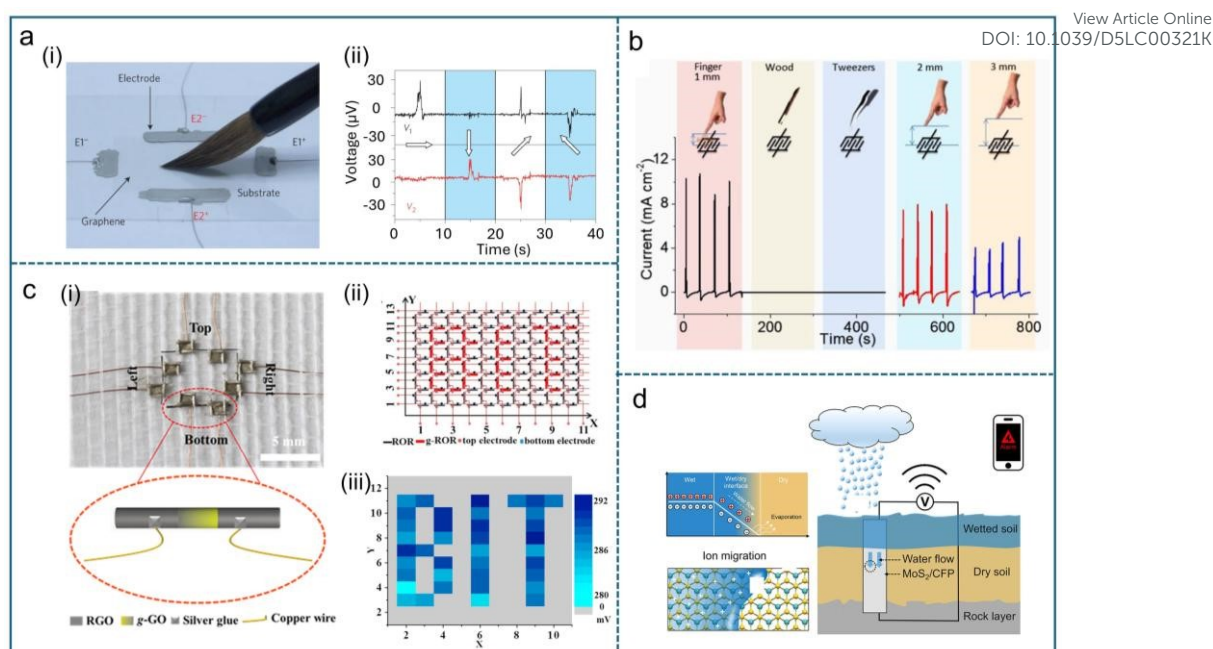
Figure 26. Applications for self-powered devices. a) (i) Photo of handwriting with a brush on graphene between four electrodes: E1$^+$, E1$^-$, E2$^+$ and E2$^-$. a) (ii) The stroke directions by the drawing potential between electrodes can be sensed based on generated voltage signal. Reproduced with permission.[274] Copyright 2014, Springer Nature. b) Schematic of transpiration energy power generator for water seepage early warning system. Reproduced with permission.[382] Copyright 2023, American Chemical Society. c) (i) The units "0" and "1" can be integrated into the textile by random permutation and combination. Four information units are integrated into a piece of textile. c) (ii) Schematic of array of information storage units. c) (iii) Based on different voltage signal, the units are showing the logo of "BIT". Reproduced with permission.[383] Copyright 2017, Elsevier. d) Generated streaming current with different objects and the changed position of fingers. Reproduced with permission.[354] Copyright 2018, Elsevier.

4.4. Challenges and opportunities

Compared to conventional power generation, electrokinetic effects offer several advantages, including cleanliness, noiseless operation, environmental friendliness, abundant energy resources, and a simple energy conversion process. However, electrokinetic systems still face several challenges.

First, the power density and energy conversion efficiency remain relatively low. The performance of electrokinetic generators is largely governed by interfacial effects, as charge generation primarily occurs at the interface between fluids and solid surfaces. However, in situ characterization techniques to explain the potential charge generation and transfer processes at the atomic level in liquid-solid phase interactions remain scarce, hindering a deeper understanding of these phenomena.

Enhancing surface charge density through material optimization and surface morphology modification can improve performance to some extent but charge density

cannot be increased indefinitely. Alternatively, improving interfacial slip length can effectively enhance device output. The liquid-liquid interface on SLIPS facing durability challenges due to the depletion of lubrication liquid. Exploring the liquid-polyelectrolyte interface holds great potential for enhancing electrokinetic performance by facilitating higher slip[387] lengths and sustainable energy harvesting.

Additionally, the synthesis of materials and the design of devices still lack standardization. There is a need to establish a reliable connection between material properties and output power. Developing standardized fabrication protocols and characterization methods will be crucial for optimizing material performance and ensuring the scalability of electrokinetic energy harvesting technologies.

Finally, most reported devices remain at the laboratory demonstration stage, with significant scale-up challenges hindering real-world applications. The scalability of microfluidic devices remains uncertain, as issues such as flow blockage and charged droplet loss can arise upon upscaling.[388] Additionally, real-world operating conditions are more diverse and complex. For example, biofouling and surface contamination can accumulate on the device, leading to performance degradation.[212] Therefore, developing electrokinetic systems with stable self-cleaning capabilities could enhance their adaptability across various application environments.

Given the growing demand for sustainable and renewable energy solutions, electrokinetic energy harvesting presents a promising avenue for future advancements in energy generation. The ability to convert ambient mechanical energy, such as fluid flow or droplet impact, into usable electrical power offers a significant step toward reducing reliance on fossil fuels. As research continues to address the current challenges, the potential applications of electrokinetic systems are vast, spanning from self-powered sensors and portable devices to large-scale energy harvesting in industrial or environmental settings. Furthermore, with advancements in material science, microfluidics, and system integration, electrokinetic energy harvesting could play a key role in the development of autonomous, self-sustaining devices that operate efficiently in diverse, real-world conditions. Continued exploration of this field holds the promise of unlocking new paradigms in sustainable energy technologies, ultimately contributing to the broader goal of expanding energy harvesting strategies and minimizing environmental impact.

5. Comparison among REWOD, TENGs, and EKEC

In the field of energy harvesting and self-powered sensing, the three technologies—REWOD, TENGs, and EKEC—each have distinct characteristics, forming a complementary development pattern. These energy conversion mechanisms, based on liquid-solid interfacial effects, are opening new pathways for distributed energy supply and the construction of smart sensing systems. For systematic comparison, Table 2 summarizes representative data for these three technologies across key dimensions such as working principles, output performance, manufacturing costs, and application scenarios.

REWOD technology relies on capacitance changes caused by droplet deformation on dielectric layers, with a theoretical power density reaching the order of 10^4 W/m². It is particularly suitable for energy harvesting and signal monitoring in high-frequency pressure environments such as shoe soles, oil pumps, and vibration devices. However, this technology heavily depends on high-permittivity metal oxide coatings and complex micro-nano fabrication processes, resulting in high per-device costs ($11.5–55.5/cm²). Additionally, critical issues like synchronous control of multiple droplets remain unresolved, severely limiting its large-scale application.

In contrast, TENGs convert energy through contact electrification and electrostatic induction, offering advantages such as readily available materials, mature fabrication processes, and low manufacturing costs ($0.3–1.3/cm²). They are suitable for large-area preparation and are widely used in contact- and friction-driven wearable textile energy harvesting, droplet and wave impact energy harvesting, as well as self-powered sensors for biological and chemical detection and environmental monitoring. However, their performance is susceptible to humidity, and the durability of friction materials poses a significant challenge to long-term stable operation.

EKEC technology generates potential through fluid shear-induced interfacial charge dragging effects, enabling adaptation to complex fluid environments such as waves, moisture, and evaporation. It shows potential in energy harvesting and self-powered sensing for scenarios involving droplets, waves, and surface wetting. However, its energy conversion efficiency is relatively low (approximately 1–4%, though the theoretical upper limit is around 40%). Additionally, the fabrication of microchannel structures is complex and costly ($16–66/cm²), and the lack of standardized synthesis

pathways and device design processes results in low overall technological maturity and scalability, hindering industrial progress.

From a developmental perspective, in-depth research on interfacial charge transfer mechanisms and the development of novel functional materials will be key to improving the performance metrics of these three technologies. Future studies should focus on addressing industrial bottlenecks such as scalable fabrication processes, environmental stability, and system integration to advance these technologies from the laboratory to practical applications.

Table 2. Comparison among REWOD, TENGs, and EKEC.

Comparison Dimension	REWOD	TENGs	EKEC
Working principle	Capacitance variation induced by droplet deformation through electrowetting	Electrostatic induction and charge transfer triggered by contact-separation.	Flow potential generated by charge dragging induced by fluid shear
Typical output power density	$10^{-3} - \sim100$ W/m² (Theoretical max: $\sim10^4$ W/m²)	$10^{-5} - 160$ W/m²	$10^{-3} - \sim1$ W/m²
Energy conversion efficiency	< 10%	0.01% – 11%	$\sim1\% - 4\%$ (Theoretical max: 40%)
Fabrication cost	Highly dependent on high-dielectric-constant metal oxide coatings, complex micro/nanofabrication, sophisticated electrode manufacturing, and challenging fabrication of enclosed droplet structures, resulting in overall system complexity and high fabrication cost Materials: ~$0.5/cm² Micro/nanofabrication: ~ $10–50/cm² Assembly: ~ $1–5/cm² Total estimated cost: ~ $11.5–55.5/cm²	Mostly utilize low-cost, mature fabrication techniques such as electrospinning, spraying, printing, and textile integration. Materials are easily accessible, processes are simple, suitable for large-area manufacturing with low production cost Materials: ~$0.1/cm² Micro/nanofabrication: ~ $0.1–1/cm² Assembly: ~ $0.2/cm² Total estimated cost: ~ $0.3–1.3/cm²	Relies on precise interfacial control and microchannel/nanopore fabrication. Involves diverse materials, lacks standardized fabrication routes, and presents low overall process maturity, leading to high and difficult-to-control fabrication costs and poor scalability Materials: ~$1/cm² Micro/nanofabrication: ~ $10–50/cm² Assembly: ~ $5–10/cm² Total estimated cost: ~ $16-66/cm²
Applicable scenarios	• Pressure-type wearable energy harvesting (e.g., shoe soles, flexible components) • Pressure-type mechanical motion energy harvesting (e.g., oil pumps, vibration devices) • Self-powered sensors for pressure and motion monitoring	• Contact- and friction-based wearable textile energy harvesting • Droplet and wave impact energy harvesting • Self-powered sensors for biological and chemical composition detection • Self-powered environmental and rainfall alarm sensors	• Energy harvesting from droplets, waves, fluid pipelines, and surface moisture • Self-powered sensors for respiration, humidity variation, and seepage monitoring
Advantages	• High energy density harvesting under high-frequency and strong compression scenarios • High energy conversion potential	• Ultra-low cost • Simple fabrication process • Suitable for large-area textile and friction- • based scenarios • Expandable to hybrid systems for diversified energy harvesting	• Capable of adapting to complex fluid environments such as waves, humidity, and evaporation. • Simple structure • Generate both AC and DC
Disadvantages	• Complex fabrication process with high cost, difficult to achieve mass production • Low power output, highly dependent on complex high-dielectric films and micro/nanofabrication systems • Synchronization and control of multiple droplets is challenging, requiring the development of enclosed multi-droplet microstructures	• Poor long-term durability, prone to wear, contamination, moisture, and corrosion • Poor environmental adaptability, significant reduction in energy output under high temperature and humidity due to electron leakage.	• Low energy conversion efficiency with insufficient understanding of interfacial charge mechanisms • Lack of standardized synthesis and device design processes • Biofouling and surface blockage can accumulate on the device, leading to performance degradation.

Lab on a Chip Accepted Manuscript

107

6. Conclusions

Recent advancements in interfacial EHD-inspired micro/nano-fluidic energy harvesting have showcased the enormous potential of fluid-based approaches particularly REWOD, TENGs, and EKEC. EHD, which explores fluid motion and electric field interactions, offers a versatile approach to liquid-based energy harvesting. Unlike conventional hydropower, EHD-based technologies efficiently capture low-frequency, intermittent mechanical motions and other liquid-associated energy sources like thermally induced flows, evaporation-driven motion, and ionic gradients. In this review, we systematically summarized the fundamental working principles, design considerations, and practical implementations of these diverse technologies, unifying them under an EHD-based energy-harvesting framework. By highlighting key breakthroughs such as multi-droplet REWOD architecture, robust new triboelectric materials, and advanced microchannel engineering, we demonstrate how these emerging strategies collectively broaden opportunities for harvesting energy from sources ranging from raindrops, ocean waves to human motion and ambient fluids.

Despite these promising developments, several challenges persist. As detailed in the preceding sections, scaling up the output power of REWOD requires precise synchronization and control of multiple droplets. Similarly, long-term stability, environmental adaptability, and methods to continuously boost energy output are the main challenges faced in TENG and need further development. And in electrokinetic systems, challenges such as limited atomic-level characterization, energy conversion inefficiencies, and durability concerns continue to hinder large-scale implementation. Moreover, some technologies demand costly materials, complicated fabrication processes or specialized coatings for surface modifications, complicating large-scale manufacturing and commercial uptake. Achieving higher output power and stable performance under variable environmental factors such as salinity, fluid velocity, or pH requires deeper insight into interfacial physics and material optimization. Additionally, integrating these energy harvesters with on-chip signal conditioning, energy storage, and wireless communication modules poses a key engineering challenge on the path to fully autonomous systems.

Moving forward, research should focus on optimizing device architectures to maximize power density while preserving mechanical flexibility, biocompatibility, and environmental resilience. Novel functional materials such as bioinspired self-healing

polymers or hybrid nanocomposites could address durability concerns, while scalable fabrication methods (e.g., roll-to-roll or 3D printing) may reduce production costs and complexity. Beyond the laboratory, the synergy of interfacial EHD-based harvesters with advanced computing, machine learning, and internet IoT platforms can unlock transformative solutions for wearable health monitoring, environmental sensing, and industrial automation. With continued innovation and interdisciplinary collaboration, these fluidic energy-harvesting technologies are poised to transition from proof-of-concept demonstrations to market-ready devices, offering sustainable, decentralized power sources that address real-world energy challenges.

Author Contributions

Lingxuan Hao, Mohammed Imran Khan, and Yilin Lei contributed equally to this work and share first authorship. Their contributions include conceptualization, literature review, and manuscript preparation. Shuneng Zhou assisted in abstract formulation and provided critical feedback. Bei Fan supervised the project, reviewed drafts, provided intellectual insights, and revised the manuscript.

Conflicts of Interests

The authors declare no conflict of interest.

Acknowledgements

ORCID

Mohammed Imran Khan: https://orcid.org/0000-0002-5689-335X

Yilin Lei: https://orcid.org/0000-0001-7890-0373

Lingxuan Hao: https://orcid.org/0000-0001-6202-6060

References

1   F. Wen and C. Lee, Droplet, 2024, 3, e133.

2   D. Shen, W. W. Duley, P. Peng, M. Xiao, J. Feng, L. Liu, G. Zou and Y. N. Zhou, Adv. Mater., 2020, 32, 2003722.

3   D. Singh, G. Bhutani, S. Sharma and R. Kumar, in Emerging Trends in Energy Conversion and Thermo-Fluid Systems, eds. D. Sharma and S. Roy, Springer Nature, Singapore, 2023, pp. 3–16.

Lab on a Chip Accepted Manuscript

4   U. Latif, E. Uddin, M. Y. Younis, J. Aslam, Z. Ali, M. Sajid and A. Abdelkefi, Energy, 2021, 215, 119195.

5   G. L. Stephens, M. Z. Hakuba, M. Hawcroft, J. M. Haywood, A. Behrangi, J. E. Kay and P. J. Webster, Curr. Clim. Change Rep., 2016, 2, 135–147.

6   M. Mariello, F. Guido, V. M. Mastronardi, M. T. Todaro, D. Desmaële and M. De Vittorio, Nano Energy, 2019, 57, 141–156.

7   L. Ren, C.-J. Kim and Z. Wang, Droplet, 2022, 1, 1–1.

8   Y. Song, W. Xu, Y. Liu, H. Zheng, M. Cui, Y. Zhou, B. Zhang, X. Yan, L. Wang and P. Li, The innovation.

9   S. Chu and A. Majumdar, nature, 2012, 488, 294–303.

10   J. Tu, J. Shi, L. Chen, J. Liu, C. Li and J. Wei, Int. J. Heat Mass Transf., 2022, 199, 123481.

11   N. Wang, M. Zhao, Y. Lei and J. Liang, IOP Conf. Ser. Mater. Sci. Eng., 2024, 1301, 012001.

12   S. Zhao, G. Wang, L. Wei, Q. Wu, Z. Pan, Y. Lei, M. Zheng, M. Xia and J. Liang, IOP Conf. Ser. Mater. Sci. Eng., 2024, 1301, 012149.

13   B. W. An, J. H. Shin, S.-Y. Kim, J. Kim, S. Ji, J. Park, Y. Lee, J. Jang, Y.-G. Park and E. Cho, Polymers, 2017, 9, 303.

14   M. Ha, S. Lim and H. Ko, J. Mater. Chem. B, 2018, 6, 4043–4064.

15   A. Darwish and A. E. Hassanien, Sensors, 2011, 11, 5561–5595.

16   W. Zhang, Y. Zhang, G. Yang, X. Hao, X. Lv, F. Wu, J. Liu and Y. Zhang, Nano Energy, 2021, 82, 105769.

17   M. Stoppa and A. Chiolerio, sensors, 2014, 14, 11957–11992.

18   S. Chen, Z. Qiao, Y. Niu, J. C. Yeo, Y. Liu, J. Qi, S. Fan, X. Liu, J. Y. Lee and C. T. Lim, Nat. Rev. Bioeng., 2023, 1, 950–971.

19   C. Yang, X. Gan, Y. Zeng, Z. Xu, L. Xu, C. Hu, H. Ma, B. Chai, S. Hu and Y. Chai, Biosens. Bioelectron., 2023, 242, 115723.

20   A. Ainla, M. M. Hamedi, F. Güder and G. M. Whitesides, Adv. Mater., 2017, 29, 1702894.

21   Y. Yang, X. Guo, M. Zhu, Z. Sun, Z. Zhang, T. He and C. Lee, Adv. Energy Mater., 2023, 13, 2203040.

22   M. Huang, M. Zhu, X. Feng, Z. Zhang, T. Tang, X. Guo, T. Chen, H. Liu, L. Sun and C. Lee, ACS Nano, 2023, 17, 6435–6451.

23 L. Liu, Q. Shi and C. Lee, Nano Energy, 2020, 76, 105052.

24 A. Goswami and P. Sen, in Nanomaterials for Green Energy, Elsevier, 2018, pp. 113–143.

25 E. D. Fylladitakis, M. P. Theodoridis and A. X. Moronis, IEEE Trans. Plasma Sci., 2014, 42, 358–375.

26 N. T. Tasneem, D. K. Biswas, P. R. Adhikari, R. Reid and I. Mahbub, in 2020 IEEE International Symposium on Circuits and Systems (ISCAS), IEEE, 2020, pp. 1–5.

27 K. Liu, Y. Zhou, F. Yuan, X. Mo, P. Yang, Q. Chen, J. Li, T. Ding and J. Zhou, Angew. Chem. Int. Ed., 2016, 55, 15864–15868.

28 X. Zhang, Y. Zheng, D. Wang and F. Zhou, Nano Energy, 2017, 40, 95–106.

29 J. Nie, Z. Wang, Z. Ren, S. Li, X. Chen and Z. Lin Wang, Nat. Commun., 2019, 10, 2264.

30 H. Li, X. Li, X. Li, C. Chong, J. Jin, Z. Wu, H. Wang, J. Huang, J. Han and H. K. Lee, Chem. Eng. J., 2023, 461, 142083.

31 R. Zhang, S. Wang, M.-H. Yeh, C. Pan, L. Lin, R. Yu, Y. Zhang, L. Zheng, Z. Jiao and Z. L. Wang, Adv. Mater., 2015, 27, 6482–6487.

32 C. Quilliet and B. Berge, Curr. Opin. Colloid Interface Sci., 2001, 6, 34–39.

33 F. Mugele, M. Duits and D. Van den Ende, Adv. Colloid Interface Sci., 2010, 161, 115–123.

34 T. Krupenkin and J. A. Taylor, Nat. Commun., 2011, 2, 448.

35 J. K. Moon, J. Jeong, D. Lee and H. K. Pak, Nat. Commun., 2013, 4, 1487.

36 H. Yang, H. Lee, Y. Lim, M. Christy and Y.-B. Kim, Int. J. Precis. Eng. Manuf.-Green Technol., 2021, 8, 103–111.

37 D. Choi, Y. Lee, Z.-H. Lin, S. Cho, M. Kim, C. K. Ao, S. Soh, C. Sohn, C. K. Jeong, J. Lee, M. Lee, S. Lee, J. Ryu, P. Parashar, Y. Cho, J. Ahn, I.-D. Kim, F. Jiang, P. S. Lee, G. Khandelwal, S.-J. Kim, H. S. Kim, H.-C. Song, M. Kim, J. Nah, W. Kim, H. G. Menge, Y. T. Park, W. Xu, J. Hao, H. Park, J.-H. Lee, D.-M. Lee, S.-W. Kim, J. Y. Park, H. Zhang, Y. Zi, R. Guo, J. Cheng, Z. Yang, Y. Xie, S. Lee, J. Chung, I.-K. Oh, J.-S. Kim, T. Cheng, Q. Gao, G. Cheng, G. Gu, M. Shim, J. Jung, C. Yun, C. Zhang, G. Liu, Y. Chen, S. Kim, X. Chen, J. Hu, X. Pu, Z. H. Guo, X. Wang, J. Chen, X. Xiao, X. Xie, M. Jarin, H. Zhang, Y.-C. Lai, T. He, H. Kim, I. Park, J. Ahn, N. D. Huynh, Y. Yang, Z. L. Wang, J. M. Baik and D. Choi, ACS Nano, 2023, 17, 11087–11219.

38 X. Cui, J. Nie and Y. Zhang, Int. J. Extreme Manuf., 2024, 6, 042001.

39   M. S. Iqbal, H. Lu, S. Khaladkar, X. Wu, S. Roy, Z. Ullah, Y. Yan, Y. Zhang and B. Guo, Mater. Today Energy, 2024, 46, 101732.

40   C. Davidson and X. Xuan, J. Power Sources, 2008, 179, 297–300.

41   C. Bakli and S. Chakraborty, ELECTROPHORESIS, 2015, 36, 675–681.

42   C. L. A. Berli, J. Colloid Interface Sci., 2010, 349, 446–448.

43   C. Li, K. Liu, H. Liu, B. Yang and X. Hu, Mater. Res. Bull., 2017, 90, 81–86.

44   K. Kakaraparty, G. S. Hyer, E. A. Pineda, R. C. Reid and I. Mahbub, in 2022 IEEE Sensors, IEEE, 2022, pp. 1–4.

45   B. S. Schumacher, P. K. Sah, K. Kakaraparty, I. Mahbub and R. C. Reid, IEEE Sens. J.

46   P. R. Adhikari, M. N. Islam, Y. Jiang, R. C. Reid and I. Mahbub, IEEE Sens. Lett., 2022, 6, 1–4.

47   S. D. Psoma, I. Sobianin and A. Tourlidakis, in Proceedings, MDPI, 2024, vol. 97, p. 200.

48   P. R. Adhikari, A. B. Patwary, K. Kakaraparty, A. Gunti, R. C. Reid and I. Mahbub, Energy Technol., 2022, 10, 2100867.

49   T.-H. Hsu, J. A. Taylor and T. N. Krupenkin, Faraday Discuss., 2017, 199, 377–392.

50   C. Ye, D. Liu, P. Chen, L. N. Y. Cao, X. Li, T. Jiang and Z. L. Wang, Adv. Mater., 2023, 35, 2209713.

51   Z. L. Wang, T. Jiang and L. Xu, Nano Energy, 2017, 39, 9–23.

52   J. Chen, J. Yang, Z. Li, X. Fan, Y. Zi, Q. Jing, H. Guo, Z. Wen, K. C. Pradel, S. Niu and Z. L. Wang, ACS Nano, 2015, 9, 3324–3331.

53   J. H. Ahn, J. Y. Hwang, C. G. Kim, G. H. Nam and K. K. Ahn, Nano Energy, 2020, 67, 104269.

54   Y. Zhong, Y. Guo, X. Wei, P. Rui, H. Du and P. Wang, Nano Energy, 2021, 89, 106467.

55   X. Gao, G. Zhao, Y. Zhang, Y. Zhang and Z. Wang, Eur. Phys. J. Plus, 2024, 139, 788.

56   Z. Ding, K. Tian and Y. Jian, Appl. Math. Mech., 2022, 43, 1289–1306.

57   Y. (张越) Zhang, G. (赵光普) Zhao, Y. (侯雅馨) Hou, J. (张佳莉) Zhang and B. (薛博) Xue, Phys. Fluids, 2024, 36, 093106.

58 Y. Lei, G. Hong, Y. Zhao, R. Li, J. Quan and J. Liang, Cryogenics, 2023, 132, 103687.

59 J. Zhang, K. Zhan, S. Wang and X. Hou, Soft Matter, 2020, 16, 2915–2927.

60 D. Xu, M. Yan and Y. Xie, ELECTROPHORESIS, 2024, 45, 244–265.

61 C.-C. Chang, Nanomaterials, 2022, 12, 1100.

62 N. Yanagisawa, V. Dominguez, S. Mahmud and D. Dutta, Phys. Fluids, 2023, 35, 053604.

63 D. Burgreen and F. R. Nakache, J. Appl. Mech., 1965, 32, 675–679.

64 B. Nie, S. Xing, J. D. Brandt and T. Pan, Lab. Chip, 2012, 12, 1110–1118.

65 N. T. Tasneem, D. K. Biswas, I. Mahbub, P. R. Adhikari and R. Reid, in 2021 IEEE International Symposium on Circuits and Systems (ISCAS), IEEE, 2021, pp. 1–5.

66 P. R. Adhikari, N. T. Tasneem, D. K. Biswas, R. C. Reid and I. Mahbub, in ASME International Mechanical Engineering Congress and Exposition, American Society of Mechanical Engineers, 2020, vol. 84560, p. V008T08A035.

67 N. Zhang, C. Tao, X. Fan and J. Chen, J. Mater. Res., 2017, 32, 1628–1646.

68 S. Wang, Y. Wang, D. Liu, Z. Zhang, W. Li, C. Liu, T. Du, X. Xiao, L. Song, H. Pang and M. Xu, Sens. Actuators Phys., 2021, 317, 112459.

69 Y. Song, J. Min, Y. Yu, H. Wang, Y. Yang, H. Zhang and W. Gao, Sci. Adv., 2020, 6, eaay9842.

70 H. Helmholtz, Ann. Phys., 1879, 243, 337–382.

71 M. Gouy, J. Phys. Théorique Appliquée, 1910, 9, 457–468.

72 D. L. Chapman, Lond. Edinb. Dublin Philos. Mag. J. Sci., 1913, 25, 475–481.

73 O. Stern, Z. Für Elektrochem. Angew. Phys. Chem., 1924, 30, 508–516.

74 A. J. Bard, L. R. Faulkner and H. S. White, Electrochemical methods: fundamentals and applications, John Wiley & Sons, 2022.

75 J. N. Israelachvili, Intermolecular and surface forces, Academic press, 2011.

76 D. C. Grahame, Chem. Rev., 1947, 41, 441–501.

77 R. Parsons, Chem. Rev., 1990, 90, 813–826.

78 R. B. Schoch, J. Han and P. Renaud, Rev. Mod. Phys., 2008, 80, 839–883.

79 Q. Deyang and S. Hang, J. Power Sources.

80 P. Sharma and T. S. Bhatti, Energy Convers. Manag., 2010, 51, 2901–2912.

81 P. Simon and Y. Gogotsi, Nat. Mater., 2008, 7, 845–854.

Lab on a Chip Accepted Manuscript

82   J. H. Masliyah and S. Bhattacharjee, Electrokinetic and Colloid Transport Phenomena, John Wiley & Sons, 2006.

83   G. Lippmann, Ann Chim Phys, 1875, 5, 494–549.

84   F. Mugele and J.-C. Baret, J. Phys. Condens. Matter, 2005, 17, R705.

85   Y.-P. Zhao and Y. Wang, Rev. Adhes. Adhes., 2013, 1, 114–174.

86   B. Berge, Comptes Rendus Acad. Sci. Ser. Ii, 1993, 317, 157–163.

87   J. A. M. Sondag-Huethorst and L. G. J. Fokkink, Langmuir, 1994, 10, 4380–4387.

88   W. J. J. Welters and L. G. J. Fokkink, Langmuir, 1998, 14, 1535–1538.

89   D. Singh, G. Bhutani, S. Sharma and R. Kumar, in iCONECTS 2021, eds. D. Sharma and S. Roy, Springer, Singapore, Singapore, 2023, pp. 3–16.

90   W. Xu, H. Zheng, Y. Liu, X. Zhou, C. Zhang, Y. Song, X. Deng, M. Leung, Z. Yang, R. X. Xu, Z. L. Wang, X. C. Zeng and Z. Wang, Nature, 2020, 578, 392–396.

91   J. Tan, S. Sun, D. Jiang, M. Xu, X. Chen, Y. Song and Z. L. Wang, Mater. Today, 2022, 58, 201–220.

92   P. Gu, S. Yang, X. Liu and G. Yang, Soil Sci. Soc. Am. J., 2020, 84, 494–501.

93   P. Gaddam and W. Ducker, Langmuir, 2019, 35, 5719–5727.

94   S. Berry, J. Kedzierski and B. Abedian, J. Colloid Interface Sci., 2006, 303, 517–524.

95   F. Mugele, M. Duits and D. Van den Ende, Adv. Colloid Interface Sci., 2010, 161, 115–123.

96   F. Invernizzi, S. Dulio, M. Patrini, G. Guizzetti and P. Mustarelli, Chem. Soc. Rev., 2016, 45, 5455–5473.

97   P. G. De Gennes, Rev. Mod. Phys., 1985, 57, 827–863.

98   P. R. Adhikari, R. C. Reid and I. Mahbub, J. Power Sources, 2022, 517, 230726.

99   P. R. Adhikari, N. T. Tasneem, R. C. Reid and I. Mahbub, Sci. Rep., 2021, 11, 5030.

100 H. Yang, S. Hong, B. Koo, D. Lee and Y.-B. Kim, Nano Energy, 2017, 31, 450–455.

101 T.-H. Hsu, S. Manakasettharn, J. A. Taylor and T. Krupenkin, Sci. Rep., 2015, 5, 16537.

102 J. Drelich, J. D. Miller and R. J. Good, J. Colloid Interface Sci., 1996, 179, 37–50.

103 P. R. Adhikari, D. K. Biswas, N. T. Tasneem, R. C. Reid and I. Mahbub, in Energy Harvesting and Storage: Materials, Devices, and Applications XI, SPIE, 2021, vol. 11722, pp. 63–73.

104 Z. Wan, H. Zeng and A. Feinerman, .

105 P. Sen and C.-J. Kim, J. Microelectromechanical Syst., 2008, 18, 174–185.

106 N. Novkovski, A. Skeparovski and E. Atanassova, J. Phys. Appl. Phys., 2008, 41, 105302.

107 Y.-Y. Lin, R. D. Evans, E. Welch, B.-N. Hsu, A. C. Madison and R. B. Fair, Sens. Actuators B Chem., 2010, 150, 465–470.

108 M. K. Kilaru, J. Heikenfeld, G. Lin and J. E. Mark, Appl. Phys. Lett.

109 J. An, T. Usui, M. Logar, J. Park, D. Thian, S. Kim, K. Kim and F. B. Prinz, ACS Appl. Mater. Interfaces, 2014, 6, 10656–10660.

110 J. Kolodzey, E. A. Chowdhury, T. N. Adam, G. Qui, I. Rau, J. O. Olowolafe, J. S. Suehle and Y. Chen, IEEE Trans. Electron Devices, 2000, 47, 121–128.

111 S. Nawaz and C. Mascolo, in Proceedings of the 12th ACM Conference on Embedded Network Sensor Systems, ACM, Memphis Tennessee, 2014, pp. 236–250.

112 M. Youssef, M. A. Yosef and M. El-Derini, in 2010 IEEE Global Telecommunications Conference GLOBECOM 2010, IEEE, 2010, pp. 1–5.

113 J. Zhao, R. Ghannam, K. O. Htet, Y. Liu, M. Law, V. A. L. Roy, B. Michel, M. A. Imran and H. Heidari, Adv. Healthc. Mater., 2020, 9, 2000779.

114 A. Ben Amar, A. B. Kouki and H. Cao, sensors, 2015, 15, 28889–28914.

115 J. B. Reswick and L. Vodovnik, Artif. Limbs, 1967, 11, 5–21.

116 A. Carroll and G. Heiser, in 2010 USENIX Annual Technical Conference (USENIX ATC 10), 2010.

117 S. Tarkoma, Smartphone energy consumption: modeling and optimization, Cambridge University Press, 2014.

118 C. V. Vasile, C. Pattinson and A.-L. Kor, in Green IT Engineering: Social, Business and Industrial Applications, eds. V. Kharchenko, Y. Kondratenko and J. Kacprzyk, Springer International Publishing, Cham, 2019, vol. 171, pp. 243–271.

119 R. Piyare, A. L. Murphy, C. Kiraly, P. Tosato and D. Brunelli, IEEE Commun. Surv. Tutor., 2017, 19, 2117–2157.

120 L. M. Larsen, H. L. Christiansen, S. Ruepp and M. S. Berger, IEEE Open J. Commun. Soc., 2023, 4, 768–797.

View Article Online
DOI: 10.1039/D5LC00321K

121 J. Baliga, R. Ayre, K. Hinton and R. S. Tucker, IEEE Commun. Mag., 2011, 49, 70–77.

122 K. Kakaraparty, E. A. Pineda, B. Schumacher, R. C. Reid and I. Mahbub, IEEE Sens. J.

123 P. D. Mitcheson, E. M. Yeatman, G. K. Rao, A. S. Holmes and T. C. Green, Proc. IEEE, 2008, 96, 1457–1486.

124 J. A. Paradiso and T. Starner, IEEE Pervasive Comput., 2005, 4, 18–27.

125 N. S. Shenck and J. A. Paradiso, IEEE Micro, 2001, 21, 30–42.

126 T. Starner, IBM Syst. J., 1996, 35, 618–629.

127 K. Kakaraparty, E. A. Pineda, R. C. Reid and I. Mahbub, IEEE Sens. J., 2023, 23, 10334–10341.

128 S. C. Chandrarathna and J.-W. Lee, IEEE Trans. Biomed. Circuits Syst., 2020, 15, 55–67.

129 P. K. Sah, E. P. Alvarez, K. Kakaraparty, R. C. Reid and I. Mahbub, in 2024 IEEE 67th International Midwest Symposium on Circuits and Systems (MWSCAS), IEEE, 2024, pp. 1046–1050.

130 A. Moyo, M. W. Shahzad, J. Terry, Y. Mita and Y. Li, in 2022 IEEE Sensors, IEEE, 2022, pp. 1–5.

131 C. Hou, H. Wang, Q. Zhang, Y. Li and M. Zhu, Adv. Mater. Deerfield Beach Fla, 2014, 26, 5018–5024.

132 X. Liao, Q. Liao, X. Yan, Q. Liang, H. Si, M. Li, H. Wu, S. Cao and Y. Zhang, Adv. Funct. Mater., 2015, 25, 2395–2401.

133 X. Xiao, L. Yuan, J. Zhong, T. Ding, Y. Liu, Z. Cai, Y. Rong, H. Han, J. Zhou and Z. L. Wang, Adv. Mater., 2011, 23, 5440–5444.

134 D. P. Cotton, I. M. Graz and S. P. Lacour, IEEE Sens. J., 2009, 9, 2008–2009.

135 H. Athenstaedt, H. Claussen and D. Schaper, Science, 1982, 216, 1018–1020.

136 Q. Zhong, J. Zhong, X. Cheng, X. Yao, B. Wang, W. Li, N. Wu, K. Liu, B. Hu and J. Zhou, Adv. Mater., 2015, 27, 7130–7136.

137 J. Zhou, Y. Gu, P. Fei, W. Mai, Y. Gao, R. Yang, G. Bao and Z. L. Wang, Nano Lett., 2008, 8, 3035–3040.

138 Y. Yang, Z.-H. Lin, T. Hou, F. Zhang and Z. L. Wang, Nano Res., 2012, 5, 888–895.

139 T. Someya, T. Sekitani, S. Iba, Y. Kato, H. Kawaguchi and T. Sakurai, Proc. Natl. Acad. Sci., 2004, 101, 9966–9970.

140 C. Wang, D. Hwang, Z. Yu, K. Takei, J. Park, T. Chen, B. Ma and A. Javey, Nat. Mater., 2013, 12, 899–904.

141 R. C. Webb, A. P. Bonifas, A. Behnaz, Y. Zhang, K. J. Yu, H. Cheng, M. Shi, Z. Bian, Z. Liu and Y.-S. Kim, Nat. Mater., 2013, 12, 938–944.

142 G. Schwartz, B. C.-K. Tee, J. Mei, A. L. Appleton, D. H. Kim, H. Wang and Z. Bao, Nat. Commun., 2013, 4, 1859.

143 J. Zhong, Q. Zhong, Q. Hu, N. Wu, W. Li, B. Wang, B. Hu and J. Zhou, Adv. Funct. Mater., 2015, 25, 1798–1803.

144 I. Graz, M. Krause, S. Bauer-Gogonea, S. Bauer, S. P. Lacour, B. Ploss, M. Zirkl, B. Stadlober and S. Wagner, J. Appl. Phys.

145 C. Li, P.-M. Wu, L. A. Shutter and R. K. Narayan, Appl. Phys. Lett.

146 T. Someya, Y. Kato, T. Sekitani, S. Iba, Y. Noguchi, Y. Murase, H. Kawaguchi and T. Sakurai, Proc. Natl. Acad. Sci., 2005, 102, 12321–12325.

147 N. T. Tien, S. Jeon, D. Kim, T. Q. Trung, M. Jang, B. Hwang, K. Byun, J. Bae, E. Lee, J. B. -H. Tok, Z. Bao, N. Lee and J. Park, Adv. Mater., 2014, 26, 796–804.

148 F. Zhang, Y. Zang, D. Huang, C. Di and D. Zhu, Nature Communications, 2013, 26, 796–804.

149 A. Moyo, M. W. Shahzad, S. Smith, J. Terry, Y. Mita, J. Lewis and Y. Li, in 2024 IEEE 36th International Conference on Microelectronic Test Structures (ICMTS), IEEE, 2024, pp. 1–5.

150 S.-Y. Teh, R. Lin, L.-H. Hung and A. P. Lee, Lab on a Chip, 2008, 8, 198–220.

151 G. Carraro, S. Passaglia, G. Paolini, G. Bracco, L. Savio, G. Luciano, L. Vattuone, R. Masini and M. Smerieri, Appl. Surf. Sci., 2023, 611, 155522.

152 R. Rusev, G. Angelov, K. Angelov and D. Nikolov, in 2017 XXVI International Scientific Conference Electronics (ET), IEEE, 2017, pp. 1–4.

153 F. Fan, Z. Tian and Z. L. Wang, Nano Energy, 2012, 1, 328–334.

154 S. Roy Barman, Y.-J. Lin, K.-M. Lee, A. Pal, N. Tiwari, S. Lee and Z.-H. Lin, ACS Nano, 2023, 17, 2689–2701.

155 T. Huang, W. Sun, L. Liao, K. Zhang, M. Lu, L. Jiang, S. Chen and A. Qin, ACS Appl. Mater. Interfaces, 2023, 15, 35014–35023.

156 P. Jiang, L. Zhang, H. Guo, C. Chen, C. Wu, S. Zhang and Z. L. Wang, Adv. Mater., 2019, 31, 1902793.

157 R. Zhang, H. Lin, Y. Pan, C. Li, Z. Yang, J. Tian and H. C. Shum, Adv. Funct. Mater., 2022, 32, 2208393.

158 S. Zhang, M. Chi, J. Mo, T. Liu, Y. Liu, Q. Fu, J. Wang, B. Luo, Y. Qin, S. Wang and S. Nie, Nat. Commun., 2022, 13, 4168.

159 C. Xu, X. Fu, C. Li, G. Liu, Y. Gao, Y. Qi, T. Bu, Y. Chen, Z. L. Wang and C. Zhang, Microsyst. Nanoeng., 2022, 8, 1–9.

160 Z. Wang, W. Liu, W. He, H. Guo, L. Long, Y. Xi, X. Wang, A. Liu and C. Hu, Joule, 2021, 5, 441–455.

161 Y. Zeng, H. Xiang, N. Zheng, X. Cao, N. Wang and Z. L. Wang, Nano Energy, 2022, 91, 106601.

162 Y. Wang, A. T. T. Pham, X. Han, D. Du and Y. Tang, Nano Energy, 2022, 93, 106844.

163 G. Yu, J. Wen, H. Li, Y. Shang, Z. L. Wang and B. Chen, Nano Energy, 2024, 119, 109062.

164 Z. L. Wang, Mater. Today, 2017, 20, 74–82.

165 Z. L. Wang, Nano Energy, 2020, 68, 104272.

166 Z. L. Wang, in Handbook of Triboelectric Nanogenerators, eds. Z. L. Wang, Y. Yang, J. Zhai and J. Wang, Springer International Publishing, Cham, 2023, pp. 3–32.

167 H. Zhai, S. Ding, X. Chen, Y. Wu and Z. Lin Wang, Mater. Today, 2023, 65, 166–188.

168 G. Qiao, J. Wang, X. Yu, R. Jia, T. Cheng and Z. L. Wang, Nano Energy, 2021, 79, 105408.

169 G. Min, Y. Xu, P. Cochran, N. Gadegaard, D. M. Mulvihill and R. Dahiya, Nano Energy, 2021, 83, 105829.

170 Y. Zou, J. Xu, K. Chen and J. Chen, Adv. Mater. Technol., 2021, 6, 2000916.

171 V. Nguyen and R. Yang, Nano Energy, 2013, 2, 604–608.

172 J. Fu, X. Xia, G. Xu, X. Li and Y. Zi, ACS Nano, 2019, 13, 13257–13263.

173 J. Fu, G. Xu, C. Li, X. Xia, D. Guan, J. Li, Z. Huang and Y. Zi, Adv. Sci., 2020, 7, 2001757.

174 X. Xia, J. Fu and Y. Zi, Nat. Commun., 2019, 10, 4428.

175 W. Tang, T. Jiang, F. R. Fan, A. F. Yu, C. Zhang, X. Cao and Z. L. Wang, Adv. Funct. Mater., 2015, 25, 3718–3725.

176 S. Chatterjee, S. R. Burman, I. Khan, S. Saha, D. Choi, S. Lee and Z.-H. Lin, Nanoscale, 2020, 12, 17663–17697.

177 Y. Chen, B. Xie, J. Long, Y. Kuang, X. Chen, M. Hou, J. Gao, S. Zhou, B. Fan, Y. He, Y.-T. Zhang, C.-P. Wong, Z. Wang and N. Zhao, Adv. Mater., 2021, 33, 2104290.

178 Y. Dong, S. Xu, C. Zhang, L. Zhang, D. Wang, Y. Xie, N. Luo, Y. Feng, N. Wang, M. Feng, X. Zhang, F. Zhou and Z. L. Wang, Sci. Adv., 2022, 8, eadd0464.

179 Y. Dong, M. Feng, J. Cheng, S. Chang, D. Wang and W. Lu, Nano Energy, 2024, 119, 109083.

180 J. Fu, G. Xu, H. Wu, C. Li and Y. Zi, Adv. Energy Sustain. Res., 2022, 3, 2200051.

181 Z. L. Wang, Faraday Discuss., 2015, 176, 447–458.

182 Z.-H. Lin, G. Cheng, L. Lin, S. Lee and Z. L. Wang, Angew. Chem. Int. Ed., 2013, 52, 12545–12549.

183 Y. Lu, L. Jiang, Y. Yu, D. Wang, W. Sun, Y. Liu, J. Yu, J. Zhang, K. Wang, H. Hu, X. Wang, Q. Ma and X. Wang, Nat. Commun., 2022, 13, 5316.

184 H. Deng, Z. Zhao, C. Jiao, J. Ye, S. Zhao, M. Ma and X. Zhong, Front. Mater., DOI:10.3389/fmats.2021.692273.

185 X. Liang, S. Liu, S. Lin, H. Yang, T. Jiang and Z. L. Wang, Adv. Energy Mater., 2023, 13, 2300571.

186 S. Hu, Z. Shi, R. Zheng, W. Ye, X. Gao, W. Zhao and G. Yang, ACS Appl. Mater. Interfaces, 2020, 12, 40021–40030.

187 J.-W. Lee and W. Hwang, Nano Energy, 2018, 52, 315–322.

188 S. A. Nahian, R. K. Cheedarala and K. K. Ahn, Nano Energy, 2017, 38, 447–456.

189 Z.-H. Lin, G. Cheng, S. Lee, K. C. Pradel and Z. L. Wang, Adv. Mater., 2014, 26, 4690–4696.

190 M. Han, B. Yu, G. Qiu, H. Chen, Z. Su, M. Shi, B. Meng, X. Cheng and H. Zhang, J. Mater. Chem. A, 2015, 3, 7382–7388.

191 W. Zhang, P. Wang, K. Sun, C. Wang and D. Diao, Nano Energy, 2019, 56, 277–285.

192 S. Wang, Y. Xie, S. Niu, L. Lin and Z. L. Wang, Adv. Mater., 2014, 26, 2818–2824.

193 S.-H. Kwon, J. Park, W. K. Kim, Y. Yang, E. Lee, C. J. Han, S. Y. Park, J. Lee and Y. S. Kim, Energy Environ. Sci., 2014, 7, 3279–3283.

194 H. Hong, T. Chen, J. Yang, Y. Hu, J. Hu, D. Li, F. Liu, L. Liu and H. Wu, Cell Rep. Phys. Sci., 2024, 5, 101933.

195 L. N. Y. Cao, Z. Xu and Z. L. Wang, Nanomaterials, 2022, 12, 3261.

196 X. Li, J. Tao, X. Wang, J. Zhu, C. Pan and Z. L. Wang, Adv. Energy Mater., 2018, 8, 1800705.

197 G. Cheng, T. Zhang, X. Fu, J. Hua, W. Dai, J. Cao, W. Sun and J. Ding, Adv. Mater. Technol., 2024, 9, 2301588.

198 W. Xu, X. Li, J. Brugger and X. Liu, Nano Energy, 2022, 98, 107166.

199 C. Xu, Y. Zi, A. C. Wang, H. Zou, Y. Dai, X. He, P. Wang, Y.-C. Wang, P. Feng, D. Li and Z. L. Wang, Adv. Mater., 2018, 30, 1706790.

200 M. Sun, Q. Lu, Z. L. Wang and B. Huang, Nat. Commun., 2021, 12, 1752.

201 Y. Nan, J. Shao, M. Willatzen and Z. L. Wang, Research, DOI:10.34133/2022/9861463.

202 L. Li, X. Wang, P. Zhu, H. Li, F. Wang and J. Wu, Nano Energy, 2020, 70, 104476.

203 J. Le, Q. Fan, L. Perez-Martinez, A. Cuesta and J. Cheng, Phys. Chem. Chem. Phys., 2018, 20, 11554–11558.

204 G. Trefalt, S. H. Behrens and M. Borkovec, Langmuir, 2016, 32, 380–400.

205 S. Lin, X. Chen and Z. L. Wang, Chem. Rev., 2022, 122, 5209–5232.

206 J. Nie, Z. Ren, L. Xu, S. Lin, F. Zhan, X. Chen and Z. L. Wang, Adv. Mater., 2020, 32, 1905696.

207 Z. L. Wang and A. C. Wang, Mater. Today, 2019, 30, 34–51.

208 D. Yoo, S. Jang, S. Cho, D. Choi and D. S. Kim, Adv. Mater., 2023, 35, 2300699.

209 L. Zhang, X. Li, Y. Zhang, Y. Feng, F. Zhou and D. Wang, Nano Energy, 2020, 78, 105370.

210 S. Lin, X. Chen and Z. L. Wang, Nano Energy, 2020, 76, 105070.

211 S. Lin, L. Xu, A. Chi Wang and Z. L. Wang, Nat. Commun., 2020, 11, 399.

212 Y. Wang, S. Gao, W. Xu and Z. Wang, Adv. Funct. Mater., 2020, 30, 1908252.

213 H. Wu, N. Mendel, D. Van Den Ende, G. Zhou and F. Mugele, Phys. Rev. Lett., 2020, 125, 078301.

214 H. Wu, N. Mendel, S. van der Ham, L. Shui, G. Zhou and F. Mugele, Adv. Mater., 2020, 32, 2001699.

215 W. Xu, Q. Chen, Q. Ren, J. Li, Q. Chen, C. Zhu, Y. Xie and W. Li, Nano Energy, 2024, 131, 110191.

216 J. Peng, S. D. Kang and G. J. Snyder, Sci. Adv., 2017, 3, eaap8576.

217 S. Jang, M. La, S. Cho, Y. Yun, J. H. Choi, Y. Ra, S. J. Park and D. Choi, Nano Energy, 2020, 70, 104541.

218 S. Lin, M. Zheng, J. Luo and Z. L. Wang, ACS Nano, 2020, 14, 10733–10741.

219 H. Zhang, K. Yin, L. Wang, Q. Deng, Y. He, Z. Xiao, G. Li and G. Dai, ACS Appl. Mater. Interfaces, 2023, 15, 30902–30912.

220 L. Wang, Y. Song, W. Xu, W. Li, Y. Jin, S. Gao, S. Yang, C. Wu, S. Wang and Z. Wang, EcoMat, 2021, 3, e12116.

221 W. Xu, X. Zhou, C. Hao, H. Zheng, Y. Liu, X. Yan, Z. Yang, M. Leung, X. C. Zeng, R. X. Xu and Z. Wang, Natl. Sci. Rev., 2019, 6, 540–550.

222 P. Wu, P. Yang, Z. Liu, G. Huang, X. Tao, S. Qin, X. Dong, L. Zheng, H. Li, X. Chen and Z. L. Wang, Adv. Energy Mater., 2024, 14, 2303912.

223 X. Chen, Y. Zhao, F. Wang, D. Tong, L. Gao, D. Li, L. Wu, X. Mu and Y. Yang, Adv. Sci., 2022, 9, 2103957.

224 W. Shao, T. Lin, W. Liu, J. Groenewold, B. Tang, J. Gao and G. Zhou, Adv. Funct. Mater., 2023, 33, 2302472.

225 J. Lowell and A. C. and Rose-Innes, Adv. Phys., 1980, 29, 947–1023.

226 S. Wang, Y. Zi, Y. S. Zhou, S. Li, F. Fan, L. Lin and Z. L. Wang, J. Mater. Chem. A, 2016, 4, 3728–3734.

227 D. L. Vu, C. D. Le, C. P. Vo and K. K. Ahn, Compos. Part B Eng., 2021, 223, 109135.

228 Y. Liu, Y. Zheng, T. Li, D. Wang and F. Zhou, Nano Energy, 2019, 61, 454–461.

229 A. B. D. Cassie and S. Baxter, Trans. Faraday Soc., 1944, 40, 546–551.

230 Y. Li, Y. Song and Z. Wang, in Handbook of Triboelectric Nanogenerators, eds. Z. L. Wang, Y. Yang, J. Zhai and J. Wang, Springer International Publishing, Cham, 2023, pp. 1035–1078.

231 D. Choi, D. W. Kim, D. Yoo, K. J. Cha, M. La and D. S. Kim, Nano Energy, 2017, 36, 250–259.

232 S. Yang, K. Yin, J. Wu, Z. Wu, D. Chu, J. He and J.-A. Duan, Nanoscale, 2019, 11, 17607–17614.

233 Y. He, L. Wang, T. Wu, Z. Wu, Y. Chen and K. Yin, Nanoscale, 2022, 14, 9392–9400.

234 N. Zhang, H. Zhang, Z. Liu, W. Xu, H. Zheng, Y. Song, Z. Wang and X. Zhou, Nano Energy, 2023, 106, 108111.

235 N. Zhang, H. Gu, K. Lu, S. Ye, W. Xu, H. Zheng, Y. Song, C. Liu, J. Jiao, Z. Wang and X. Zhou, Nano Energy, 2021, 82, 105735.

236 H. Wang, Y. Kurokawa, K. Gotoh, S. Kato, S. Yamada, T. Itoh and N. Usami, Jpn. J. Appl. Phys., 2023, 62, SC1032.

237 N. Zhang, H. Gu, H. Zheng, S. Ye, L. Kang, C. Huang, K. Lu, W. Xu, Q. Miao, Z. Wang, J. Zhang and X. Zhou, Nano Energy, 2020, 73, 104748.

238 Y. Song, W. Xu, Y. Liu, H. Zheng, M. Cui, Y. Zhou, B. Zhang, X. Yan, L. Wang, P. Li, X. Xu, Z. Yang and Z. Wang, The Innovation, 2022, 3, 100301.

239 X. Li, X. Ning, L. Li, X. Wang, B. Li, J. Li, J. Yin and W. Guo, Nano Energy, 2022, 92, 106705.

240 X. Xu, P. Li, Y. Ding, W. Xu, S. Liu, Z. Zhang, Z. Wang and Z. Yang, Energy Environ. Sci., 2022, 15, 2916–2926.

241 J. Dong, L. Zhu, P. Guo, C. Xu, X. Zhao, S. Yang, X. He, G. Zhou, G. Ma, H. Guo, C. Hu and Q. Song, Energy Environ. Sci., 2023, 16, 1071–1081.

242 Y. Li, G. Ma, Y. Li, J. Fu, M. Wang, K. Gong, W. Li, X. Wang, L. Zhu and J. Dong, ACS Appl. Mater. Interfaces, 2024, 16, 27339–27351.

243 S. Tian, L. Lai, J. Xin, Z. Qu, B. Li and Y. Dai, Small, 2024, 20, 2307282.

244 H. Gu, N. Zhang, Z. Zhou, S. Ye, W. Wang, W. Xu, H. Zheng, Y. Song, J. Jiao, Z. Wang and X. Zhou, Nano Energy, 2021, 87, 106218.

245 C. Ye, D. Liu, P. Chen, L. N. Y. Cao, X. Li, T. Jiang and Z. L. Wang, Adv. Mater., 2023, 35, 2209713.

246 C. Ye, D. Liu, X. Peng, Y. Jiang, R. Cheng, C. Ning, F. Sheng, Y. Zhang, K. Dong and Z. L. Wang, ACS Nano, 2021, 15, 18172–18181.

247 Y.-C. Lai, Y.-C. Hsiao, H.-M. Wu and Z. L. Wang, Adv. Sci., 2019, 6, 1801883.

248 H. Wang, L. Xu and Z. Wang, Nanoenergy Adv., 2021, 1, 32–57.

249 G. Liu, L. Xiao, C. Chen, W. Liu, X. Pu, Z. Wu, C. Hu and Z. L. Wang, Nano Energy, 2020, 75, 104975.

250 K. Munirathinam, G. Prasad, D. S. Kim, J. Park and D. Lee, Adv. Mater. Technol., 2023, 8, 2201902.

251 Y. Yang, N. Sun, Z. Wen, P. Cheng, H. Zheng, H. Shao, Y. Xia, C. Chen, H. Lan, X. Xie, C. Zhou, J. Zhong, X. Sun and S.-T. Lee, ACS Nano, 2018, 12, 2027–2034.

252 H. Ouyang, Z. Li, M. Gu, Y. Hu, L. Xu, D. Jiang, S. Cheng, Y. Zou, Y. Deng, B. Shi, W. Hua, Y. Fan, Z. Li and Z. Wang, Adv. Mater., 2021, 33, 2102302.

253 Y.-Y. Cheng, A. Ganguly, Y.-Y. Cheng, C. L. D. Ortiz, A. Pal, P. Shah, K. Kaswan, L.-W. Yang and Z.-H. Lin, Nano Energy, 2024, 125, 109519.

254 A. Gao, Q. Zhou, Z. Cao, W. Xu, K. Zhou, B. Wang, J. Pan, C. Pan and F. Xia, Adv. Sci., 2024, 11, 2309824.

255 S. Chatterjee, S. Saha, S. R. Barman, I. Khan, Y.-P. Pao, S. Lee, D. Choi and Z.-H. Lin, Nano Energy, 2020, 77, 105093.

256 B. D. Chen, W. Tang, C. He, T. Jiang, L. Xu, L. P. Zhu, G. Q. Gu, J. Chen, J. J. Shao, J. J. Luo and Z. L. Wang, Adv. Mater. Technol., 2018, 3, 1700229.

257 R. Zhang, H. Lin, Y. Pan, C. Li, Z. Yang, J. Tian and H. C. Shum, Adv. Funct. Mater., 2022, 32, 2208393.

258 Y. Aoki and R. and Naganuma, Mol. Cryst. Liq. Cryst., 2023, 763, 47–53.

259 L. Yang, J. Yu, Y. Guo, S. Chen, K. Tan and S. Li, Adv. Funct. Mater., 2023, 33, 2302147.

260 L. Wang, W. Li, Y. Song, W. Xu, Y. Jin, C. Zhang and Z. Wang, Adv. Funct. Mater., 2022, 32, 2206705.

261 Z. Chen, Y. Lu, R. Li, R. J. Orlando, R. Manica and Q. Liu, Chem. Eng. J., 2022, 439, 135688.

262 D. Jiang, Y. Su, K. Wang, Y. Wang, M. Xu, M. Dong and G. Chen, Nano Energy, 2020, 70, 104459.

263 L. L. Sun, C. Li, X. Chen and W. Tang, Nano Energy, 2021, 90, 106587.

264 M. Zheng, S. Lin, Z. Tang, Y. Feng and Z. L. Wang, Nano Energy, 2021, 83, 105810.

265 J. Zhang, K. Zhan, S. Wang and X. Hou, Soft Matter, 2020, 16, 2915–2927.

266 S. (সুমনচক্রবর্তী) Chakraborty, C. (চিরদীপ বাকলী) Bakli, D. (দেবমাল্য রায়) Roy, A. (অভিরূপ চৌধুরী) Chaudhuri, A. (অনিরুদ্ধ গুহ) Guha and A. (আদিত্য পটবারী) Patwari, Appl. Phys. Rev., 2025, 12, 011305.

267 X. Hou, Y. S. Zhang, G. T. Santiago, M. M. Alvarez, J. Ribas, S. J. Jonas, P. S. Weiss, A. M. Andrews, J. Aizenberg and A. Khademhosseini, Nat. Rev. Mater., 2017, 2, 1–15.

268 S. S. Das, S. Kar, T. Anwar, P. Saha and S. Chakraborty, Lab. Chip, 2018, 18, 1560–1568.

269 K. Xiao, L. Jiang and M. Antonietti, Joule, 2019, 3, 2364–2380.

270 D. N. Østedgaard-Munck, J. Catalano, M. B. Kristensen and A. Bentien, Mater. Today Energy, 2017, 5, 118–125.

271 J. Catalano, H. V. M. Hamelers, A. Bentien and P. M. Biesheuvel, J. Phys. Condens. Matter, 2016, 28, 324001.

272 S. Haldrup, J. Catalano, M. Hinge, G. V. Jensen, J. S. Pedersen and A. Bentien, ACS Nano, 2016, 10, 2415–2423.

273 W. Olthuis, B. Schippers, J. Eijkel and A. van den Berg, Sens. Actuators B Chem., 2005, 111–112, 385–389.

274 J. Yin, X. Li, J. Yu, Z. Zhang, J. Zhou and W. Guo, Nat. Nanotechnol., 2014, 9, 378–383.

275 J. Yin, Z. Zhang, X. Li, J. Yu, J. Zhou, Y. Chen and W. Guo, Nat. Commun., 2014, 5, 3582.

276 Y. Xie, D. Bos, M.-J. van der Meulen, M. Versluis, A. van den Berg and J. C. T. Eijkel, Nano Energy, 2016, 30, 252–259.

277 Y. Xie, H. L. de Boer, A. J. Sprenkels, A. van den Berg and J. C. T. Eijkel, Lab. Chip, 2014, 14, 4171–4177.

278 F. H. J. van der Heyden, D. Stein and C. Dekker, Phys. Rev. Lett., 2005, 95, 116104.

279 P. Goswami and S. Chakraborty, Langmuir, 2010, 26, 581–590.

280 B. J. Kirby and E. F. Hasselbrink, ELECTROPHORESIS, 2004, 25, 187–202.

281 G. E. Brown, V. E. Henrich, W. H. Casey, D. L. Clark, C. Eggleston, A. Felmy, D. W. Goodman, M. Grätzel, G. Maciel, M. I. McCarthy, K. H. Nealson, D. A. Sverjensky, M. F. Toney and J. M. Zachara, Chem. Rev., 1999, 99, 77–174.

282 C. Shao, B. Ji, T. Xu, J. Gao, X. Gao, Y. Xiao, Y. Zhao, N. Chen, L. Jiang and L. Qu, ACS Appl. Mater. Interfaces, 2019, 11, 30927–30935.

283 F. Zhao, H. Cheng, Z. Zhang, L. Jiang and L. Qu, Adv. Mater., 2015, 27, 4351–4357.

284 J. Li, K. Liu, T. Ding, P. Yang, J. Duan and J. Zhou, Nano Energy, 2019, 58, 797–802.

285 E. E. Saka and C. Güler, Clay Miner., 2006, 41, 853–861.

286 Y. Zhang and T. Xu, Desalination, 2006, 190, 256–266.

287 Y. Zhang, T. Xu and Z. Liu, Desalination, 2007, 212, 183–190.

288 M. Löbbus, H. P. van Leeuwen and J. Lyklema, Colloids Surf. Physicochem. Eng. Asp., 2000, 161, 103–113.

289 T. L. Constantopoulos, G. S. Jackson and C. G. Enke, J. Am. Soc. Mass Spectrom., 1999, 10, 625–634.

290 S. Kamble, S. Agrawal, S. Cherumukkil, V. Sharma, R. V. Jasra and P. Munshi, ChemistrySelect, 2022, 7, e202103084.

291 M. Kosmulski and E. Matijevic, Langmuir, 1992, 8, 1060–1064.

292 T. Liang. Huang, Pei. Tsai, C. Tiao. Wu and C. S. Lee, Anal. Chem., 1993, 65, 2887–2893.

293 J. Caslavska and W. Thormann, J. Microcolumn Sep., 2001, 13, 69–83.

294 I. Z. Atamna, H. J. Issaq, G. M. Muschik and G. M. Janini, J. Chromatogr. A, 1991, 588, 315–320.

295 B. J. Kirby and E. F. Hasselbrink, Electrophoresis, 2004, 25, 203–213.

296 Yunus A. Cengel and John M. Cimbala, Fluid Mechanics Fundamental and Application Fourth Edition, 2018.

297 L. Joly, C. Ybert, E. Trizac and L. Bocquet, J. Chem. Phys., 2006, 125, 204716.

298 B. J. Kirby, Micro- and Nanoscale Fluid Mechanics: Transport in Microfluidic Devices, Cambridge University Press, Cambridge, 2010.

299 V. Tandon and B. J. Kirby, ELECTROPHORESIS, 2008, 29, 1102–1114.

300 Y. Ren and D. Stein, Nanotechnology, 2008, 19, 195707.

301 Y. Xie, L. Fu, T. Niehaus and L. Joly, Phys. Rev. Lett., 2020, 125, 014501.

302 C.-H. Choi, U. Ulmanella, J. Kim, C.-M. Ho and C.-J. Kim, Phys. Fluids, 2006, 18, 087105.

303 S. Parvate, P. Dixit and S. Chattopadhyay, J. Phys. Chem. B, 2020, 124, 1323–1360.

304 S. Das, S. Kumar, S. K. Samal, S. Mohanty and S. K. Nayak, Ind. Eng. Chem. Res., 2018, 57, 2727–2745.

305 E. B. Caldona, A. C. C. De Leon, P. G. Thomas, D. F. I. Naylor, B. B. Pajarito and R. C. Advincula, Ind. Eng. Chem. Res., 2017, 56, 1485–1497.

306 M. Malekidelarestaqi, A. Mansouri and S. F. Chini, Chem. Phys. Lett., 2018, 703, 72–79.

307 T. M. Squires, Phys. Fluids, 2008, 20, 092105.

Lab on a Chip Accepted Manuscript

308 H. Zhao, Phys. Fluids, 2011, 23, 022003.

309 T.-S. Wong, S. H. Kang, S. K. Y. Tang, E. J. Smythe, B. D. Hatton, A. Grinthal and J. Aizenberg, Nature, 2011, 477, 443–447.

310 B. Fan, A. Bhattacharya and P. R. Bandaru, Nat. Commun., 2018, 9, 4050.

311 B. Fan and P. R. Bandaru, Langmuir, 2019, 35, 6203–6210.

312 B. Fan and P. R. Bandaru, Langmuir, 2019, 35, 14812–14817.

313 B. Fan and P. R. Bandaru, Langmuir, 2020, 36, 10238–10243.

314 L. Cheng, B. Fan, Z. Zhang and P. Bandaru, Langmuir, 2021, 37, 6736–6743.

315 L. Cheng, B. Fan, Z. Zhang, A. McLeod, W. Shipley and P. Bandaru, Langmuir, 2022, 38, 11837–11844.

316 D. Jing, Y. Pan and X. Wang, Int. J. Heat Mass Transf., 2017, 113, 32–39.

317 D. Jing and B. Bhushan, J. Colloid Interface Sci., 2015, 454, 152–179.

318 F. H. J. van der Heyden, D. J. Bonthuis, D. Stein, C. Meyer and C. Dekker, Nano Lett., 2006, 6, 2232–2237.

319 H. Daiguji, P. Yang and A. Majumdar, Nano Lett., 2004, 4, 137–142.

320 J. F. Osterle, J. Appl. Mech., 1964, 31, 161–164.

321 R. J. Gross and J. F. Osterle, J. Chem. Phys., 1968, 49, 228–234.

322 H. Ban, B. Lin and Z. Song, Biomicrofluidics, 2010, 4, 014104.

323 S. Das, A. Guha and S. K. Mitra, Anal. Chim. Acta, 2013, 804, 159–166.

324 S. C. Yang, Microfluid. Nanofluidics, 2006, 2, 501–511.

325 J. Pfitzner, Anaesthesia, 1976, 31, 273–275.

326 S. Smirnov, I. Vlassiouk, P. Takmakov and F. Rios, ACS Nano, 2010, 4, 5069–5075.

327 C. Zhang, X. Wang, J. Jin, L. Li and J. D. Miller, Colloids Interfaces, 2021, 5, 44.

328 R. Hatsuki, F. Yujiro and T. Yamamoto, Microfluid. Nanofluidics, 2013, 14, 983–988.

329 R. G. Neo and B. C. Khoo, Appl. Energy, 2021, 285, 116428.

330 Y. Yang and C. Lee, Droplet, 2022, 1, 7–10.

331 R. Guigon, J.-J. Chaillout, T. Jager and G. Despesse, Smart Mater. Struct., 2008, 17, 015039.

332 Q. Zhang, Y. Li, H. Cai, M. Yao, H. Zhang, L. Guo, Z. Lv, M. Li, X. Lu, C. Ren, P. Zhang, Y. Zhang, X. Shi, G. Ding, J. Yao, Z. Yang and Z. L. Wang, Adv. Mater., 2021, 33, 2105761.

333 Y. Zhao, J. Duan, B. He and Q. Tang, J. Alloys Compd., 2019, 776, 31–35.

334 H. Kong, P. Si, M. Li, X. Qiu, J. Liu, X. Wang, Q. Wang, Y. Li and Y. Wang, Nano Lett., 2022, 22, 3266–3274.

335 J. Park, S. Song, Y. Yang, S.-H. Kwon, E. Sim and Y. S. Kim, J. Am. Chem. Soc., 2017, 139, 10968–10971.

336 S. Yang, Y. Su, Y. Xu, Q. Wu, Y. Zhang, M. B. Raschke, M. Ren, Y. Chen, J. Wang, W. Guo, Y. Ron Shen and C. Tian, J. Am. Chem. Soc., 2018, 140, 13746–13752.

337 S. G. Yoon, H. Jin, W. H. Lee, J. Han, Y. H. Cho and Y. S. Kim, Nano Energy, 2021, 80, 105522.

338 W. Wang, W. Gong, Y. Wang, G. Li, W. Lu, Y. You and X. Zhang, J. Mater. Chem. A, 2021, 9, 5588–5596.

339 A. S. Aji, R. Nishi, H. Ago and Y. Ohno, Nano Energy, 2020, 68, 104370.

340 M.-Y. Ryu, H.-K. Jang, K. Jin Lee, M. Piao, S.-P. Ko, M. Shin, J. Huh and G.-T. Kim, Phys. Chem. Chem. Phys., 2017, 19, 13133–13139.

341 G. Kukucska and J. Koltai, Phys. Status Solidi B, 2017, 254, 1700184.

342 S. Pennock, M. M. Vanegas-Cantarero, T. Bloise-Thomaz, H. Jeffrey and M. J. Dickson, Renew. Energy, 2022, 190, 1078–1088.

343 B. Del Río-Gamero, T. Lis Alecio and J. Schallenberg-Rodríguez, Desalination, 2022, 525, 115479.

344 J. Tan, J. Duan, Y. Zhao, B. He and Q. Tang, Nano Energy, 2018, 48, 128–133.

345 W. Fei, C. Shen, S. Zhang, H. Chen, L. Li and W. Guo, Nano Energy, 2019, 60, 656–660.

346 X.-S. Zhang, M.-D. Han, R.-X. Wang, F.-Y. Zhu, Z.-H. Li, W. Wang and H.-X. Zhang, Nano Lett., 2013, 13, 1168–1172.

347 K. Y. Lee, J. Chun, J. Lee, K. N. Kim, N. Kang, J. Kim, M. H. Kim, K. Shin, M. K. Gupta, J. M. Baik and S. Kim, Adv. Mater., 2014, 26, 5037–5042.

348 W. Seung, M. K. Gupta, K. Y. Lee, K.-S. Shin, J.-H. Lee, T. Y. Kim, S. Kim, J. Lin, J. H. Kim and S.-W. Kim, ACS Nano, 2015, 9, 3501–3509.

349 C. Chang, V. H. Tran, J. Wang, Y.-K. Fuh and L. Lin, Nano Lett., 2010, 10, 726–731.

350 X. Wang, J. Song, J. Liu and Z. L. Wang, Science, 2007, 316, 102–105.

351 L. Joly, C. Ybert, E. Trizac and L. Bocquet, Phys. Rev. Lett., 2004, 93, 257805.

352 F. H. J. van der Heyden, D. Stein, K. Besteman, S. G. Lemay and C. Dekker, Phys. Rev. Lett., 2006, 96, 224502.

353 G. Xue, Y. Xu, T. Ding, J. Li, J. Yin, W. Fei, Y. Cao, J. Yu, L. Yuan, L. Gong, J. Chen, S. Deng, J. Zhou and W. Guo, Nat. Nanotechnol., 2017, 12, 317–321.

354 H. Cheng, Y. Huang, L. Qu, Q. Cheng, G. Shi and L. Jiang, Nano Energy, 2018, 45, 37–43.

355 D. Shen, M. Xiao, G. Zou, L. Liu, W. W. Duley and Y. N. Zhou, Adv. Mater., 2018, 30, 1705925.

356 Y. Huang, H. Cheng, C. Yang, H. Yao, C. Li and L. Qu, Energy Environ. Sci., 2019, 12, 1848–1856.

357 T. Xu, X. Ding, Y. Huang, C. Shao, L. Song, X. Gao, Z. Zhang and L. Qu, Energy Environ. Sci., 2019, 12, 972–978.

358 J. Luo and Z. L. Wang, Energy Storage Mater., 2019, 23, 617–628.

359 T. Zhong, H. Guan, Y. Dai, H. He, L. Xing, Y. Zhang and X. Xue, Nano Energy, 2019, 60, 52–60.

360 G. Zhang, Z. Duan, X. Qi, Y. Xu, L. Li, W. Ma, H. Zhang, C. Liu and W. Yao, Carbon, 2019, 148, 1–8.

361 H.-J. Li, D. Zhang, H. Wang, Z. Chen, N. Ou, P. Wang, D. Wang, X. Wang and J. Yang, Small, 2019, 15, 1804146.

362 W. ur Rehman, Y. Ma, Z. khan, F. Z. A. Laaskri, J. Xu, U. Farooq, A. Ghani, H. Rehman and Y. Xu, Mater., 2025, 7, 100450.

363 S. S. Das, V. M. Pedireddi, A. Bandopadhyay, P. Saha and S. Chakraborty, Nano Lett., 2019, 19, 7191–7200.

364 X. Zhou, W. Zhang, C. Zhang, Y. Tan, J. Guo, Z. Sun and X. Deng, ACS Appl. Mater. Interfaces, 2020, 12, 11232–11239.

365 K. Jiao, H. Yan, F. Qian, W. Zhang, H. Li, Q. Wang and C. Zhao, J. Power Sources, 2023, 569, 233007.

366 H. Su, A. Nilghaz, D. Liu, L. Dai, B. Tang, Z. Wang, J. M. Razal, J. Tian and J. Li, Chem. Eng. J. Adv., 2023, 14, 100498.

367 X. Fan, Y. Yang, X. Shi, Y. Liu, H. Li, J. Liang and Y. Chen, Adv. Funct. Mater., 2020, 30, 2007110.

368 Y. Zhang, H. Zhang, T. Xiong, H. Qu, J. Justin Koh, D. Krishna Nandakumar, J. Wang and S. Ching Tan, Energy Environ. Sci., 2020, 13, 4891–4902.

369 Flexible and Washable CNT-Embedded PAN Nonwoven Fabrics for Solar-Enabled Evaporation and Desalination of Seawater | ACS Applied Materials & Interfaces, https://pubs.acs.org/doi/full/10.1021/acsami.9b12806, (accessed March 26, 2025).

370 H. Peng, D. Wang and S. Fu, Chem. Eng. J., 2021, 426, 131818.

371 V.-D. Dao, N. H. Vu, H.-L. Thi Dang and S. Yun, Nano Energy, 2021, 85, 105979.

372 P. Xiao, J. He, F. Ni, C. Zhang, Y. Liang, W. Zhou, J. Gu, J. Xia, S.-W. Kuo and T. Chen, Nano Energy, 2020, 68, 104385.

373 S. Chu and A. Majumdar, Nature, 2012, 488, 294–303.

374 K. Liu, T. Ding, J. Li, Q. Chen, G. Xue, P. Yang, M. Xu, Z. L. Wang and J. Zhou, Adv. Energy Mater., 2018, 8, 1702481.

375 K. Liu, T. Ding, X. Mo, Q. Chen, P. Yang, J. Li, W. Xie, Y. Zhou and J. Zhou, Nano Energy, 2016, 30, 684–690.

376 Z. Zhang, X. Li, J. Yin, Y. Xu, W. Fei, M. Xue, Q. Wang, J. Zhou and W. Guo, Nat. Nanotechnol., 2018, 13, 1109–1119.

377 A. K. M. Newaz, D. A. Markov, D. Prasai and K. I. Bolotin, Nano Lett., 2012, 12, 2931–2935.

378 J. Yin, X. Li, J. Yu, Z. Zhang, J. Zhou and W. Guo, Nat. Nanotechnol., 2014, 9, 378–383.

379 Y. Zhou, D. Yue, S. Li, G. Liang, Z. Chao, Y. Zhao and X. Meng, J. Clean. Prod., 2022, 357, 131887.

380 Y. Tang, F. Feng, Z. Guo, W. Feng, Z. Li, J. Wang, Q. Sun, H. Ma and Y. Li, J. Clean. Prod., 2020, 277, 124159.

381 J. Lin, W. Chen, X. Qi and H. Hou, J. Clean. Prod., 2021, 309, 127077.

382 P. Wen, J. Ren and S. Ling, ACS Appl. Electron. Mater., 2023, 5, 2082–2092.

383 Y. Liang, F. Zhao, Z. Cheng, Q. Zhou, H. Shao, L. Jiang and L. Qu, Nano Energy, 2017, 32, 329–335.

384 F. Zhao, Y. Liang, H. Cheng, L. Jiang and L. Qu, Energy Environ. Sci., 2016, 9, 912–916.

385 M. Li, L. Zong, W. Yang, X. Li, J. You, X. Wu, Z. Li and C. Li, Adv. Funct. Mater., 2019, 29, 1901798.

386 D. Shen, M. Xiao, Y. Xiao, G. Zou, L. Hu, B. Zhao, L. Liu, W. W. Duley and Y. N. Zhou, ACS Appl. Mater. Interfaces, 2019, 11, 14249–14255.

387 L. Hao and B. Fan, Nanoscale, 2025, 17, 6448–6459.

388 D. Xu, M. Yan and Y. Xie, ELECTROPHORESIS, 2024, 45, 244–265.

Lab on a Chip Accepted Manuscript

No primary research results, software or code have been included and no new data were generated or analysed as part of this review.